Defect Characterization in 4% Cadmium Zinc Telluride Semiconductors

by

Silvia I. Penkova
Bachelor of Engineering, University of Victoria, 2015

A Thesis Submitted in Partial Fulfillment
of the Requirements for the Degree of

MASTER OF APPLIED SCIENCE

in the Faculty of Mechanical Engineering

© Silvia I. Penkova, 2018
University of Victoria

All rights reserved. This thesis may not be reproduced in whole or in part, by photocopy
or other means, without the permission of the author.

Supervisory Committee

Defect Characterization in 4% Cadmium Zinc Telluride Semiconductors

by

Silvia I. Penkova
Bachelor of Engineering, University of Victoria, 2015

Supervisory Committee

Dr. Rodney Herring, Department of Mechanical Engineering
Supervisor

Dr. Thomas Tiedje, Department of Electrical and Computer Engineering
Co-Supervisor

Dr. Jordan Roszmann, Department of Mechanical Engineering
Departmental Member

Abstract

Supervisory Committee

Dr. Rodney Herring, Department of Mechanical Engineering
Supervisor

Dr. Thomas Tiedje, Department of Electrical and Computer Engineering
Co-Supervisor

Dr. Jordan Roszmann, Department of Mechanical Engineering
Departmental Member

This thesis presents a characterization study of Cadmium Zinc Telluride with a 4% Zinc molar concentration using five different techniques. Three of the characterization methods – X-ray diffraction (XRD), transmission electron microscopy (TEM) and wet chemical etching – were used to study the atomic arrangement of the lattice and the type of defects in the material. On the other hand, the other two methods – photoluminescence (PL) and the Hall Effect – provided information about the electronic properties of the material and identified the electronic signatures of the defects present. This thesis study applied these five methods to 29 samples with the [111] and [211] crystal orientations.

XRD was used to calculate the Zn concentration and the atomic spacing of the samples. TEM allowed to map the crystal structure using Kikuchi diffraction and to calculate the variation of the local lattice constant. This showed that the sample was under strain. A CBED imaging condition producing HOLZ lines allowed for qualitatively imaging the strain field in the crystal and contrast phase imaging showed stacking faults and dislocations present in the lattice. Next, wet chemical etching - using Nakagawa and Everson solutions – revealed several different types of etch pits were present on the material's surface and provided a value for the etch pit density (EPD). PL at room temperature was used to calculate the Zn concentration and to produce contour maps of the samples showing the variation in Zn. Low temperature PL was used to conduct intensity and thermal studies of the material providing information about the type of emission (donor-acceptor pair, free exciton or excitonic) and the activating energies. This information was used to assign the peaks seen in the PL spectrum at 8K. Lastly, the Hall Effect experiment was used to calculate the resistivity and the mobility of carriers, i.e., electrons and holes, of the samples.

The last stage of the project was to seek correlations between the data obtained during the five characterization techniques. Correlations were noted between the XRD FWHM broadening and the EPD, the disturbances in the atomic lattice and the defect band broadening and a summary of all the values calculated during the project was provided. Overall this project provided a very thorough study of 4% CZT.

Table of Contents

Supervisory Committee ii
Abstract iii
Table of Contents iv
List of Tables vii
List of Figures viii
Acknowledgments xiii
Dedication xiv
Chapter 1 Introduction on Cadmium Zinc Telluride Semiconductors 1
1.1 Introduction 1
1.2 Motivation for Study 2
1.3 Organization of Thesis 3
Chapter 2 Crystal Morphology 4
2.1 Crystal Structure and Electronic Properties 4
2.1.1 Zincblende Crystal Structure 4
2.1.2 Electronic Properties 5
2.2 Growth Techniques 6
2.2.1 Vertical Gradient Freeze Growth Process 6
2.2.2 Effects of Segregation 6
2.3 Types and Effects of Defects on Semiconductor Performance 7
2.3.1 Tellurium Precipitates and Inclusions 7
2.3.2 Pipes and Wires 9
2.3.3 Other Common Defects in CZT (Cracks, Grain Boundaries and Twins) 9
Chapter 3 Structural Characterization 11
3.1 Theory 11
3.1.1 X-ray Diffraction 11
3.1.2 Transmission Electron Microscopy 14
3.1.3 Wet Chemical Etching 16
3.2 Experimental Method 18
3.2.1 X-ray Diffraction 18

3.2.2 Transmission Electron Microscopy 19

3.2.3 Wet Chemical Etching 19

3.3 Results 20

3.3.1 X-ray Diffraction Results 20

3.3.2 Transmission Electron Microscopy Results 26

3.3.3 Wet Chemical Etching 32

3.4 Discussion 36

3.4.1 X-ray Diffraction Results Interpretation 36

3.4.2 Transmission Electron Microscopy Interpretation 38

3.4.3 Wet Chemical Etching Discussion 40

Chapter 4 Electronic Characterization 45

4.1 Theory 45

4.1.1 Photoluminescence 45

4.2.1 Hall Effect in Semiconductors 48

4.2 Experimental Method 49

4.2.1 Photoluminescence 49

4.2.2 Hall Effect in Semiconductors 52

4.3 Results 53

4.3.1 Photoluminescence 53

4.3.2 Hall Effect in Semiconductors 72

4.4 Discussion 76

4.4.1 Photoluminescence 76

4.4.2 Hall Effect in Semiconductors 79

Chapter 5 Connection Between Structure and Electronic Properties 81

5.1 Effects of Strain on the Material Quality 81

5.2 Zn Concentration Comparison Between XRD and PL Methods 83

5.3 Relationship between Lattice Disruptions and Electronic Broadening 84

5.4 Relationship between Etch Pit Density and XRD FWHM 86

5.5 $Cd_{0.96}Zn_{0.04}Te$ Material Properties 87

Chapter 6 Conclusion 89

References 91

Appendix A Details of TEM Sample Preparation 95
1. Selecting an Area for TEM Study... 95
2 Sample Preparation Using the Lift-Out Process 96
3 Finishing Clean – Ion Milling and Zone Cleaning 103

List of Tables

Table 3.1: Kikuchi bands related to the angle of tilt of the specimen holder containing the sample 26

Table 3.2: Software calibration for a 0.3m camera length 28

Table 3.3: Local lattice constants calculated from the (123) zone axis diffraction pattern 30

Table 3.4: Nakagawa etch pit density results for six [111] oriented samples 33

Table 3.5: Everson etch pit density count results 35

Table 4.1: Bound exciton types, composition and PL emission energies present in CZT [43, 44] 46

Table 4.2: Room temperature PL fitting parameters used in band gap calculation 56

Table 4.3: Summary of emission types observed at different peak energies 67

Table 4.4: Fitting parameters for each energy of the DAP Arrhenius spectra (Fig. 4.30 to Fig. 4.34) 70

Table 4.5: Fitting parameters from the Excitonic temperature dependence fit using Equation 4.8 (Fig. 4.35 to Fig 4.38) 72

Table 4.6: Hall Measurement results for Samples I, J, and U 76

Table 5.1: Results of characterizing CZT samples 87

Table A.1: FIB beams used for the TEM sample preparation and their purpose 97

List of Figures

Figure 2.1: Zincblende crystal structure with interpenetrating A (white) and B (blue) sub-lattices 4

Figure 2.2: Te precipitates are visible in the CZT matrix because they are not transparent in the IR........ 8

Figure 3.1: Bragg's law showing the constructive interference of waves scattered from two parallel planes 11

Figure 3.2: Schematic showing the difference between the formation of Kikuchi lines due to inelastic scattering in (a) and the formation of HOLZ lines with elastic electron scattering in (b) 15

Figure 3.3: (a) Zinc concentration (molar) variation between all 29 samples, (b) [111] oriented samples only and (c) [211] oriented samples only 21

Figure 3.4: (a) Sample U showing an example of a splitting XRD peak, (b) Sample W showing an example of overlapping peaks with a shoulder and (c) variation in distribution for all [111] XRD peaks 22

Figure 3.5: (a) Sample M showing an example of a single peak with a shoulder, (b) Sample N showing an example of a single peak without a shoulder and (c) variation in distribution for all [211] XRD peaks 23

Figure 3.6: (a) Distribution of FWHM values for all [111] and [422] reflections of all samples, (b) only [111] reflections and (c) only [422] reflections 23

Figure 3.7: Reciprocal space lattice map of Sample T [111], FWHM = 116.25 arc seconds........ 25

Figure 3.8: Reciprocal space lattice map of Sample M [211], FWHM = 37.68 arc seconds 25

Figure 3.9: Kikuchi map of [111] oriented CZT sample obtained by tilting the sample from -13 degrees to +13 degrees and travelling between three zone axes (ZA)........ 27

Figure 3.10: Diffraction pattern at ZA3 showing the distances between spots in reciprocal lattice units (1/nm) 28

Figure 3.11: Tabulated (123) diffraction pattern for FCC crystals [28] 29

Figure 3.12: (a) Splitting of HOLZ lines, noted by white arrow, due to the strain induced by the precipitate, (b) impact of contamination on the strain in the material and (c) bending of HOLZ lines around a precipitate causing a high strain region................. 31
Figure 3.13: (a) Lattice image of [111] oriented CZT sample showing four regions (A, B, C and D) with dislocations, (b) close up of a dislocation and (c) close up of an edge dislocation 32
Figure 3.14: (a) Example field of view of Nakagawa pits visible at x10 magnification and (b) close up of smaller and larger triangular etch pits observed in the material............... 33
Figure 3.15: (a) x100 magnification view of evenly distributed EPD and (b) a view showing areas of EPD clusters (right) 34
Figure 3.16: Six types of etch pits observed through the Everson etch method............... 35
Figure 3.17: Model for spreading of Cd and Te dislocations throughout the material via tangential and tetrahedral glide systems [38]... 42
Figure 3.18: Examples of etch pits representing tetrahedral slide systems observed during the experiment in both (111) and (211) oriented CZT samples...................................... 43
Figure 3.19: Dislocation direction assignment of four etch pits in [111] oriented samples (left) and [111] pole figure used for assignment (right). Figure adapted from Ref. [35] . 44
Figure 3.20: Three examples of a triangular cluster of etch pits found in the material studied in this thesis, which has been shown to form on top of Te precipitates, which are below the surface of the material [37] 44
Figure 4.1: Energy level diagram for various radiative transitions in $Cd_{1-x}Zn_xTe$ (x = 4%), reinterpreted from [45].. 47
Figure 4.2: Schematic of the Hall Effect observed in semiconductors placed in a magnetic field 48
Figure 4.3: Photoluminescence set up used for room temperature experiments 50
Figure 4.4: Low temperature photoluminescence experimental set up 51
Figure 4.5: (a) van der Pauw I-V control unit and magnet and (b) van der Pauw device showing sample mounted on glass slide with four contacts 52
Figure 4.6: Example room temperature fitting analysis for calculating Eg in Sample B (black, Equation 4.6 fit), and comparison to the improvement from Equation 4.5 (red and blue) showing the previous fit compared with the raw data (orange).............................. 55

Figure 4.7: Sample L [211] convolution fit 55
Figure 4.8: Sample S [111] convolution fit 55
Figure 4.9: Zinc (%, molar) concentration spread for all 29 samples (left) and this same data repeated separating the growth directions [111] (top right) and [211] (bottom right) 57
Figure 4.10: Zn (%) distribution contour map of Sample W, [111] 58
Figure 4.11: Zn (%) distribution contour map of Sample Y, [111] 58
Figure 4.12: Zn (%) distribution contour map of Sample R, [111] 59
Figure 4.13: Zn (%) distribution contour map of Sample N, [211] 59
Figure 4.14: Zn (%) distribution contour map of Sample M, [211] 59
Figure 4.15: Zn (%) distribution contour map of Sample F, [211] 59
Figure 4.16: Zn (%) distribution contour map of Sample M, [211] 60
Figure 4.17: Zn (%) distribution contour map of Sample BB, [211] 60
Figure 4.18: PL spectrum of sample R obtained at 9 K. (top) Residual plot showing peak fitting quality, (middle) PL spectra of the sample (red) overlaid on the sum of the Gaussian analysis results (blue); and (bottom) peaks used to produce curve fitting equation 61
Figure 4.19: Identification of the PL emission peaks in sample Sample R at 8K 63
Figure 4.20: Power dependence study for Sample R showing changes in peaks with decrease in laser power. The decrease in power is achieved with a smaller number of the ND filter 64
Figure 4.21: Power dependence fit for 1.547 eV peak 65
Figure 4.22: Power dependence fit for 1.570 eV donor acceptor pair (DAP) peak 65
Figure 4.23: Power dependence fit for 1.588 eV (A,X)-LO longitudinal optical phonon replica peak 66
Figure 4.24: Power dependence fit for 1.598 eV X-LO longitudinal optical phonon replica peak 66
Figure 4.25: Power dependence fit for bound acceptor (A,X) 1.610 eV peak 66
Figure 4.26: Power dependence fit for 1.614 eV bound donor (D,X) peak 66
Figure 4.27: Power dependence fit for 1.619 eV free exciton (F,X) peak 67
Figure 4.28: Temperature dependence plot of spectrum from 9K to 300K for Sample R 68

Figure 4.29: Tellurium vacancy temperature dependence spectrum plot from 9K to 220K 68
Figure 4.30: DAP Arrhenius fitting function results for Te vacancy peak at 1.11 eV 69
Figure 4.31: DAP Arrhenius fitting function results for the peak at 1.24 eV 69
Figure 4.32: DAP Arrhenius fitting function results for the peak at 1.54 eV 69
Figure 4.33: DAP Arrhenius fitting function results for the donor acceptor peak (DAP) at 1.56 eV 69
Figure 4.34: DAP Arrhenius fitting function results for the longitudinal optical replica (A,X)-LO peak 70
Figure 4.35: Excitonic Arrhenius fit for the 1.59 eV X-LO longitudinal optical phonon replica peak 71
Figure 4.36: Excitonic Arrhenius fit for the 1.61 eV bound acceptor (A,X) peak 71
Figure 4.37: Excitonic Arrhenius fit for the 1.614 eV bound donor (D,X) peak 71
Figure 4.38: Excitonic Arrhenius fit for the 1.619 eV free exciton (F,X) peak 71
Figure 4.39: (a) I-V curves used to calculate the sheet resistance in Samples J, (b) Sample I and (c) Sample U 73
Figure 4.40: Negative magnetic field (left) and positive magnetic field (right) I-V curves used to calculate the Hall coefficient for Sample I 74
Figure 4.41: Negative magnetic field (left) and positive magnetic field (right) I-V curves used to calculate the Hall coefficient for Sample J 74
Figure 4.42: Negative magnetic field (left) and positive magnetic field (right) I-V curves used to calculate the Hall coefficient for Sample U 75
Figure 5.1: (a) XRD peak shape and (b) room temperature PL map for Sample W [111]81
Figure 5.2: (a) XRD peak shape and (b) room temperature PL map for Sample N [211] 82
Figure 5.3: (a) XRD peak shape and (b) room temperature PL map for Sample U [111] 82
Figure 5.4: Plot of correlation between the Zn (%) molar concentrations found by XRD and by PL for each of the two crystal orientations 83
Figure 5.5: Plot of XRD peak FWHM and PL FWHM low temperature emission peaks from Samples E, M, Q and BB 85
Figure 5.6: (a) Nakagawa etch EPD vs. XRD FWHM broadening and (b) Everson etch EPD vs. XRD FWHM broadening 86

Figure A.1: SEM image showing etch pits at x150 magnification (left) and a zoomed in image at x300 magnification (right) 96
Figure A.2: Damage from FIB beam alignment (left) and a close up between a damaged and non-damaged area (right) 98
Figure A.3: FIB image showing an etch pit group found on Sample 3 (left) and a close up of the large etch pit circled in red (right) 99
Figure A.4: Unwanted W deposition outside of red box (left) and final area covered with W in red box (right) 100
Figure A.5: Isometric view of lift out sample (left) and top view (right) 101
Figure A.6: TEM sample holder inserted into FIB in order to attach the specimen into the viewing area 102
Figure A.7: Front view of the sample mounted in TEM holder (left) and a zoomed out view of the sample in the TEM holder (right) 102

Acknowledgments

I want to thank my thesis supervisors Dr. Thomas Tiedje and Dr. Rodney Herring for giving me the opportunity to work on this project. Studying CZT by using highly specialized material characterization methods allowed me to learn about the field of material science and semiconductor manufacture. Most importantly, their continued support throughout this project taught me how to independently work on research material directly and indirectly related to my educational background, manage that work and also analyze and present scientific data. It is those transferrable skills that provided the most personal growth and valuable learning experience of the entire project. These are things I will carry forward with me into my career as a mechanical engineer wherever I go, but without them it would not have been possible.

I also want to thank Dr. Sadik Dost and the UVIC Crystal Growth Laboratory for providing me with the samples which I used to study in this project. Last but not least, I want to extend sincere thanks to my laboratory colleagues Dr. Vahid Bahrami-Yekta and Dr. Svetlana Kostina for their continued support and help during the experimental and analysis phases of my thesis. Your company and guidance through this project made it not only educational but also socially rewarding.

Dedication

To Pisa

Chapter 1
Introduction on Cadmium Zinc Telluride Semiconductors

Semiconducting compounds make up the backbone of all electronics today. Their applications span the entire range of the market from nano-devices, to all fields of commercial transportation and even supercomputers. One application of semiconducting compounds is in the field of radiation detection. This field makes use of single crystals, grown from melt compounds, which are able to work with high energy electromagnetic signals such as x-rays and gamma rays. The challenge of mass commercializing this type of technology has been the inability to produce large sized low defect single crystal wafers. One such promising material is Cadmium Zinc Telluride (CZT). This master's thesis focused on studying the types of defects present in CZT by applying five different characterization techniques.

1.1 Introduction

Cadmium Zinc Telluride ($Cd_{1-x}Zn_xTe$) is a pseudo binary compound made up of CdTe and ZnTe, which form a zincblende structure [1]. An important property of CZT is its tuneable lattice parameter. The lattice parameter is dependent on the Zinc concentration, which also has a direct effect on the band gap of the material. CZT is a wide band gap (1.49 eV) material, when compared to other single crystal semiconductors such as high purity germanium and silicon, which have band gaps of 0.8 and 1.1 eV, respectively [1]. This wider band gap reduces leakage currents and allows CZT x-ray detectors to operate at room temperature thus making it a preferred choice compared with silicon or germanium which need to be cooled.

CZT is generally manufactured in a 4% or a 10% Zinc concentration. These two concentrations are chosen for the following reasons:

1) Using a 4% Zn concentration allows for the lattice constant to be matched to that of HgCdTe, an infrared (IR) detecting material, in order to be used as a growth substrate. These substrates are used for military applications such as night vision goggles and IR tracking cameras in drones [2].

2) In the 10% zinc concentration, CZT crystals are used in gamma ray and x-ray detection. This concentration is preferred for medical imaging (PET scans), airport security (baggage scanning) and homeland security applications (dirty bomb detection) [2].

Previous work by Chu at al (2004) [3] has shown that one of the roles of Zn is to reduce the density of Te antisite defects (Te_{Cd}) and also to increase the density and diffusion rate of Cd vacancies (V_{Cd}). This increase in diffusion and higher Zn concentration causes the vacancies to merge, which in turn promotes the trapping of Te precipitates. These are one of the most common defects in CZT that lower the spectral resolution of CZT detectors and are discussed in more detail further in this chapter [3]. Due to this mechanism, the same study showed that growing CZT detectors with higher than 10% Zn concentrations produce inferior results.

The interaction of these detectors with higher energy electromagnetic radiation signals, such as gamma rays and X-rays, happens via one or more of the four following mechanisms: elastic scattering, photoelectric absorption, Compton scattering or pair production. The main process for interaction in CZT is by photoelectric absorption. In this process, the energy from the absorbed photon interacts with the orbital electrons in the atoms of the detector. As the high energy photon penetrates the detector material, it is absorbed by valence or core electrons and the excited electron loses its kinetic energy as a result of Coulomb interactions and produces many electron-hole pairs. The charges created in this process drift across the detector volume creating a current in an external circuit. The detection of these pairs occurs through pulse charge signals which are used to recreate a histogram of pulse peaks with a height, which is proportional to the energy of the absorbed photon [4]. This histogram can then be reconstructed using specialized software and the known detector geometry to present meaningful information such as a 3D image of a computed tomography (CT) medical scan.

1.2 Motivation for Study

The goal of this thesis was to examine 29 samples, in the [111] and [211] crystal plane orientations, by using five distinct characterization methods and to lend further understanding to

the types of defects seen in CZT. Three of the five methods employed during this study - X-ray diffraction, Transmission Electron Microscopy and Wet Chemical Etching – were used to examine atomic arrangements of the lattice. On the other hand, the other two methods - Photoluminescence and the Hall Effect - studied the electronic properties of the material. The results from each method were first independently interpreted and then a correlation between results from the different methods was established. The goal of this study was to examine a large batch of samples and to use that information to conclude, with some certainty, that trend lines in fact observed were a valid result and not an outlier.

1.3 Organization of Thesis

This thesis focuses on five destructive and non-destructive methods of studying CZT, laid out in six different chapters. The first chapter provides an introduction to the properties of CZT and the significance of this material to the research field.

In chapter 2, a review of the material properties is provided, including discussions on how to grow CZT and the types of defects which affect large scale production.

In chapter 3, CZT's structural properties are studied using x-ray diffraction, transmission electron microscopy (TEM) and chemical etching. The theory and experimental method behind each analysis type is explained, followed by a presentation of the experimental results and an interpretation.

In chapter 4, CZT's electronic properties were studied using photoluminescence (PL) and the Hall Effect in semiconductors. As in Chapter 3, a review of the theory and experimental method is provided, followed by the results from each characterization method and their interpretation.

In chapter 5, the results from the preceding chapter are looked at as a big picture, interpreted and discussed. First the results of each method are independently interpreted, and then a discussion involving cross links between the methods is presented.

In chapter 6, a summary of the work in the thesis and closing remarks - including suggestions for future work – are provided.

Chapter 2
Crystal Morphology

2.1 Crystal Structure and Electronic Properties

2.1.1 Zincblende Crystal Structure

The properties allowing CZT detectors to efficiently absorb higher energy electromagnetic signals are rooted in the atomic arrangement of the zincblende structure. The zincblende structure is made up from two interpenetrating face centered cubic lattices which are offset from each other by ¼ of the cubic diagonal vector. In binary II-VI compounds, each sub-lattice is made up of atoms from one of group II or group VI. Each atom in the structure is positioned at the center of a tetrahedron formed by the four closest atoms (Fig.2.1) [4].

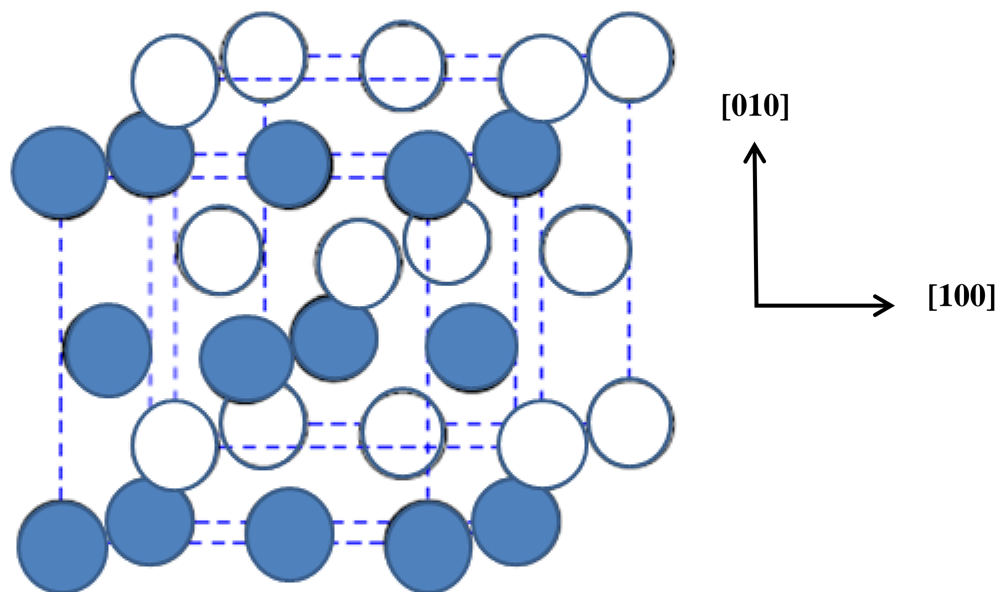

Figure 2.1: Zincblende crystal structure with interpenetrating A (white) and B (blue) sub-lattices

The most common growth orientation for CZT is with axes aligned in the <110> or <111> crystallographic directions. Material grown in the <111> direction has face polarity, either an A or a B face. The A-polar face is terminated with Cd and Zn atoms, whereas the B-polar face is

terminated with Te atoms. One property of the face polarity is that each face has a different chemical reactivity and reacts differently to etching [5] (discussed further in Section 3.3.3).

2.1.2 Electronic Properties

CZT is held together by covalent bonds. This bonding type binds all of the electrons in the lattice. In the event that the temperature is not at absolute zero or there are electronically active defects some electrons can be excited into the conduction state. The electrons which are bound to an atom are considered to occupy a valence state whereas the mobile electrons are said to occupy a conduction state. The energy required for an electron to transition from the valence band to the conduction band is equal to the band-gap of the material. One mechanism allowing this bi-directional valence-to-conduction transition to take place is the absorption of a photon. CZT is a direct band-gap semiconductor which does not require an exchange of momentum between electrons transitioning between the valence and conduction states. This is an important advantage over in-direct band-gap semiconductors - such as silicon - because direct band-gap semiconductors promote a stronger interaction of photons with electrons. This means that a much smaller volume of material is required to absorb light and to result in a photoelectric interaction. The more electrons which are able to overcome the band-gap of the material, the more conductive the material becomes. High resistivity semiconductors are less prone to leakage currents and detectors made from these materials have a higher signal to noise ratio [4].

The other important electronic property of semiconductors is the product of the material's carrier mobility (μ) and lifetime (τ). This property is a measure of how far excited charge carriers are able to travel in the material under the influence of an electric field before they recombine with an electron, hole, or a defect and this has a direct impact on the sensitivity of a detector. The mobility, measures how quickly an electron or a hole travels through the material under an electric field. Ideally, the drift length which is the product of the mobility, lifetime and electric field should be greater than the detector thickness to ensure full charge collection. However, the hole mobility is lower (~90 cm^2/Vs) compared to the electron mobility (~880 cm^2/Vs) which results in "hole tailing" [6]. Detector devices often suffer from incomplete hole collection which results in some charge loss during the sampling time, broadening of the measured energy spectrum of a given signal and a reduced current pulse. The carrier lifetimes in CZT have been

shown as an average of 100 ns to several microseconds for electrons and 50-300 ns for holes [6]. The electronic and mobility properties are also detailed and discussed in more depth in Section 4.4.1 (Photoluminescence) and Section 4.4.2 (Hall Effect in Semiconductors).

2.2 Growth Techniques

2.2.1 Vertical Gradient Freeze Growth Process

The samples studied in this thesis were grown by the Vertical Gradient Freeze (VGF) method. VGF is a melt growth process which uses 5N or higher purity Cd, Zn and Te material that is compounded and sealed in a graphite ampoule. The system is heated until the melting points of all three materials have been surpassed. This ensures that previously existing molecular structures have been destroyed and will not remain intact as they can lead to the formation of precipitates in the new matrix. Atmospheric control, achieved through a vacuum, ensures that a proper stoichiometry is maintained and a high resistivity material is produced. The material is then cooled and the temperature profile is adjusted in order to stabilize the growth interface. It is at that liquid and solid interface that the melt is most unstable and where one of the first defect origination mechanisms starts through the effects of segregation [7]. This stabilization is achieved by controlling the temperature profile electronically and melt replenishment, when required. In cases where the ampule or heater is translated to achieve the desired temperature field during the solidification phase, the crystal growth process is known as Bridgman growth [7].

2.2.2 Effects of Segregation

The electrical properties and conductivity of semiconductor crystals can also be controlled by the addition of certain dopant elements. These specifically chosen elements added to the melt and then incorporated into the solid crystal during the growth process, can be used to control the conductivity of the material. Common dopants for CdTe include indium, aluminum and chlorine for n-type material and phosphorous, lithium and sodium for p-type material [4]. However, during the solidification process, some of these added elements can become segregated at the solid-liquid interface of the material resulting in a non-uniform dopant distribution throughout the material [8]. These result in poor carrier properties and affect the detector performance.

Segregation occurs as a result of changing concentration of the dopant in the melt as the boule solidifies. At the beginning of the growth process the initial concentration of the dopant in the melt is C_o. At the start of crystallization, the concentration of dopants in the liquid will be the same as the initial concentration, $C_l = C_o$. As crystallization proceeds and a solid begins to form, the concentration in the liquid is offset due to concentration in the solid [8]. Progressively the liquid becomes richer in the dopant species or more depleted in the case of Zn. A compound's propensity for segregation is measured by the segregation coefficient number, k, which is the ratio of dopant concentration in the solid to the dopant concentration in the liquid (Equation 2.1) [8].

$$k = \frac{C_{Solid}}{C_{liquid}} \quad \textbf{2.1}$$

Segregation occurs in liquids with a coefficient not equal to one. The segregation coefficient for Zn in CdTe is 1.35. Even in an ideal case of perfect mixing within the liquid, the concentration in the solid is still at a higher level than the initial concentration C_o, of the liquid melt. An over-excess of rejected dopant at the solid-liquid interface remains within the boundary layer of liquid and leads to an increase of concentration in the solid too [8].

In addition, dopant accumulation in the boundary layer will result in a lowering of the melting temperature in this region. A steep thermal gradient is formed between the segregated dopant and uniform melt areas. This results in a super cooled region of the melt. At this critical concentration, super cooling is relieved by spontaneous solidification and the growth of dendrites. The dendrites close around segregated dopant clusters which can contains various defects too, such as Tellurium inclusions. In effect the trapping of Te inclusions and other defects leads to detrimental results for the resolution of CZT detectors [8]. The next section gives a brief overview of how defects lower the performance of detector arrays.

2.3 Types and Effects of Defects on Semiconductor Performance

2.3.1 Tellurium Precipitates and Inclusions

The most common defect originating from the VGF growth process is the formation of Te precipitates and inclusions. Origination of these defects occurs during the melt growth by two

distinct mechanisms: (1) the formation of droplet inclusions due to growth instabilities and (2) temperature dependant retrograde solubility (i.e. the tendency of a substance to become less soluble with higher temperatures) [9]. Detrimental effects caused by Te precipitates result in the introduction of stress by distortion of the surrounding lattice and also act as non-radiative recombination centers for carriers. These particles are often associated with radial strain fields, dislocation loop punching and faceted shapes [9, 10]. Additionally, the presence of Te droplets results in less transmittance and degraded electrical properties because solid Te has a band gap of ~0.33eV, which is much lower than the surrounding CZT matrix. As a consequence, higher leakage currents found along grain boundaries are attributed to the high density of conducting Te inclusions [11]. A typical scatter of Te inclusions, imaged using IR transmission microscopy, is seen in a 10% CZT material (Fig. 2.2).

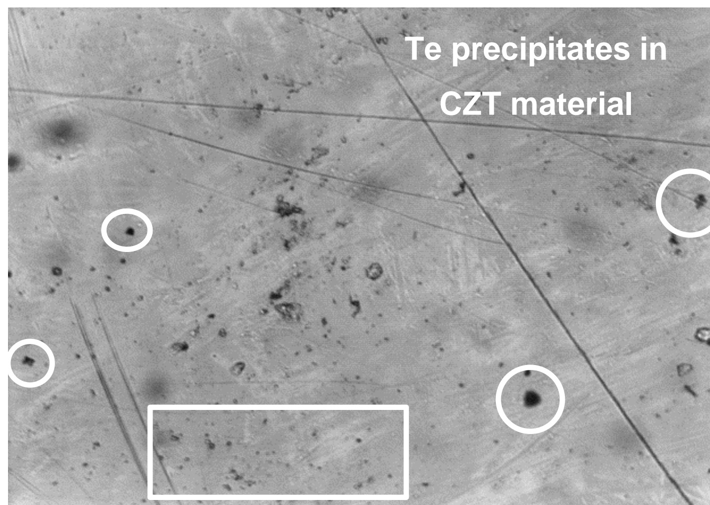

Figure 2.2: Te precipitates are visible in the CZT matrix because they are not transparent in the IR

C.H. Hanager Jr. et all (2009) [9] showed that the specific orientation of Te precipitates in the surrounding CZT matrix occurs on low energy planes ({111}, {110} or {100}). These researchers imaged CZT using backscatter SEM and showed that: (1) the Te precipitate shapes are approximately tetrahedral with faces corresponding to the {111} growth planes of cubic CZT matrix, (2) the elemental Te's crystalline axes have a relationship with the host axes and crystal faces and (3) Te particles have relatively large (~30% of volume) voids [9].

2.3.2 Pipes and Wires

The second most common defect observed in CZT is the formation of hollow tubular defects known as pipes. Pipes are commonly found running intermittently and parallel to the growth axis of the CZT ingots. A higher density of pipes is usually observed at the top of the ingot with a decreasing density towards the bottom of the ingot [12]. Salez et al (1998) [12] indicated that pipes form by two mechanisms during the growth: (1) pipes are caused by solute trails left by excess Te and (2) pipes occur as a result of dissolved gases coming out of the solution as the crystal cools. The pipes are usually several mm to a few cm in length and have a width of 20-50 microns. These typically appear hollow and can trap foreign contaminants during process like acquiring contact materials such as gold. Moreover, thinner pipe-like structures, also called wires, form in the solid and are typically observed at triple junctions (regions of three of more intersecting grains) inside the CZT boule. They are made up of continuous Te precipitates, which can act as a short circuit if they extend between the cathode and anode. Pipes and wires tend to form at the higher end of the boule earlier on in the growth process, as the solidification gradient of the material travels from the bottom to top ends of the boule [12].

2.3.3 Other Common Defects in CZT (Cracks, Grain Boundaries and Twins)

Cracks results from the excess thermal stress during the cool down process. The cracks observed in previous studies by T.E. Schlesinger et al (2001) [4] have ranged in length from ~ 25 um in width to several cm. They were found to originate from the edges of the crystal and propagate toward the center of the ingot. It is thought that the excess stress developed from the adhesion between the crystal and the crucible wall during the solidification process gives rise to nucleation sites for the crack propagation. In addition, cracks can occur when the material is being sliced and cut during the manufacturing stage.

Another common defect in CZT is twinning caused by the partially ionic nature of CZT bonding which favours a low stacking energy. Twin planes with (111) orientations are found in nearly all CZT crystals. High dislocation densities and twinning have both been found to impact the device efficiency and yield. Electrical response studies by C. Szeles at al (1998) [10] using a single channel analyzer and a ^{57}Co source showed almost zero response from regions along large angle grain boundaries, when compared to a high response inside grains. Cracks propagating inside the

grains also gave a nearly zero response. However, no correlation was found between lowered performance and the high presence of twin boundaries, indicating that twins have a negligible effect on the electric field and charge collection in CZT devices [10].

Chapter 3
Structural Characterization

3.1 Theory

3.1.1 X-ray Diffraction

X-ray diffraction is a non-destructive method of analysing the crystal structure, lattice constant, strain and composition of a material [13]. X-rays are emitted toward the specimen (usually using a Cu source) and used to probe the lattice as radiation scatters from the interaction with the electron cloud surrounding each atom. At a time when the path difference of each wave (nλ) is equivalent to 2dsinθ, constructive interference occurs and this is known as the Bragg condition given by Equation 3.1 [13]:

$$2dsin\theta_B = n\lambda \qquad \textbf{3.1}$$

where d is the atomic plane spacing, $\theta_B$is the Bragg angle, λ is the X-ray source wavelength and n is any integer. Bragg's law is used to calculate the atomic plane spacing by using the value of the experimentally obtained Bragg angle, θ_B. This is shown in Figure 3.1.

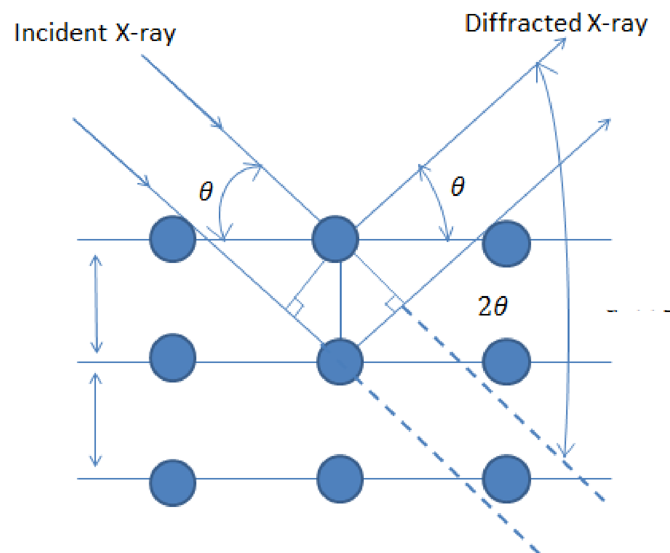

Figure 3.1: Bragg's law showing the constructive interference of waves scattered from two parallel planes

The reflection as a function of angle near the Bragg angle carries information about the crystal structure and defects present in the material [13].

3.1.1.1 Reciprocal Space

Each set of crystal planes in real space is associated with a diffraction spot in reciprocal space. In order to plot the reciprocal lattice, a vector perpendicular to a particular set of planes is drawn from the origin. This vector has a magnitude of 1/d and describes the interplanar spacing [14]. A point is plotted at the end of each vector until a 3-D periodic array of reciprocal lattice points is established. Due to the reciprocal relationship between reciprocal and real space, small plain spacing in real space become large in reciprocal space. As a result, any factor which alters the spacing will be reflected in the position of the Bragg spots and can be used to calculate the atomic lattice spacing.

The reciprocal lattice can be probed by the scattering vector, s. This vector is obtained from the difference between the incident vector (k_o) hitting the sample and the reflected vector, k_r. The length and orientation of a scan can be changed by varying the reflected vector angle 2θ and the angle at which the incident beam hits the sample ω. The reciprocal lattice can be thought of as being attached to the crystal because if the crystal moves with respect to the incident beam, so does the crystal lattice. The locations at which the Bragg condition is satisfied lie on the Ewald sphere of reflections. The radius of the Ewald sphere is 1/λ, where λ is the wavelength of the probing signal. This sphere represents the regions of the reciprocal space, which can be explored given a certain angle theta and a particular wavelength λ. The maximum possible length of s is 2/λ, which is twice the length of the incident vector, k_o. Not all of the reflections can be accessed as some of them are blocked by the crystal. In addition, the allowed reflections from each crystal structure are determined by the atomic scattering amplitude and the structure factor (see Section 3.1.1.2).

3.1.1.2 Structure Factor

The type of diffraction pattern which forms depends on the crystallographic orientation and symmetry of the crystal. The intensity of the scattering of the x-rays reflected back at the Bragg angle is determined by the structure factor. The structure factor is the combined equivalent from

all the scattering amplitudes of each individual atom in the unit cell. The scattering amplitude (A_{cell}) from the unit cell is given by Equation 3.2:

$$A_{cell} = \frac{e^{2\pi ikr}}{r}\sum_{i} f_i(\theta)e^{2\pi iK\cdot r_i} \qquad \textbf{3.2}$$

According to Equation 3.2, all the atoms within the unit cell scatter with a phase difference given by $2\pi iK \cdot r_i$, where r_i describes the position of each atom in the unit cell [15]. This expression can be shown to equal the structure factor F_{hkl} (Equation 3.3).

$$F_{hkl} = \sum_{i} f_i e^{\frac{2\pi i}{a}(hx_i+ky_i+lz_i)} \qquad \textbf{3.3}$$

where h, k and l are the Miller indices of the Bragg reflection. Equation 3.3 is valid for all sizes and symmetries of unit lattice cells, whether the unit cell is made from one atom or over a hundred. The position in reciprocal space of the constructive interference, or “reflections”, is determined by the location of the atoms within the unit cell. For a face centered cubic structure, like CZT, the atom coordinates are:

$$(x,y,z) = (0,0,0), (\tfrac{1}{2},\tfrac{1}{2},0), \left(\tfrac{1}{2},0,\tfrac{1}{2}\right), \text{ and } (0,\tfrac{1}{2},\tfrac{1}{2})$$

Substituting these values into Equation 3.3 shows that if all three values of the h, k and l indices are either odd or even, then all of the exponential terms will be equal to $e^{2n\pi i}$. This results in the diffracted waves being multiples of 2π and being in phase. This condition produces allowed reflections for this structure. However, if one of the h, k and l indices is odd and two are even, or vice versa, this will result in odd multiples of π and two terms of -1. In this case, the structure factor is zero and there is no reflection at the corresponding Bragg angle [15].

In the case of the CZT samples, the [111] oriented samples can be directly scanned for a [111] Bragg predicted reflection. However, the [211] samples do not produce a reflection for a zinc blend structure having one even and two odd indices due to a lack of signal constructive interference. This means that a [422] Bragg condition must be used to produce a signal. The [422] plane is a higher order plane parallel to [211] and has a more narrow FWHM width.

3.1.2 Transmission Electron Microscopy

The transmission electron microscope (TEM) is used for high resolution imaging of small objects at the nano and pico scales. The advantage of this instrument, over conventional optical microscopes, is that it is not limited by the wavelength of visible light (400 nm - 700 nm) since the electron has a much smaller wavelength (1.23 nm at 1 eV) [15]. As high energy electrons pass through the crystal interacting with atoms in the material, inelastic and elastic scattering occurs. Analysis of each scattering type can be used to learn about different properties of the material [15].

3.1.2.1. Kikuchi Diffraction Patterns

Inelastically scattered elections lead to the formation of Kikuchi diffraction. Kikuchi diffraction patterns occur in thicker samples (several nm) due to availability to generate more scattered electrons which travel in all directions. These electrons become Bragg diffracted by the crystal planes as the incident beam ends up producing a parabolic Kossel cone diffracted beam. In regions near the optical axis, a direction in which a ray does not undergo double refraction, these parabolic cones appear as two parallel lines [15]. Kikuchi lines provide important crystallographic information about the sample such as: (1) information about the direct real-space crystal lattice via the Kikuchi band positions, (2) the reciprocal lattice via the band widths and (3) the physical crystal structure via the band intensity. Additionally, Kikuchi bands can be used as “maps” or “roads” to navigate the crystal as they are attached to a specific location which does not change as the crystal is rotated. Travelling from one location to another is made possible by the presence of zone axes. A zone axis is formed when two or more Kikuchi lines intersect. In real space, a zone axis represents a lattice row parallel to the intersection of two (or more) families of lattice planes. Tilting the crystal by a known angle allows for moving from one zone axis to another. This property of diffracting crystals can be used to orient the sample along a particular crystallographic axis [16]. The location of the Kikuchi lines can also be used to calculate the deviation parameter and to identify the orientation of the specimen [17].

3.1.2.2 Convergent Beam Electron Diffraction (CBED) Imaging of Higher Order Laue Zone (HOLZ) Lines

Coherent elastically scattered electrons are used to form Higher Order Laue Zone (HOLZ) Lines. HOLZ lines become visible under a convergent beam electron diffraction (CBED) condition. CBED is a method of producing high resolution images over a focused area. The regions sampled by CBED are a function of the beam probe size of incident electrons from the cone shaped intensity (convergent beam) and the diffuse elastically scattered electrons at Bragg angles. HOLZ lines come in pairs, similar to Kikuchi lines, with bright excess lines seen in the HOLZ hkl plane maxima and the dark (not visible lines) in the 000 disk [18]. The difference between the formation of Kikuchi lines and HOLZ lines is illustrated in Fig. 3.2a and Fig.3.2b.

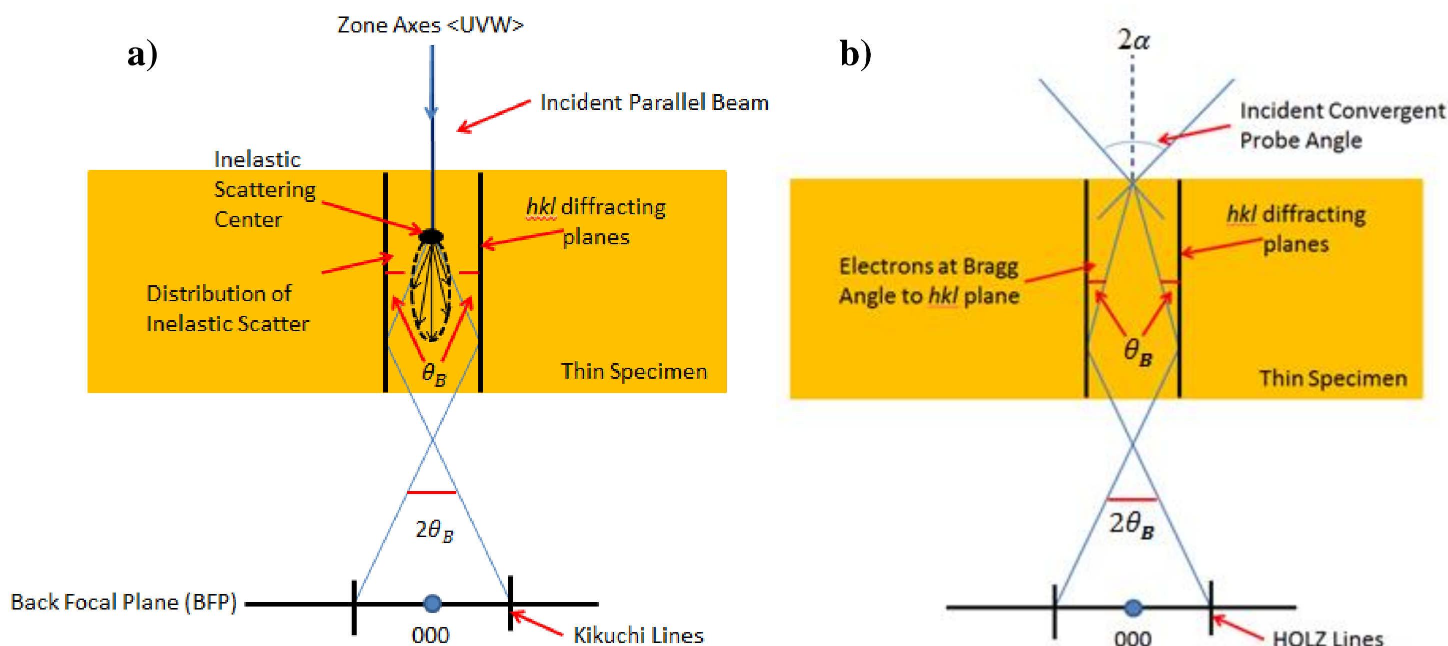

Figure 3.2: Schematic showing the difference between the formation of Kikuchi lines due to inelastic scattering in (a) and the formation of HOLZ lines with elastic electron scattering in (b)

The beam used to produce HOLZ lines converges on the specimen over an angular range of 2α, as the Ewald sphere is rotated at 2α about the origin. This allows for a wide range of sampling for existing HOLZ lines. This method allows for many ordered planes to be observed and thus the strained state of the crystal can be interpolated due to the sensitivity to the change in lattice

parameter. The sensitivity in the vector beam, g, to a change in the lattice constant is given by Equation 3.4 [15].

$$|\Delta g| = -\frac{\Delta d}{d^2} \tag{3.4}$$

where d is interplanar spacing and Δd is the change in interplanar spacing due to strain in the crystal lattice. This strain causes the HOLZ lines to split. The split in HOLZ lines is attributed to the presence of non-uniform atomic displacement along the beam direction and the reflectance of the beam at the Bragg angle [15]. An accurate measurement of the split in the HOLZ lines provides the highest resolution analysis of strain in crystals at a given point in the sample.

3.1.2.3 Phase Contrast Imaging

Phase contrast imaging is used for lattice imaging of the atomic arrangement in the material. Thin-sectioned specimens are irradiated with a parallel electron beam, which passes through an aperture and results in the electrons being scattered or transmitted through the material. The difference between the phase of the scattered and transmitted waves can be interfered to form interference fringes. This two beam imaging condition and multiple beam imaging at a zone axis, an intersection of atomic planes in real space, use the interference fringes to create a lattice image which is visible at a magnification of 100,000x or more. Lattice images are useful in studying the atomic arrangement and better understanding the types of defects present in the material [19].

3.1.3 Wet Chemical Etching

Wet chemical etching is a simple and cost effective process used to gauge the crystal quality of a semiconductor material. The etching process is used to reveal etch pits, which mark the locations of dislocations terminating on the surface of the material [20]. The efficiency of the etching process is determined by the mass transport of reactants or products in the solution, while the rate is determined by the kinetics of the surface reactions. In each etch, one of these processes is usually dominant [21]. If the mass transport is the prevalent mechanism, then the etching rate will be determined by the hydrodynamics of the system and the surface will not be sensitive to the crystallographic orientation or the surface morphology [20]. In the case of CZT, the dominant process of etching is dependent on the surface kinetics because the results of the etching process

are very sensitive to the surface orientation [21]. Different crystal faces, such as $(111)A_{Cd}$ or $(111)B_{Te}$, will dissolve at different rates and also produce different quality or no results depending on the crystallographic orientation.

The etching methods used with CZT work by oxidation of the surface followed by dissolution of the oxide. In this process, valence electrons are removed from the surface bonds by an active agent in the etching solution. The oxidizing agent is used to remove the bonding electrons from the valence band. This can in a sense be viewed as "injecting holes" into the solid. When these holes localize at the surface, they cause the rupture of surface bonds. The bonds in the etching agent and solid are broken and new bonds are formed; however, this does not involve free holes [22]. This study used three types of etchants which are discussed next.

3.1.3.1 2% Bromine Methanol Etch

The 2% Bromine methanol (volume) is a standard etch used for removing oxides from the surface of CZT samples. This type of etch is commonly used before X-Ray diffraction (XRD) or photoluminescence (PL) experiments in order to clear the surface of the oxide layer which can act as a non-radiative recombination center for electron hole pairs. Etching CZT, using Br/MeOH, leads to the formation of Te metal and the depletion of Cd from the surface sub-layer. This etchant is also anisotropic, preferentially etching the surface on the 111B face (Te) faster than the 111A face (Cd) [23].

The process works by the absorption on the surface of Br_2 molecules present in the solution. The redox potential between the Br_2/Br^- species is high and this reacts with the Te anions to give negatively charged ions and neutral Te^0. Due to the presence of Br anions, Cd^{2+} species pass into the solution forming $CdBr_2$, leaving elemental Te on the surface. This results in the removal of the Cd sub-lattice and the left over Te sub-lattice, which is now comprised of Te^0 with dangling bonds. This stoichiometric imbalance results in an unstable system that self-stabilizes by atomic rearrangement. The Te atoms are drawn together, forming clusters. Since the atoms in the clusters have a smaller minimum distance between the Te anions than in CdTe, the cluster formation disrupts the matrix leading to non-uniform etching and the appearance of pores on the surface. These pores allow for the Br anions to penetrate deeper into the material, thus etching

the material to a greater depth. This enables removal of Cd atoms from deep inside of the material and favours transfer of Te atoms into the solution [23].

3.1.3.2 Nakagawa Etch

The Nakagawa etch has been very effective in showing etch pits on the (111)A (Cd) face but not on the (111)B (Te) face. For this reason, it has actually been used as a distinguishing agent for the polarity of the faces. The reason this type of etch has been found to work on the cadmium side is due to the higher reactivity of these species. The standard concentration of Nakagawa is a 3:2:2 HF:H_2O_2:H_2O ingredient ratio by volume. However, previous work by F. Semendy et al (1999) [24] has showed that changing the solution concentration to a 4:0.5:2 of HF:H_2O_2:H_2O ingredient ratio has also produced successful results on the (111)B (Te) face. This was shown to work due to a three-fold reduction of the oxidizing agent [24].

3.1.3.3 Everson Etch

The Everson etch is made using 2:2:3 ratio of HF:H_2O_2:lactic acid. This etch is effective in showing pits on both the $[111]_{Cd}$ and [211] oriented crystal surfaces. The role of the HF and peroxide is to oxidize the surface, breaking surface bonds and disassociating the Cd ions into the solution, while the function of the lactic acid is to act as a buffer, a pH controlling agent which moderates the acid reaction in the solution [25].

3.2 Experimental Method

3.2.1 X-ray Diffraction

The high resolution X-ray diffraction measurements were performed using the Bruker D8 Discover Diffractometer. X-rays are emitted from a copper source at a wavelength of 1.54056 angstroms. Samples are mounted onto the holding plate using vacuum suction provided by the machine. The Bruker system has a capability of aligning 5 axes of rotation (x, y, z, phi and chi) and allows for movements as small as 0.001 degrees. The system is equipped with two detectors. The variable optic detector provides a lower resolution with a highest intensity and the Ge220 analyser crystal provides a higher resolution with a lower intensity. All 29 samples, in both the [111] and [211] orientations were examined using coupled ω-2θ scans.

3.2.2 Transmission Electron Microscopy

The Hitachi HF-3300v scanning transmission electron holography microscope (STEHM) at the University of Victoria was used to set up three imaging conditions: (1) Kikuchi diffraction patterns used to map the crystal, (2) a CBED pattern with HOLZ lines showing the strain in the material and (3) a two beam phase contrast imaging condition used to view the arrangement of the atomic planes. The TEM specimen was made from a [111] oriented CZT sample, prepared using a focused ion beam (Hitachi FB-2100) system, and mounted onto a single tilt sample holder. Details about the sample preparation are included in Appendix A.

3.2.3 Wet Chemical Etching

The first step in the etching study was to fine tune the process and etching duration for each type of etch. Several trial samples were used and etched for slightly different lengths of time, varying between 60 seconds and 120 seconds. Each sample was viewed under an Olympus U-CMAD3 model optical microscope and examined for formation of etch pits. Several test samples were used to dial in an optimal etching time, which was found to be 100 seconds. The chemicals for both etches were mixed in a large batch before starting each experiment such that any concentration discrepancies would be spread throughout the entire sample population.

The procedure for the Nakagawa etch was modified by the addition of a 2% Bromine Methanol (2% Br-MeOH) solution for rinsing. This was suggested by Dr. Neil Armour from the UVIC Crystal Growth Laboratory who experimentally showed that rinsing with 2% Br-MeOH after doing the Nakagawa etch removed the oxide layer from the surface allowing for better observation of the pits under the optical microscope. The following procedure was used:

1. Each sample was placed in a Teflon etching basket and dipped into the Nakagawa solution for exactly 2 minutes. The solution was not stirred or agitated during this time.
2. The basket was removed and dipped into a beaker full of deionized (DI) water for a few seconds to dilute the acids and stop the etching reaction.
3. The basket was then dipped into the 2% Br-MeOH solution for 2-5 seconds without stirring or agitating it.

4. Lastly, the basket was consecutively dipped in two methanol beakers which were used to rinse the 2% Br-Meth solution. The sample was removed and left to air dry on a Kim wipe.

The Everson etch process was followed exactly without any modification or addition of steps. The Everson etch procedure was as follows:

1. Each sample was placed in a Teflon etching basket and dipped into the Everson etch for 1 minute and 50 seconds. The etching solution was not stirred or agitated during this time.
2. The basket was removed and then rinsed in a beaker full of DI water.
3. The sample was removed from the basket and left to air dry on a Kim wipe.

The etch pits were then counted for six Nakagawa etched samples and four Everson etched samples. The Olympus U-CMAD3 optical microscope and camera set up was used to photograph different areas of each sample. The Nakagawa etch pits were visible using x10 magnification. The diameter of the area seen in the microscope's view at x10 magnification is 2 mm. The Everson etch pits were smaller and required a x100 magnification and the diameter of the visible area was 0.02 mm. The average etch pit density for each sample was found by taking the average of the number of counted pits in two locations. This was done for each sample.

3.3 Results

3.3.1 X-ray Diffraction Results

The [111] and [211] samples were studied using X-ray diffraction and the FWHM and Zn concentration in the material were calculated. A coupled ω-2θ scan was used for both orientations. The [111] oriented samples were scanned on the [111] plane; however, the [211] samples were scanned on the [422] plane because [211] is a forbidden reflection in FCC materials [13].

3.3.1.1 XRD Peak Position and Zinc Concentration

The XRD data was used to calculate the lattice constant for each sample by using Bragg's Law (Equation 3.1) and the known XRD copper source wavelength of λ = 0.154051 nm. The geometric properties of a cubic crystal structure were used to calculate the spacing between the

atomic planes, d_{111}, according to Equation 3.6, where a is the lattice constant and h, k and l are the Miller indices.

$$d_{111} = \frac{a}{\sqrt{h^2 + k^2 + l^2}} \quad \textbf{3.6}$$

The Zinc concentration (%) was calculated by linearly interpolating from Vegard's Law (Equation 3.7), where a_{ZnTe} and a_{CdTe} represent the theoretical lattice constants of ZnTe and CdTe, respectively.

$$a_{CZT} = xa_{ZnTe} + (1 - x)a_{CdTe} \quad \textbf{3.7}$$

The accepted values of a_{ZnTe} and a_{CdTe} are 0.6104 nm and 0.6481 nm, respectively [27]. The distribution of Zinc for all samples is seen in Fig. 3.3a, and then data is split up showing only [111] samples (Fig. 3.3b) and then only [211] samples (Fig. 3.3c), respectively.

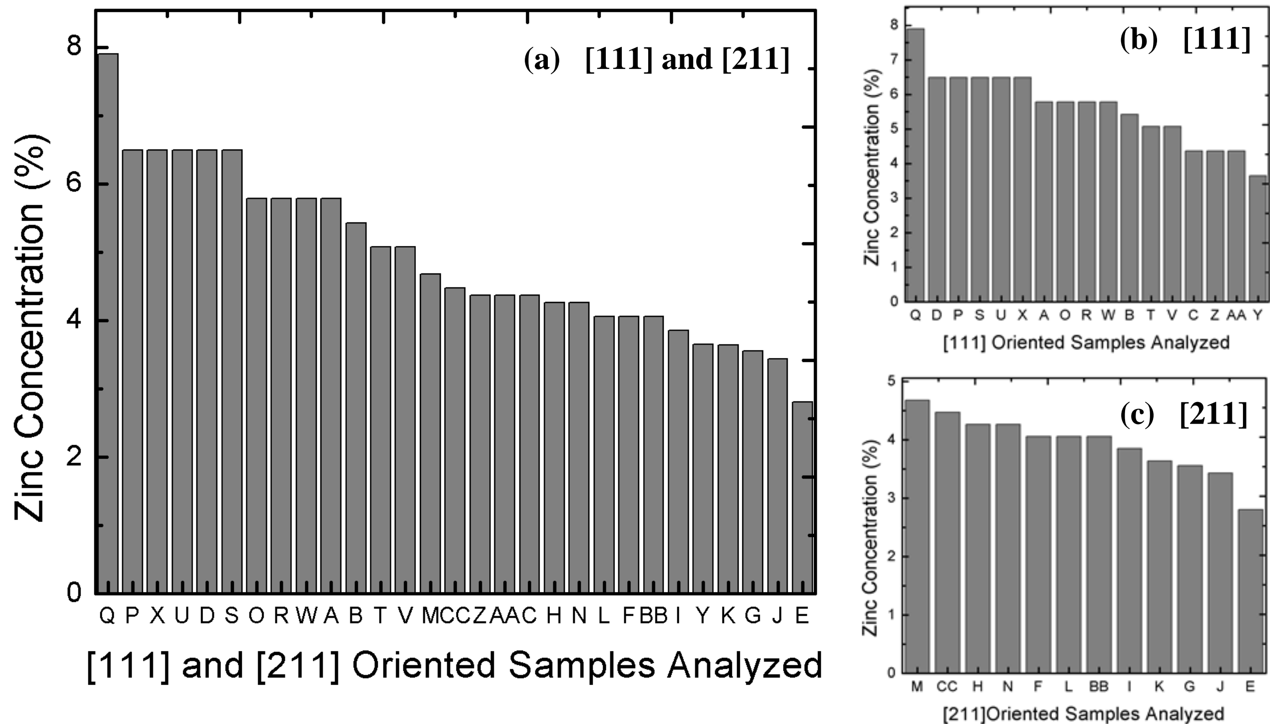

Figure 3.3: (a) Zinc concentration (molar) variation between all 29 samples, (b) [111] oriented samples only and (c) [211] oriented samples only

The Zinc distribution was found to vary between 2.8% and 7.9%., with an average zinc concentration of 4.3%. The variation of Zn in the [111] oriented samples was found to range from 3.7% to 7.9%, with an average of 5.18% and the Zn variation in the [211] oriented samples

was found to range from 2.8% to 4.7% with an average of 4.62%. The highest Zn concentration of 7.9% was observed with Sample Q in the [111] orientation, and the lowest Zn concentration of 2.8% was found in Sample E in the [211] orientation.

3.3.1.2 XRD Peak Shape and Full Width Half Maximum (FWHM)

All 29 samples, in both growth orientations, were examined using XRD. The XRD data revealed a wide variation in peak shapes, including peak splitting (Fig. 3.4a) and peaks overlapping on a large shoulder on one or both sides (Fig. 3.4b). Fig. 3.4c shows the peaks distribution and shapes found in the batch of [111] oriented samples.

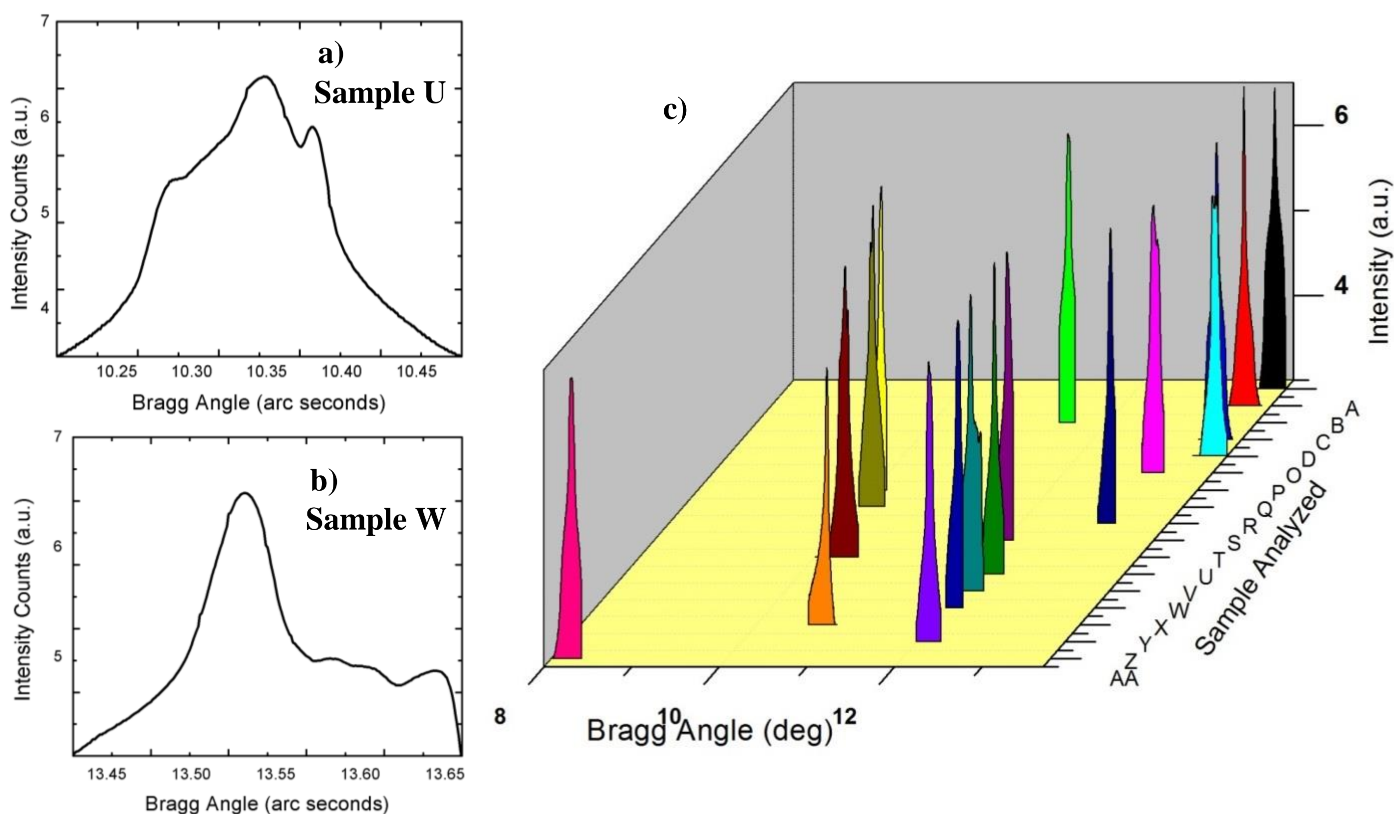

Figure 3.4: (a) Sample U showing an example of a splitting XRD peak, (b) Sample W showing an example of overlapping peaks with a shoulder and (c) variation in distribution for all [111] XRD peaks

On the other hand, it was found that no XRD peak splitting was prevalent in the [211] oriented samples. The peaks in the [211] orientation either had a single sharp peak attached to a shoulder on one or both sides (Fig. 3.5a), or a single sharp peak with no shoulder on either side (Fig.

3.5b). A comparison of the peak shape distribution (Fig. 3.5c) shows the distribution of peaks in both shape and also Bragg angle.

Figure 3.5: (a) Sample M showing an example of a single peak with a shoulder, (b) Sample N

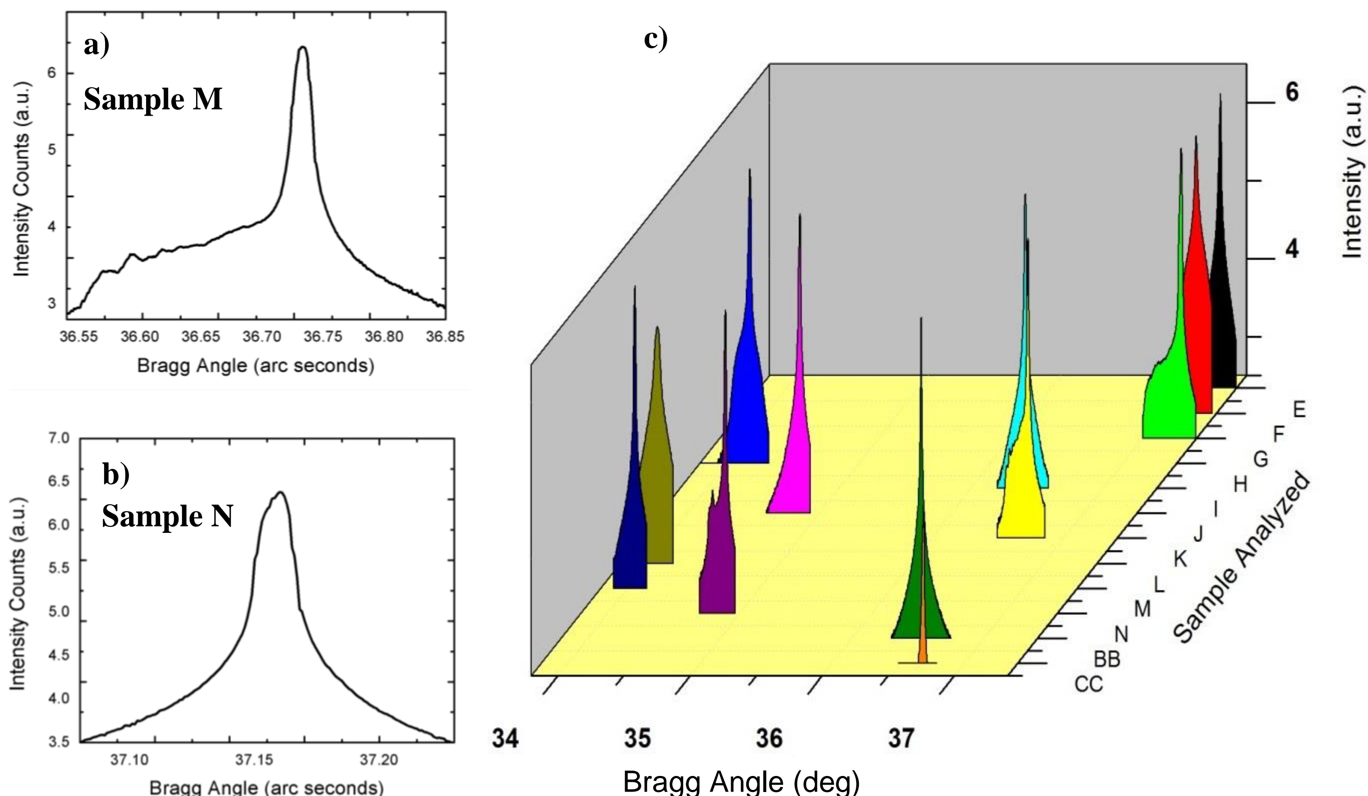

showing an example of a single peak without a shoulder and (c) variation in distribution for all [211] XRD peaks

In order to evaluate crystalline quality of the samples, the width of the XRD peak of the rocking curve was determined for all 29 samples. A 135 arc second distribution of FWHM values was observed between all 29 samples, [111] and [211] crystal orientations. Sample Z [111] was found to have the largest FWHM, 160 arc seconds, and sample BB [211] the smallest FWHM, 25 arc seconds, (Fig. 3.6a). The [111] sample distribution (Fig 3.6b) showed a 115 arc second spread between the respective samples' FWHM, while the [211] samples (Fig 3.6c, scanned on the 422 reflection) had a slight more densely clustered distribution spread of 101 arc seconds.

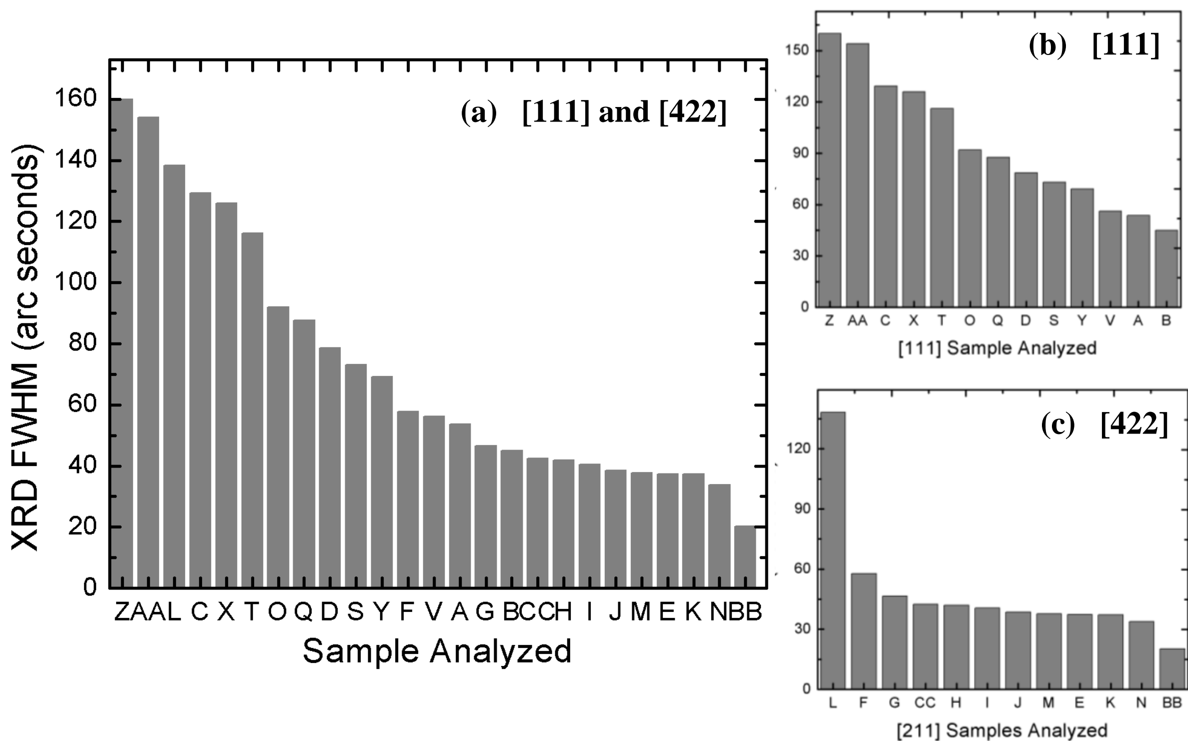

Figure 3.6: (a) Distribution of FWHM values for all [111] and [422] reflections of all samples, (b) only [111] reflections and (c) only [422] reflections

Samples P [111], U [111], W [111] and R [111] were omitted from Fig.3.6a and Fig. 3.6b. These four samples had distinctly split peaks, which did not provide a meaningful numerical measure of the XRD FWHM.

3.3.1.3 Reciprocal Space Mapping

Reciprocal space mapping (RSM), a method of gathering information about interplanar spacing and imaging defect-related XRD peak broadening, was used to study two samples. Sample T, oriented in the [111] direction (Fig. 3.7), was compared to Sample M, oriented in the [211] direction (Fig. 3.8).

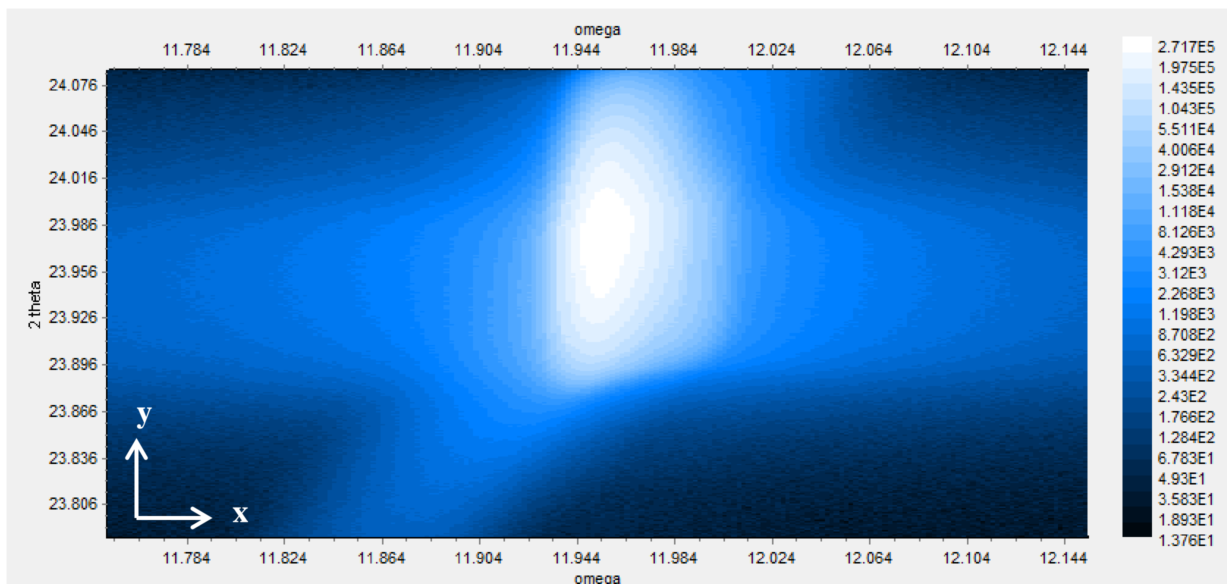

Figure 3.7: Reciprocal space lattice map of Sample T [111], FWHM = 116.25 arc seconds

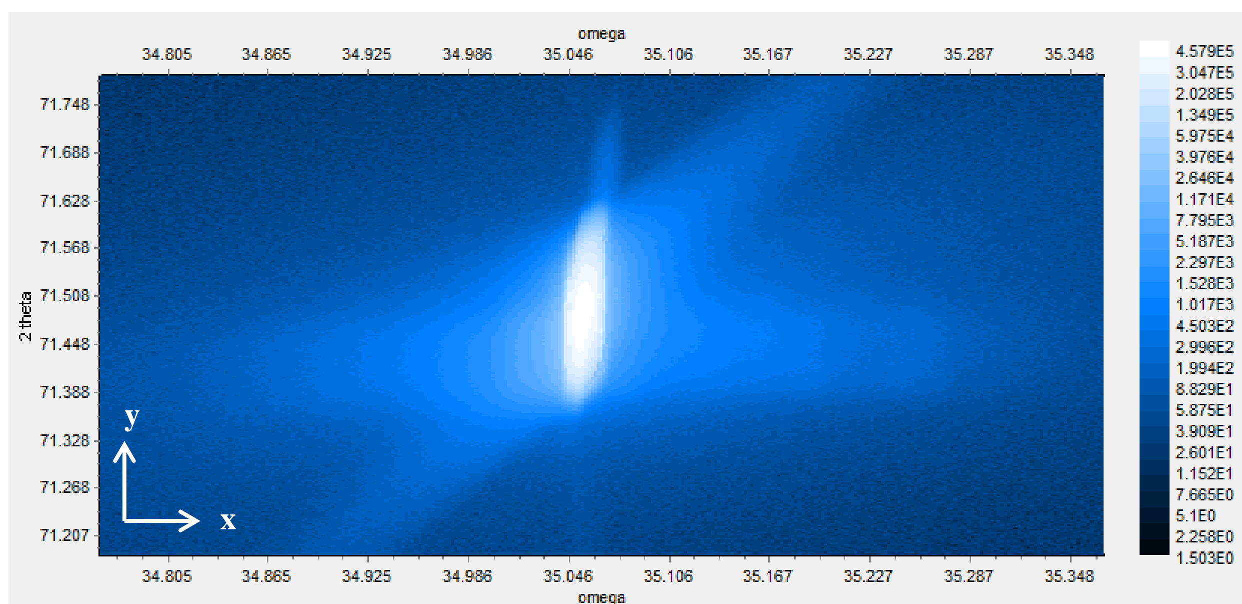

Figure 3.8: Reciprocal space lattice map of Sample M [211], FWHM = 37.68 arc seconds

The RSM for Sample T showed peak broadening in the horizontal X-X direction with a clearly defined intensity contour pattern. Sample M was found to have a narrow reciprocal space peak with an elongated pattern in the vertical X-Y direction. The RSM results for both samples were obtained using a ω-2θ scan. This type of scan rotates the x-ray source by ω and the detector by 2θ with an angular ratio of 2:1. In reciprocal space the length of the probing vector, S, changes but its direction remains the same. A ω-2θ scan provides more comprehensive information on

changes in interplanar spacing and strain induced by stress, than only performing a ω scan, which results in only a change of direction and not length for the probing vector, S, and traces an arc centered on the origin. [14].

3.3.2 Transmission Electron Microscopy Results

One [111] oriented sample was studied using TEM. This method allowed for obtaining diffraction patterns that were used to calculate the lattice constant in the material and to observe the variation in lattice constants between several neighbouring atoms. Variations in the lattice constants provided evidence that strain was present in the material. TEM was also used to image the strain field in the sample and to study the arrangement of the atomic lattice.

3.3.2.1 Kikuchi Lines and Map of Crystal

The [111] oriented sample was tilted through the full TEM holder range of -13° to +13°. The tilt was used to travel though the crystal going between three zone axes. The Kikuchi bands imaged in the single tilt holder correspond to the angles summarized in Table 3.1.

Table 3.1: Kikuchi bands related to the angle of tilt of the specimen holder containing the sample

Kikuchi Band	*Tilt Angle (^{o})*
G1	-0.3
G2	-1.2
G3	-3.7
G4	-5.2
G5	-8.5
G6	-14
G7	12.3

The tilt angles, along with Kikuchi diffraction patterns were used to create a Kikuchi map for the [111] oriented CZT sample (Fig.3.9).

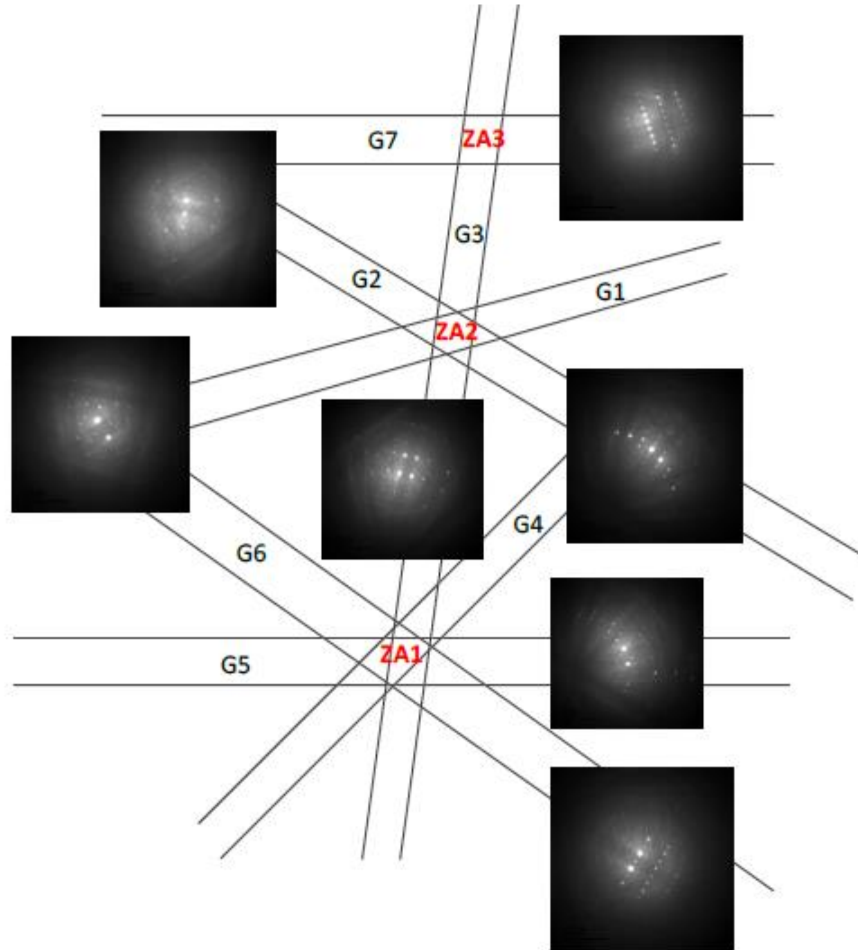

Figure 3.9: Kikuchi map of [111] oriented CZT sample obtained by tilting the sample from -13 degrees to +13 degrees and travelling between three zone axes (ZA)

Analysis of the Kikuchi Map (Fig. 3.9) revealed the presence of three zone axes (ZA). A ZA is the location where two or more Kikuchi bands intersect. ZA1 was found to be a major zone axis, while ZA2 and ZA3 are minor. In real space, a zone axis represents a lattice row parallel to the intersection of two (or more) families of lattice planes.

3.3.2.2 Lattice Constant Calculation

The local lattice constant was calculated by measuring the spacing between spots on a diffraction pattern (DP) taken at a zone axis and then indexing the diffraction pattern. The diffraction pattern obtained at ZA3 was analyzed by measuring the distances between the spots using the Gatan Micrograph software. The software was calibrated for the 0.3 m camera length with the settings given in Table 3.2.

Table 3.2: Software calibration for a 0.3m camera length

Distance [m]	*Power [kV]*	*Calibration [RLU]*
1	200	-0.0103181
0.3	200	-0.0343937

The spacing between the different diffraction spots was measured, in reciprocal lattice units (1/nm), using the calibrated camera length (Fig. 3.10).

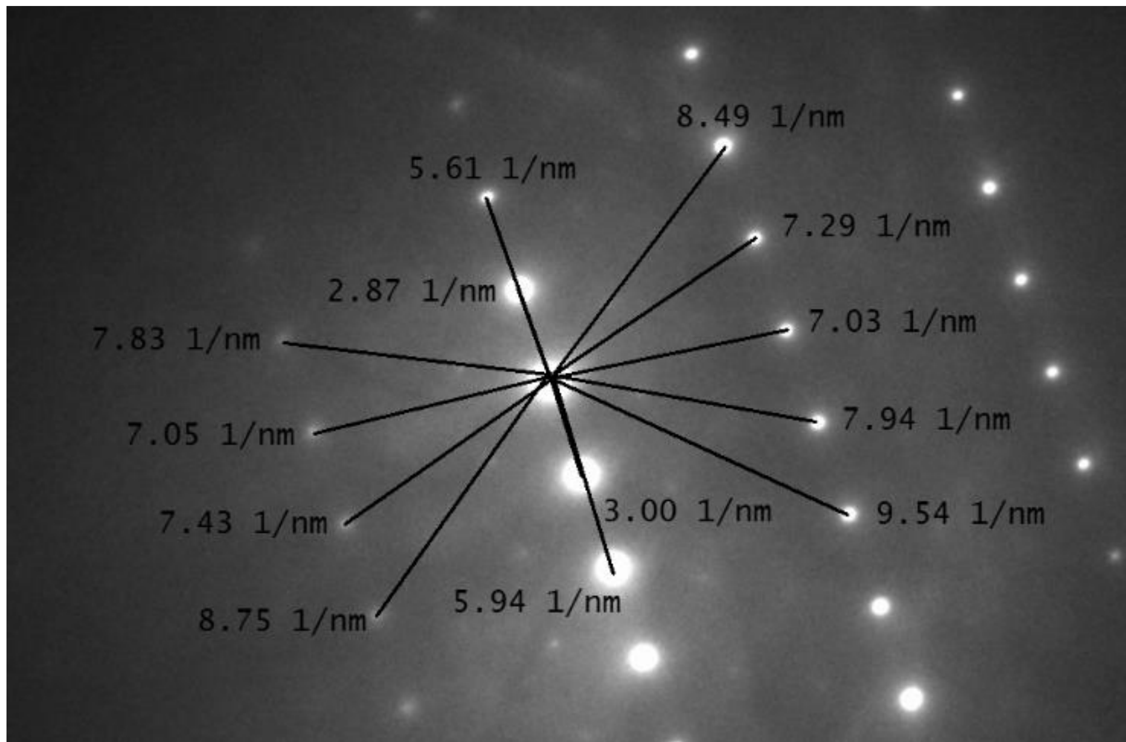

Figure 3.10: Diffraction pattern at ZA3 showing the distances between spots in reciprocal lattice units (1/nm)

Next, the diffraction pattern (DP) was indexed so the values for *h*, *k* and *l* indices of each spot are known. The DP was first compared with other commonly tabulated patterns for FCC materials. Out of twelve indexed patterns [28], the (123) diffraction pattern had the closest fit to the ZA1 pattern (Fig. 3.11).

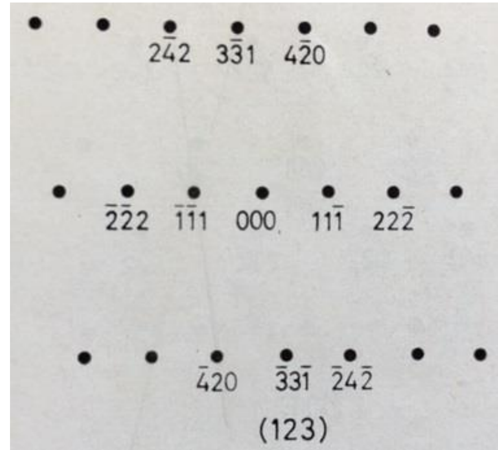

Figure 3.11: Tabulated (123) diffraction pattern for FCC crystals [28]

The theoretical plane spacing d_{hkl} was calculated using the accepted CZT lattice constant, a = 6.444 nm. The ratio between two d_{hkl} locations in Fig. 3.11 was calculated to be 2.5. The experimental ratio was then compared by measuring the same two *h*, *k* and *l* locations on the experimental DP (Fig. 3.10) and it was also found to be 2.5. The excellent agreement between theoretical and experimental values indicates that the DP was indexed correctly as (123). The lattice constant was then calculated using Equation 3.8, where R is the distance between diffraction spots, λ (1.97 pm) is the electron wavelength for the STEHM, *l* is the camera length (0.3 m) and d is the atomic spacing [15].

$$d_{hkl} = \frac{\lambda l}{R} \qquad \textbf{3.8}$$

The lattice constant *a* was found from Equation 3.9 [15] where each spot has the corresponding *h*, *k* and *l* coordinates from the indexing.

$$a = \sqrt{h^2 + k^2 + l^2}\ (d_{hkl}) \qquad \textbf{3.9}$$

The local lattice constant was calculated at four locations and the results are shown in Table 3.3.

Table 3.3: Local lattice constants calculated from the (123) zone axis diffraction pattern

Location	*Measured Lattice Constant [nm]*
331	0.740
420	0.645
111	0.720
242	1.16
Average	0.82

As can be seen by the results in Table 3.3, there is a wide range of variation in the local lattice constant. This variation can result from misalignment with the eucentric height and a contribution from strain in the material.

3.3.2.3 Convergent Electron Diffraction (CBED) Results

The variation of the local lattice constant observed for the (123) diffraction pattern suggested that the sample was under strain. A CBED pattern was used to observe the HOLZ lines and qualitatively examine the strain present in the sample. Fig. 3.12a shows the splitting and bending of HOLZ lines caused by a precipitate in the matrix. Fig. 3.12b shows another region of the sample which is under strain due to surface contamination, seen as a black pattern in the bottom left corner, and Fig. 3.12c that shows bending of the HOLZ lines around the shape of a precipitate.

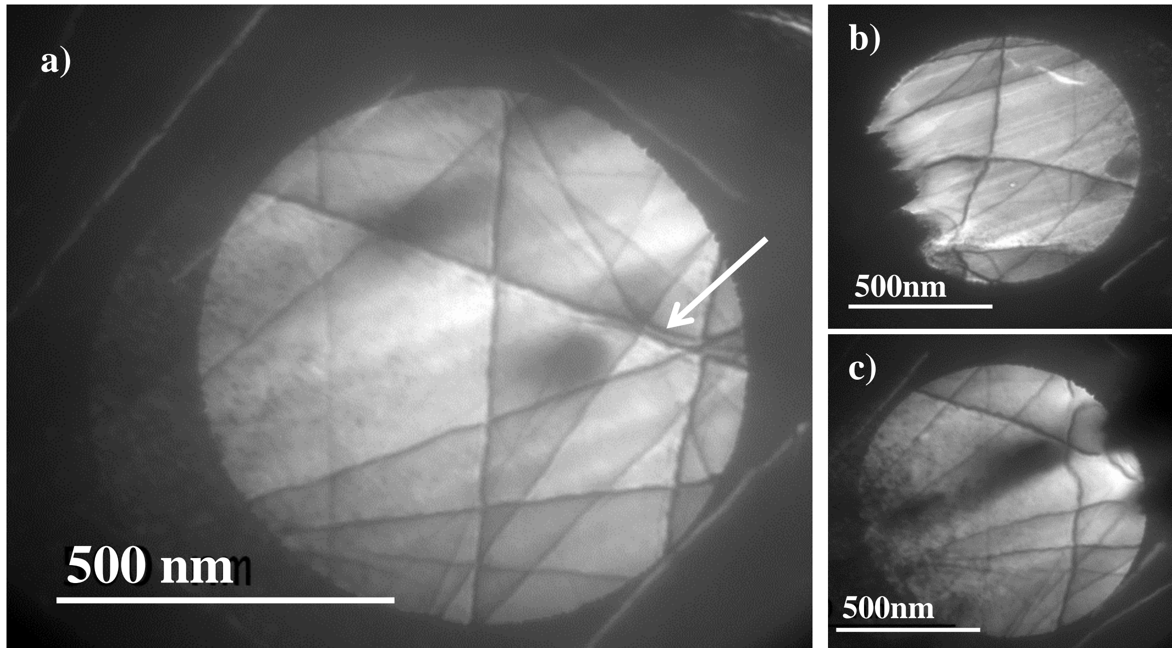

Figure 3.12: (a) Splitting of HOLZ lines, noted by white arrow, due to the strain induced by the precipitate, (b) impact of contamination on the strain in the material and (c) bending of HOLZ lines around a precipitate causing a high strain region

The HOLZ lines physically represent the atomic planes in the crystal and can reveal how the internal structure of the lattice is affected by the presence of precipitates. In addition, the strain in the crystal is affected by lattice mismatch at the interface between the sample and the contamination, caused by the re-deposited material during the FIB manufacturing stage.

3.3.2.4 Phase Contrast and Lattice Imaging

The STEHM was used for lattice imaging by setting up a two beam phase contrast imaging condition. Fig. 3.13a shows a lattice image which captured several dislocations, shown in close ups in Fig. 3.13b and Fig. 3.13c.

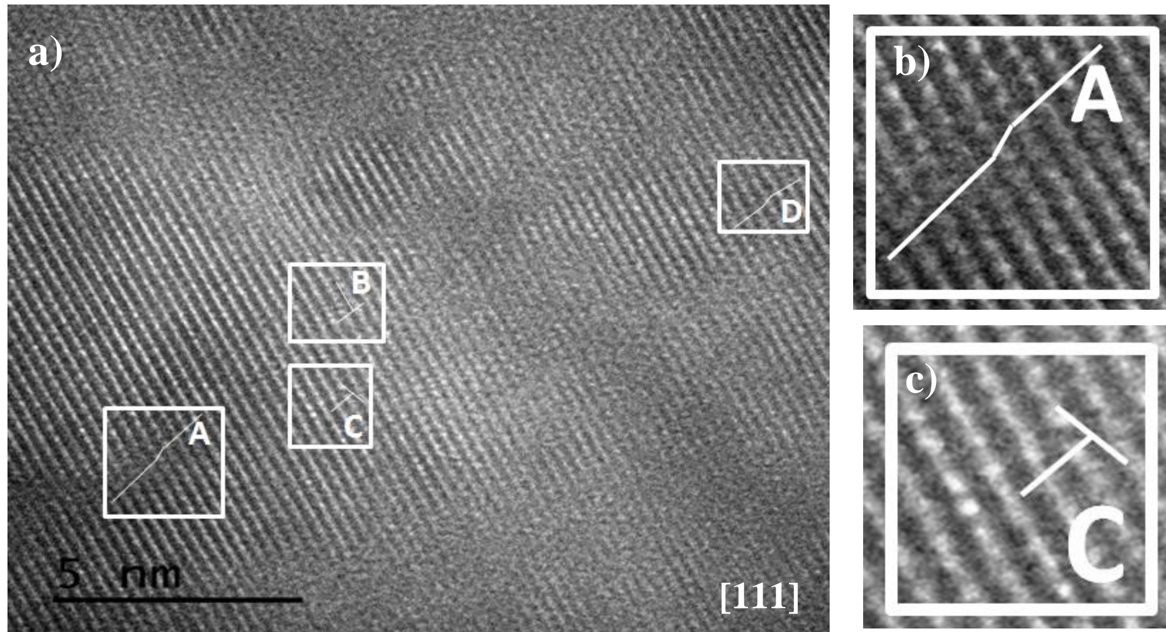

Figure 3.13: (a) Lattice image of [111] oriented CZT sample showing four regions (A, B, C and D) with dislocations, (b) close up of a dislocation and (c) close up of an edge dislocation

The regions in Fig. 3.13a marked as B and C show examples of an edge dislocation. An edge dislocation occurs when an extra plane of atoms is inserted into the matrix. Regions A and D, in Fig. 3.13a, show an example of a dislocation. Edge, screw or a mix of both dislocations also occur when slip due to shear stress is present in the crystal [29].

3.3.3 Wet Chemical Etching

Wet chemical etching is an efficient way to gauge the defect density in a material. The purpose of the etching experiment was to calculate the etch pit density (EDP) and to identify types of defects present in the material by studying the shapes, sizes and configurations of the pits.

3.3.3.1 Nakagawa Etch

The Nakagawa etch revealed etch pits only on the (111) Cd face. Each sample was viewed using the Olympus U-CMAD3 microscope on the top and bottom, and only one side on each sample was found to contain etch pits. The etch pits were visible at x10 magnification and were evenly scattered throughout the surface. Only two sizes of triangular etch pits were observed, 0.013 mm (small etch pits) and 0.027 mm (large etch pits). They both looked identical in shape but varied

in size. Figure 3.14 shows an example field of view, the types of etch pits present and the size difference between the smaller and larger pits.

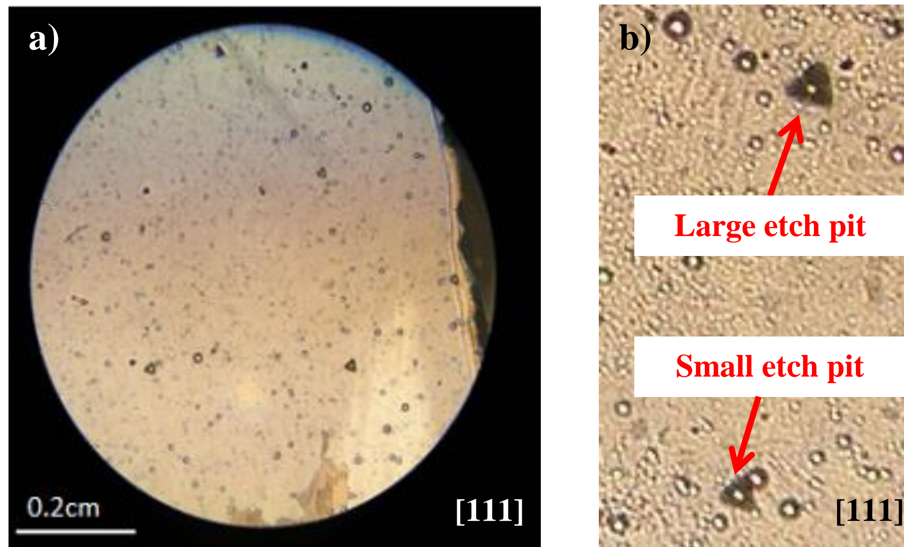

Figure 3.14: (a) Example field of view of Nakagawa pits visible at x10 magnification and (b) close up of smaller and larger triangular etch pits observed in the material

The number of etch pits at two locations on each sample were counted and an average result was used in the calculations. The results for the EPD are summarized in Table 3.4.

Table 3.4: Nakagawa etch pit density results for six [111] oriented samples

Sample	*Orientation*	*Counting Area [mm²]*	*Counted Pits Area 1*	*Counted Pits Area 2*	*Pit Density [1/cm²]*
A	[111]	6.28	6	7	103
C	[111]	6.28	4	7	88
Q	[111]	6.28	15	10	199
S	[111]	6.28	4	8	95
Y	[111]	6.28	9	11	159
Z	[111]	6.28	8	13	167

In addition, four [211] oriented samples were etched using the Nakagawa solution; however, no etch pits on either the top or bottom surface were observed.

3.3.3.2 Everson Etch Results

Four samples, two in [111] and two in [211], were etched using the Everson solution. The Everson etch produced very good results on both the [111] Cd and [211] oriented samples which were visible with x100 magnification using the Olympus U-CAD3 microscope. The etch pits were highly symmetrical and very easy to identify. Unlike the Nakagawa samples which had pits that all looked the same, the Everson etch pits had several shapes. In addition to the difference in shape, the etch pits were either evenly distributed throughout the sample (Fig. 3.15a) or clustered in some areas (Fig. 3.15b).

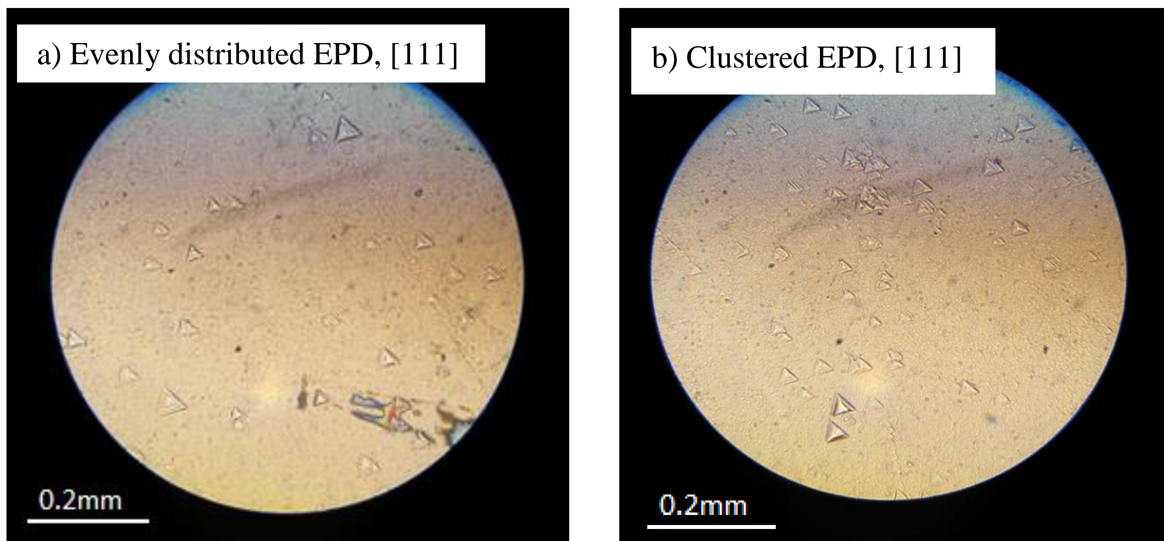

Figure 3.15: (a) x100 magnification view of evenly distributed EPD and (b) a view showing areas of EPD clusters (right)

Six distinct types of etch pits were identified in the two [111] and two [211] etched samples. Four of these etch pit types had asymmetric pyramidal apexes which were mis-oriented from the normal toward different edges (Fig. 3.16a-d). One type of observed pit had a rounded shape (Fig. 3.16e) and the last type of pit observed appeared to look like several concentric pyramids (Fig. 3.16f).

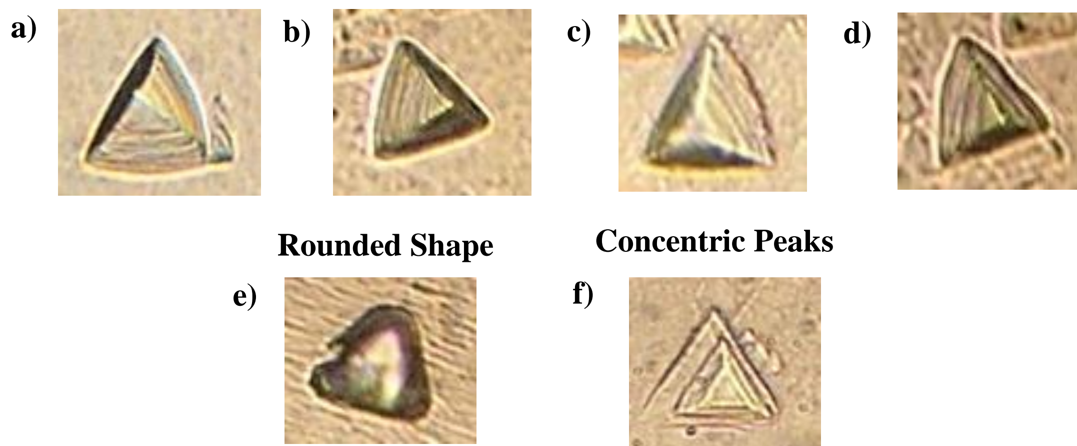

Figure 3.16: Six types of etch pits observed through the Everson etch method

The pits labeled as a), b), c), d) and e) appeared in approximately equal number (~60%) of instances on both [111] and [211] grown crystals. On the other hand, the rounded pit labelled e) was observed only in two instances on the [211] oriented crystals, and none on the [111] crystals.

The etch pit densities (EPD) for four samples were counted by analyzing two locations on each sample, analogous to the procedure used for the Nakagawa etch. The resulting pit densities are in the 10^4 – 10^7 cm^{-2} range (Table 3.5) and are significantly higher than those obtained from the Nakagawa etch (Table 3.4).

Table 3.5: Everson etch pit density count results

Sample	*Orientation*	*Counting Area [mm²]*	*Counted Pits Area 1*	*Counted Pits Area 2*	*Pit Density [cm⁻²]*
B	[111]	6.28×10^{-4}	34	44	6.21×10^{6}
V	[111]	6.28×10^{-4}	89	63	1.21×10^{7}
E	[211]	6.28×10^{-4}	24	21	3.58×10^{6}
M	[211]	6.28×10^{-4}	1	0	7.69×10^{4}

3.4 Discussion

3.4.1 X-ray Diffraction Results Interpretation

3.4.1.1 X-ray Diffraction

An X-ray diffraction study was conducted for 29 [111] and [211] oriented samples. The goal of the study was to establish the quality of the samples by looking at the spread in the Zn concentration and FWHM ranges and to examine the shape of the XRD peaks and any variation which exists between [111] and [211] oriented samples. The variation in Zn between the 29 samples was calculated using Bragg's law to find the lattice constant and Vegard's law to interpolate the percent concentration of Zn. The Zinc distribution for both [111] and [211] samples was found to vary between 2.8% and 7.9% with an average Zn concentration of 4.3% (Fig 3.3a). For the [111] samples, the Zn concentration varied between 3.65% and 7.90% with an average of 5.2% (Fig 3.3b). In the [211] samples the Zn concentration was found to vary between 2.8% and 4.7% with an average of 4.0% (Fig 3.3c). The [211] samples were found to be within the intended 4% growth Zn concentration. The variation of the Zn within the matrix can also be used as an indicator of crystal quality. Areas with a steep Zn concentration gradient have lattice mismatch with neighbouring sites of a different Zn concentration. This introduces strain in the lattice, which is relieved by dislocations resulting in a non-radiative recombination of carriers and results in a poor quality material [4].

Plotting the XRD peaks for the [111] (Fig 3.4) and [211] (Fig 3.5), samples measured on the 422 reflection, samples showed a visible variation in the peak shapes. The [111] samples showed a tendency to split as seen in Samples U and W (Fig 3.4a and Fig 3.4b). A.K. Garg et al (2004) [30], showed that peak splitting in CZT has been previously attributed to areas with high dislocation density, mosaicity or macrograins which form as a result of low critical resolved shear stress. One reason for the development of shear stress is due to the retrograde solubility of CZT. Retrograde solubility, also known as inverse solubility, is exhibited by materials which become less soluble with higher temperature. As the CZT boule cools, Te becomes more soluble and this leads to the formation of thermal gradients between areas of liquid and solid which are at different temperatures [30]. The uniformity of the cooling is also influenced by the ampoule material. The samples in this experiment were grown in a graphite ampoule. Ingots grown in

graphite ampoules have better heat dissipation due to the higher thermal conductivity of graphite, when compared to other standard ampoule materials such as quartz. Better heat dissipation results in smaller temperature gradients and less induced thermal stresses in the ingot [31].

Stress is a significant contributor to the formation of dislocations as strain is relieved in the matrix by forming dislocations. Unlike the peak splitting observed in [111] oriented samples, the [211] samples showed a single peak (Fig. 3.5a), sometimes accompanied by a shoulder (Fig 3.5b), presumably due to regions in the sample with different Zn concentrations. One reason for observing samples with XRD split peaks, single peaks, or peaks with shoulders is that samples came from different parts of the parent boule. L. Xiaohua et al (2000) [31] showed that samples taken from the middle of the parent boule showed less peak splitting when studied with XRD, than samples which were extracted from the periphery of the boule. Additionally, the samples which were studied have compositional variations which also contribute to a variation of the XRD signal.

The FWHM for [111] and [211] samples was obtained (Fig 3.6) and was found to range from 20.17 arc seconds to 160.06 arc seconds with an average of 72.95 arc seconds. The average FWHM values for the samples examined on the [111] (Fig 3.6a) and [422] (Fig 3.6b) reflections were 75.42 arc seconds and 72.28 arc seconds, respectively. The FWHMs of the [111] and [211] samples were found to be higher than those published for other commercial grade material such as work done by A.K. Garg et al (2004) [30], which had FWHM values of 20-60 arc seconds for defect prone regions and an average of <30 arc seconds for other areas. Possible reasons for this deviation from the literature include: (1) variation in the Zn concentration, which results in strain and dislocations, (2) differing sample origin locations from the parent boule, which lead to peak splitting caused by polycrystallinity and (3) different temperature solidification profiles which can increase the shear stress in the material and lead to the formation of dislocations.

3.4.1.2 Reciprocal Space Mapping (RSM)

Reciprocal Space Mapping (RSM) shows a 2D section through reciprocal space which resembles a topographical map. The rings of intensity are a projection of the intensity of the diffraction onto a 2D plane. The amount and pattern of the broadening can be used to understand the type of

defects present in the material. Vertical broadening in the reciprocal space peak is associated with compositional fluctuations. The vertical broadening is associated with the length of the reciprocal lattice vector. Horizontal peak broadening is observed with areas of high dislocation density characterized by bending of the lattice planes in the crystal, attributed to lateral strain and compositional variations in the sample. The horizontal broadening is associated with the orientation of the reciprocal lattice vector [14].

A RSM was generated for one [111] (Sample T, Fig 3.7) and one [211] (Sample M, Fig. 3.8) sample which were selected based on their FWHM. Sample T had a FWHM of 116.25 arc seconds, which was on the high range of the FWHM values calculated. On the other hand, Sample M was chosen due to its low FWHM of 37.68 arc seconds. Sample T had a high FWHM and was found to have a more horizontally (0.05 degrees) and vertically stretched out peak (0.831 degrees). The peak broadening was mainly prevalent in the horizontal direction which indicates a high dislocation density [14]. On the other hand, the peak seen with Sample M is mainly vertically broadened (0.24 degrees), which could indicate strain [14]. However, less broadening was observed in the horizontal direction (0.04 degrees), indicating a lower density of dislocations. This finding is in line with the low FWHM value observed, as a narrow peak is an indicator of crystals with low point defects and dislocations [14].

3.4.2 Transmission Electron Microscopy Interpretation

The Kikuchi map of the CZT sample was used to create a “road map” to the crystal at a local area equal to approximately the field of view. The Kikuchi map showed the presence of one major and two minor zone axis. The Kikuchi map can be indexed which allows for orienting the sample along a desired crystal orientation. In this case, this was not possible because none of the images were obtained directly at a zone axis which allowed for indexing the Kikuchi lines.

The calculated lattice constant taken at four points in the diffraction pattern (Table 3.3) showed an average value of 0.82 nm. This lattice constant was found to be higher than the accepted value of 0.644 nm observed in 4% Zn CZT samples. This deviation could be the result of sources of error with this type of measurement including not being able to exactly tell where the center of each spot is when the software is used to draw the lines shown in Fig. 3.10. The distance between the spots is very sensitive to the measurement and can introduce a large deviation. In

addition, the resolution of the measurement is affected by the size of the diffraction spot. The diffraction spot correlates with electron beam profiles like flatness, where a more planar beam results in a smaller spot which can be measured more accurately. Lastly, the largest contribution to the error in the lattice constant comes from the defocus of the diffraction plane which occurred due to the rotation of the specimen. The images of the specimen were taken at different locations during the tilt, instead of using the eucentric point. The eucentric point is the location in the objective lens where the sample can be tilted around its axis and the image remains centered across the projection screen of the TEM.

Four different points on the sample were used to measure four different lattice constants in the material (Table 3.3). This showed that a variation of lattice parameter over small areas was present presumably due to strain in the material. The CBED imaging allowed for a qualitative observation of the strain in the sample. Fig 3.12 showed that precipitates, most likely caused by Te droplets left over from the solidification process [11], cause bending in the atomic planes and splitting of the HOLZ lines. Norouzpor et al (2016) [32] showed that the splitting of HOLZ lines is indicative of very highly stressed regions in the sample. Fig 3.12b showed the additional strain impact of re-deposited material, visible in black, on the sample. This strain is not indicative of the true strained state of the crystal as it is induced and/or amplified by the presence of the re-deposited layer due to local lattice mismatch. This attests to the importance of properly decontaminating a sample by use of an ion milling machine and ozone cleaning prior to imaging.

Lastly, a two beam phase contrast imaging condition allowed for studying the atomic lattice of the sample. The shaded regions in Fig. 3.13 represent areas with fewer electrons and are thought to be coming from a change in the specimen's thickness and/or strain. A dislocation was noted in the zones labelled as A and D (Fig. 3.13a). Dislocations occurs when shear stress in the material causes defect line movement perpendicular to the direction of stress in the atom displacement and is typically visible on the surface of the material [29]. Areas B and C (Fig. 3.13b) showed the presence of an edge dislocation which is marked by the addition of an extra atomic plane. A edge dislocation can also occur in areas in the material where atoms are not properly arranged, thus introducing localized regions of tension or compression. Therefore, the energy in the material is increased and can promote the movement of dislocations. Dislocations are found to

slip in directions which require the least amount of energy expenditure. This direction is along the most close-packed crystal planes, which are the (111) planes for FCC materials [29].

3.4.3 Wet Chemical Etching Discussion

3.4.3.1 Average Etch Pit Density

The averages of the etch pit density counts from the Nakagawa and Everson etched samples were compared with a few studies from the literature. Previous work showed Nakagawa EDPs to range from 1.12 x 10^4 cm^2 [33] to 1.5 x 10^4 cm^2 [34] and the Everson etch pit density counts to range from 0.5 x 10^4 [35] to 5.0 x 10^4 [36]. The experimental results for the Nakagawa and Everson etch are shown to have a discrepancy with the values observed in the literature. The literature [33, 34] showed a much higher value than the average experimental value of 88 to 199 cm^2 observed with the Nakagawa etch. Additionally, the Everson etch average experimental values of 7.69 x 10^4 to 1.21 x 10^7 cm^2 appear to be larger than the values in previous studies [35, 36]. This discrepancy has several possible origins including: (1) operator discrimination of an etch pit candidate, (2) method of EPD counting (manual or software based), (3) possible cut misalignment from the desired crystallographic orientation and the location of each sample from the parent boule and (4) samples have a higher density of dislocations [30].

Although the EPD counting is a fast way to get a relative idea of the surface defect density, one of the principle drawbacks of this method is the subjectivity and reliance on the operator of what is to be interpreted as an etch pit. Some of the pits, which showed up with the Nakagawa and Everson etches, had a very crystallographic and triangular shape. However, there were many other pits, which had slightly rounded edges and could be interpreted as a pit based on the operator’s judgement. Due to the etchant not being isotropic, meaning it preferentially etches in certain crystallographic directions, previously existing dust particles, scratches and dents can be brought out by the etch making them to appear like a water droplet on the surface. Depending on the geometry, it is up to the individual counting to accept or reject certain pits based on their shape and surrounding morphology. In addition, the EPD count obtained in [36] was analyzed by a software program (Image-Pro Plus v7), which is semi-automated and would have a different discriminating algorithm and acceptance criteria than a human counting the pits.

Burgess at al (2015) [36] also presented findings indicating that the number of etch pits' changes depending on the mis-cut of the sample from the intended crystallographic orientation (ie. [111] or [211]). In this experiment the samples were grown by Vertical Gradient Freeze (VGF) (discussed in Section 2.2.1), which is a process requiring the extraction of material along certain growth directions. It is possible that a slight mis-cut is present in the sample(s), and this could have an impact on the pits' number. Lastly, the samples could have been from a part of the parent boule near the crucible wall. This area is subjected to a much higher shear stress and thermal gradient in both the growth and solidification process that would result in a higher density of dislocations, which in turn will increase the etch pit density count [30].

3.4.3.2 Types of Etch Pits Present in Material

The dislocation density is a representation of the crystal quality of the material and etch pits are known to form where dislocations intersect the surface. The main dislocation formation mechanisms in CZT are: (1) due to the presence of Te precipitates in the matrix, (2) due to thermal stresses during cooling and (3) any mechanical damage or stress to the material during or after the manufacturing stages [4]. The formation of dislocations in CZT is discussed in detail in Section 2.3.1. In this experiment, ten samples from both the (111) and (211) orientations, were etched using Nakagawa and Everson etching solutions. The Nakagawa etch showed pits which had the same shape but came in two distinct sizes (Fig. 3.14). A hypothesis for this size variance is that each pit is representative of two different sizes of Te precipitates in the matrix. On the other hand, the Everson etching method showed the presence of five different types of etch pits (Fig. 3.15). The observed difference in shape between each of the five pits can be explained by the plastic deformation mechanism previously studied in Zn blende structures [37, 38].

According to the plastic deformation mechanism seen in Zn blende structures, the local material deformation due to dislocations results from slip along the {111} faces with lattice propagation directions in <110>. As stress is released into the matrix, dislocations form due to tangential and tetrahedral glide systems which represent Burgers vectors in a surface-parallel direction and Burgers vectors along <110> directions into the material, respectively. Figure 3.17 shows a cross section view of (111) oriented CZT material and the dislocation orientations formed by the tangential and tetrahedral glide systems.

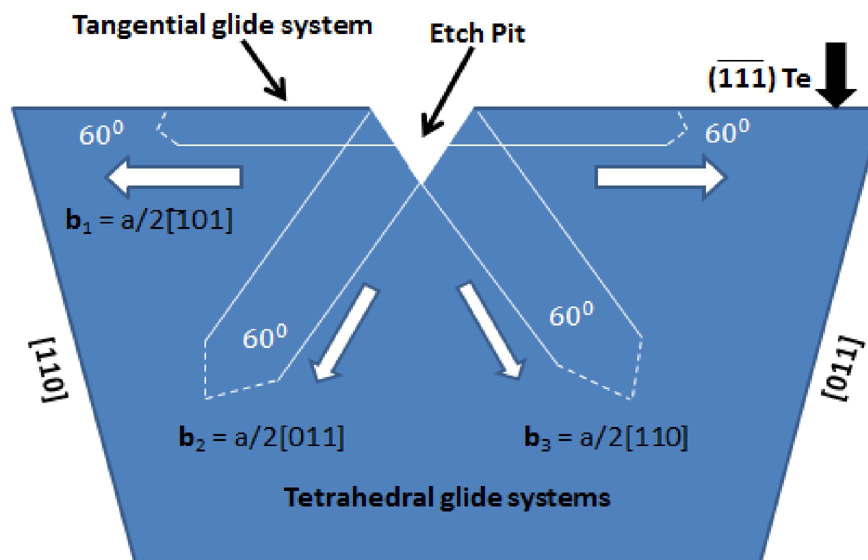

Figure 3.17: Model for spreading of Cd and Te dislocations throughout the material via tangential and tetrahedral glide systems [38]

The tangential glide system, $\mathbf{b_1}$, usually forms in six directions along the surface, radiating from the etch pit site at an equidistant rotational spacing of 60° from one another. The tetrahedral glide system, $\mathbf{b_2}$ and $\mathbf{b_3}$, forms a three sided tetrahedral prism which extends into the material. Each tetrahedron side is made up of a Burgers vector positioned 60° from the surface and having a glide orientation inclined down the <110> direction and a dihedral angle of two conjoined glide {111} planes at 70.5^{o} [37]. Each glide system represents the formation of different types of dislocations. The tangential slip system mainly forms dislocations half loops on the surface and is usually activated by surface damage. On the other hand, the tetrahedral glide systems is associated with deeply penetrating screw dislocations which sometimes slip around a local deformation center such as a Te precipitate. The threading distances of the dislocations in this experiment was not measured; however, Cui at al (2011) [35] showed that threading distances into the material for all of the directions have been seen to extend up to 18 μm.

No tangential glide systems, characterized by etch pits radiating in a rosette shape anywhere on the surface, were observed in this experiment. However, five different types of pyramidal shaped etch pits, associated with tetrahedral glide, were seen in the material. Tetrahedral glide systems represent screw dislocation half-loops, characterized by dislocations which have segments going both on the surface and into the material, which propagate deep into the CZT matrix. They can

be distinguished as deeper pyramid pits with clearer etching steps [37]. This type of pit made up about 85% of the Everson pits observed in this experiment (Fig. 3.18).

Figure 3.18: Examples of etch pits representing tetrahedral slide systems observed during the experiment in both (111) and (211) oriented CZT samples

Previous Everson etch pit characterization work by Y. Xu et al (2012) [37] showed that different etch pits can be distinguished by the slant of their apex, and that the direction of the apex slant can also be correlated to a dislocation threading along a particular crystal plane direction [37]. Y. Xu at al (2012) [37] additionally showed that the highest density of dislocations orientations in CZT are along the <211>, <131>, <111>, <151>, <031> and <110>, with <211>, <111>, <151> and <031> directions. The dislocation threading direction associated with an etch pit can be determined with the help of a pole figure (Fig. 3.19). A pole figure is a stereographic projection of the [111] plane. The ratio between tetrahedral vertices and the apex of each etch pit can be measured and then that can be matched to a location on the pole figure with the same ratio. The experimentally measured apex location matched onto the pole figure determines the dislocation threading direction. Figure 3.19 shows four etch pits from the experiment which were matched to the (111) pole figure reinterpreted from [35].

Figure 3.19: Dislocation direction assignment of four etch pits in [111] oriented samples (left) and [111] pole figure used for assignment (right). Figure adapted from Ref. [35]

Additionally, triangular shaped etch pit clusters revealed by the Everson method (Fig. 3.20) have been shown to represent tetrahedral glide prisms forming due to the intersection of multiple tetrahedral glide systems in areas of high material strain.

Figure 3.20: Three examples of a triangular cluster of etch pits found in the material studied in this thesis, which has been shown to form on top of Te precipitates, which are below the surface of the material [37]

Previous work showed that these areas of high material strain coincided with a Te precipitate embedded in the sub-surface matrix. The Te precipitates distort the matrix, inducing stress, which is relieved by the formation of dislocations. Therefore a link between the number of etch pits and the density of Te precipitates has been established. Although the observed etch pit triangle clusters were not excavated in order to confirm the presence of Te precipitates, previous work using IR transmission microscopy images taken at etch pit sites, have shown that these clusters correspond with Te precipitates [37].

Chapter 4
Electronic Characterization

4.1 Theory

4.1.1 Photoluminescence

Photoluminescence (PL) in solids is the phenomenon in which the electronic states of solids are excited by a light source of a particular energy and the excitation energy is released back in the form of light [39]. The excitation source, typically a laser, is chosen to have a higher excitation energy than the band gap of the material. The laser is directed at the surface of the sample where the incident beam is partially reflected, absorbed or transmitted by the material. When the incident beam is absorbed, the excitation photons stimulate electrons from the valance band to the conduction band or to an energy state within the band gap, E_g [40]. An oppositely charged electron-hole pair forms and is weakly bound by an electrostatic Coulomb force interaction. This is known as an exciton. When excitons recombine, photons are emitted from the surface of the sample and the resulting emission spectrum is recorded as photoluminescence [41].

4.1.1.1 Bound Excitons and Variation in Spectral Emission Intensity

Since a direct conduction band-to-valence band recombination is not frequently observed, emissions have energies smaller than the band gap of the parent material. This is due to the presence of vacant lattice sites, impurities and defects in the material which act as traps for charge carriers. Defects and impurities perturb the band structure locally by acting as discontinuities in the lattice. These can be characterized by a disturbance in a discrete energy level which lies in the band gap. Depending on the type of defect or impurity, the state will act as a donor or acceptor of excess electrons in the crystal due to Coulomb binding. Variation in the Coulomb binding energies exists as a result of the different effective masses of holes and electrons [41].

PL measurements, especially bound exciton luminescence, are used to check for residual impurities in high purity compound semiconductors because the impurities show sharp emission lines at known energy positions [42]. When an exciton encounters a defect in the material, it can decrease the energy of the exciton and bind it to the defect. When excitons become trapped, they

are referred to as bound excitons, which have lower emission spectra than free excitons. The types of bound excitons observed in CZT are summarized in Table 4.1.

Table 4.1: Bound exciton types, composition and PL emission energies present in CZT [43, 44]

Symbol	*Type*	*Composition*	*PL Emission Energies (eV)*
$(D^{+}$, X)	Exciton bound to ionized donor	Donor ion, an electron and a hole	1.590-1.592
$(D^{0}$, X)	Exciton bound to neutral donor	Donor ion, two electrons and a hole	1.592 – 1.595
$(A^{-}$, X)	Exciton bound to ionized acceptor	Acceptor ion, an electron and a hole	Not observed in CZT
$(A^{0}$, X)	Exciton bound to neutral acceptor	Acceptor ion, an electron and two holes	1.5890-1.588

Additionally, the binding energies required to trap a free exciton also depend on the zinc molar concentration. They have a linear relationship described by Vegard's law and vary between 10 meV for CdTe and 13 meV for ZnTe. The emission lines due to bound excitons tend to have a narrower line width than those due to free excitons as a result of increased localization.

Donors and acceptors are also characterized by their energy within the bandgap. A diagram of several recombination processes, which can be detected in 4% CZT, is shown in Fig 4.1.

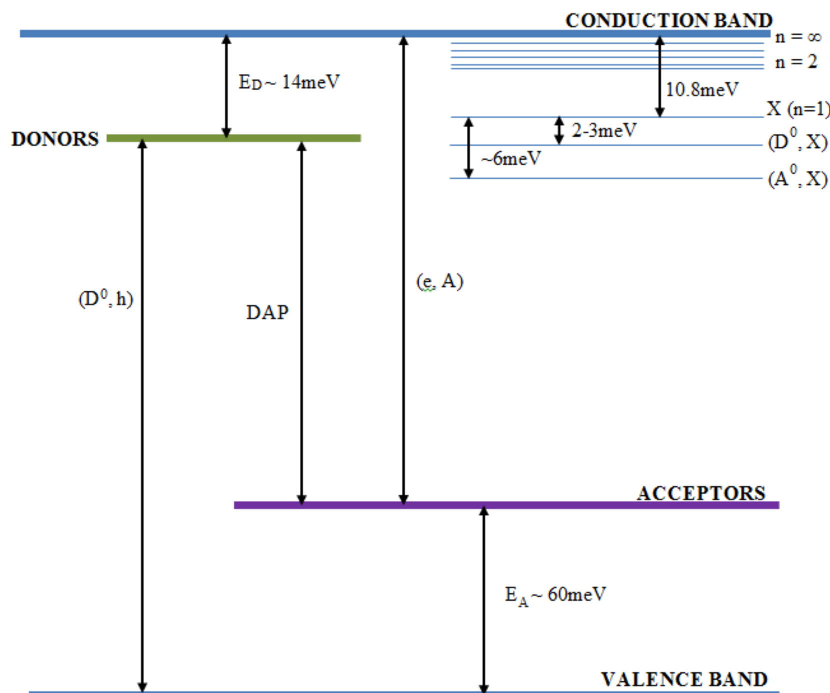

Figure 4.1: Energy level diagram for various radiative transitions in $Cd_{1-x}Zn_xTe$ (x = 4%), reinterpreted from [45]

Sometimes, if the binding energy is too great, the electron-hole pair will not have a high enough energy to be emitted from the crystal as a photon, so it will be released as a phonon.

4.1.1.2 Excitation Intensity and Temperature Dependence of Photoluminescence

Variation in the PL intensity as a function of excitation intensity and temperature can be used to further characterize electronic states and bands. The excitation intensity controls the density of photo-excited electrons and holes, which govern the behaviour of those carriers [41]. When the carrier density is low, the spectrum is dominated by discrete defect and impurity sites. By varying the laser power, using neutral density filters of increasing strength, the plot of log(PL intensity) vs. log(laser power) can be analyzed to determine the nature of the PL emission.

Temperature also affects the PL emission. The PL signal is largely dependent on the temperature due to the effects of thermal activation. As the sample temperature increases, excitons dissociate. [41]. Increases in temperature result in a reduction in radiative recombination of carriers due to the dissociation of excitons and increasing rates of competing nonradiative recombination processes. When the temperatures are low, the carriers get trapped at a localized state. When

recombination occurs, the energy is emitted as PL and the wavelength of the emission can be used to determine the energy of the defect or impurity level.

4.2.1 Hall Effect in Semiconductors

The Hall Effect experiment is a powerful method for measuring the electrical properties of a semiconductor. This measurement allows for information gathering regarding carrier concentration, mobility and the sign of the carriers. The carrier concentration and mobility can be used to calculate the conductivity of a semiconductor material. The Hall Effect is observed when a semiconducting material is placed in a z-pointing magnetic field with applied current along the sample's surface (y-direction). When a magnetic field is applied perpendicular to the direction of the flow of carriers, a potential difference appears in a direction which is normal to both the current flow and the magnetic field (x-direction) [46]. Figure 4.2 shows the basic schematic of the Hall Effect.

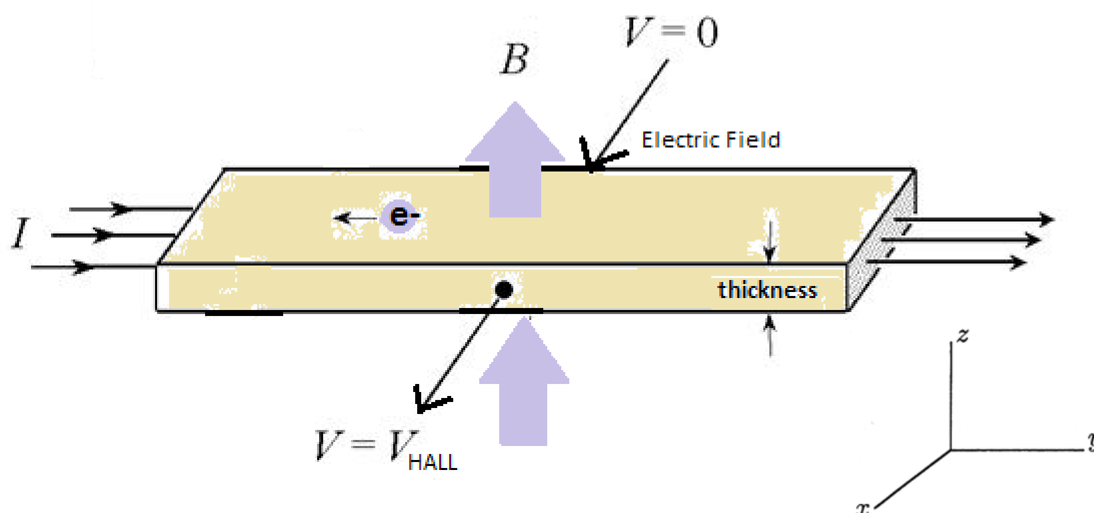

Figure 4.2: Schematic of the Hall Effect observed in semiconductors placed in a magnetic field

The electrical field is applied by placing four contacts on the sample's surface, one at each corner and connecting two of them to a current source. The Lorentz Force ($qv \times B$) exerted due to the magnetic field acts on each electron in a direction which is normal to both the direction of the flow of carriers and to the magnetic field. Since no current can flow in the x-direction, an

electric field, known as the Hall field, balancing the Lorenz force is created and this can be expressed using Equation 4.1.

$$\varepsilon_T = -(v_{dn} \times B) = -\frac{1}{qn}(B \times J) \qquad \textbf{4.1}$$

In this equation, the transverse Lorenz force is ε_T, the velocity of the carriers is v_{dn}, the magnetic field is B, q is the charge, n is the number of carriers and J is the current density. The potential voltage, known as the Hall Voltage, can be measured at the sides of the sample. Once the transverse electric field is known, the Hall coefficient can be determined. The Hall coefficient is a measure of the density of carriers in a semiconductor. The Hall coefficient, R_H, can be found using Equation 4.2, where J_n is the current density.

$$R_H = \frac{|\varepsilon_T|}{|J_n||B|} = \frac{-1}{qn} \qquad \textbf{4.2}$$

When the Hall coefficient is also combined with the conductivity (or resistivity) measurement, the majority carrier density and mobility can be calculated. Additionally, whether the material is p- or n-type can be determined, by the positive or negative sign of the Hall voltage, V_{Hall} [46].

4.2 Experimental Method

4.2.1 Photoluminescence

4.2.1.1 Room Temperature Experiment Set-up

The room temperature PL experimental set up used was comprised of a 532 nm green laser (Spectra-Physics Model 7950-L104), height adjustable stage, two optical lenses, a 590 nm long pass filter and a fibre optic cable attachment as seen in Fig. 4.3.

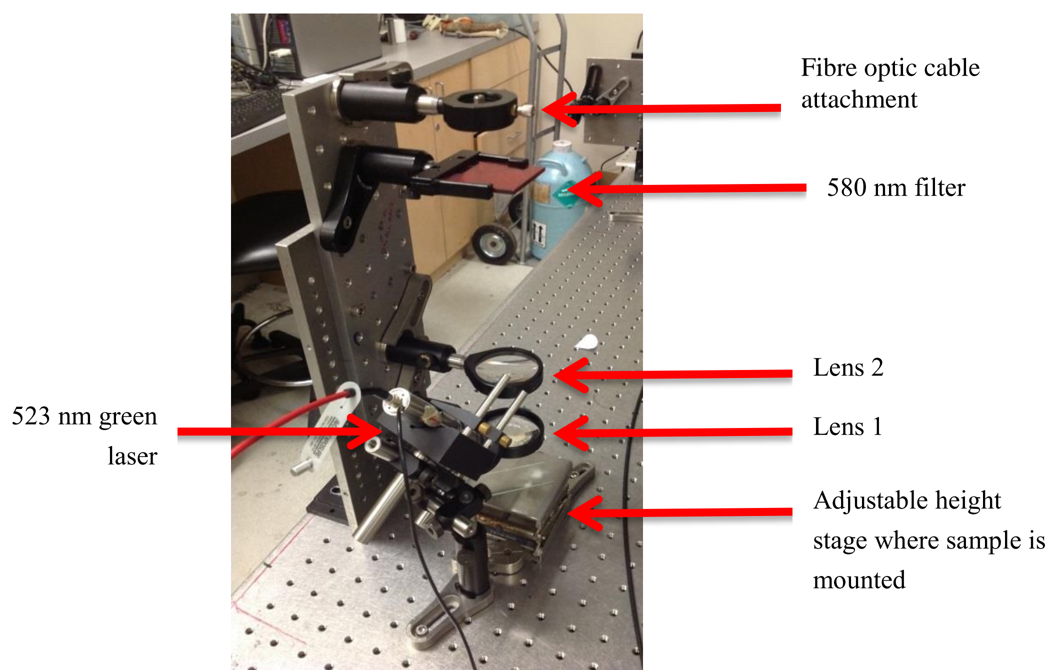

Figure 4.3: Photoluminescence set up used for room temperature experiments

The sample is excited using a pulsed laser (20 ns long pulses), consisting of a diode-pumped frequency doubled YLF laser with an average power of 5mW. The first lens (Lens 1) has a 4.5 cm focal length which is coincident with the height of the sample stage. Lens 1 collimates the signal into Lens 2, which is positioned ~5.0 cm above it. The second lens has a focal length of 19.5 cm and is placed at this exact distance from the fibre optic cable inlet. Before the signal reaches the fibre optic cable, a 590 nm filter is used to attenuate the laser signal. The intensity of the laser signal must be decreased, as it results in over excitement and saturation of the InGaAs detector array (Roper Scientific Model 7410-0003). The InGaAs detector array used has 300mm focal length, a 600 g/mm or a 1200 g/mm setting and a near infrared wavelength spectrum.

4.2.1.2 Low Temperature Experimental Set-up

The PL laboratory experimental set up was reconfigured for use at cryogenic temperatures. The samples were placed onto a copper holder and temporarily glued on using an Apiezon cryo-grease product. The holder was screwed into the base of the Advanced Research Systems Inc. cryo-column where the samples were cooled to 9 K using a Helium-based refrigerator. The low temperature PL set up is shown in Fig. 4.4.

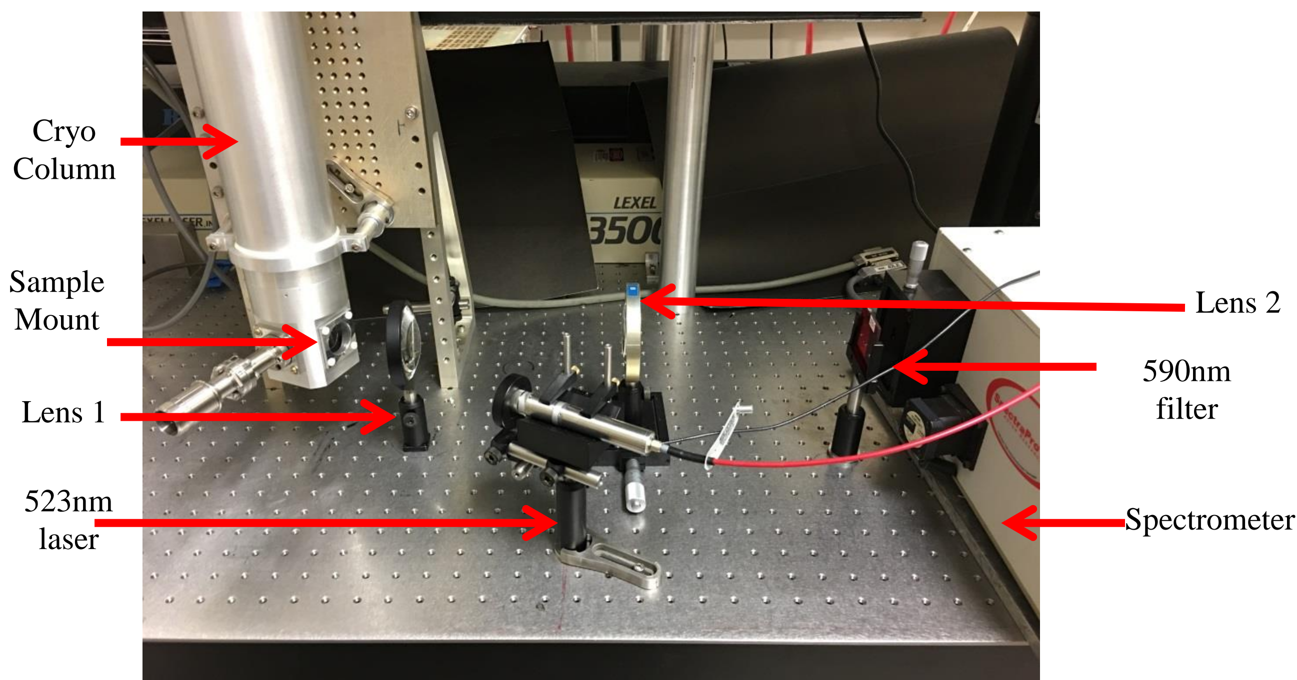

Figure 4.4: Low temperature photoluminescence experimental set up

The cryogenic column is kept at a high vacuum by a two-stage pumping system. A scroll pump (Franklin Electric Model 1201006408) is used to evacuate the majority of the air, and then a high vacuum (~10^{-8} Torr) is achieved by using a turbo molecular pump (Seiko+Seki Model STP-30). A high vacuum is needed to remove any residual gas species as any water vapour or air will freeze in the column. The experimental set up allowed for mounting four samples at a time. A 532 nm green laser was used to excite each CZT sample with a 5 second integration time. The PL emission was collected using the same two lens and 590 nm filter configuration used with the room temperature experiment. The spectrometer was operated in the high resolution 600 g/mm grating mode.

The first experiment was used to study the effect on the PL emission of varying the laser power and recording the PL intensity. Six neutral density filters were used in succession to reduce the average power of the green laser from 5 mW to 0.75 mW, and a spectrum was obtained at each laser power. The neutral density filters used allowed the transmission of 97%, 81%, 63%, 60%, 25% and 15% of the laser power for each reading. The second experiment studied the behaviour of the PL spectra as the temperature was raised from 9K to 300K. A PL spectrum was obtained at 11 temperature points. The PL intensity as a function of temperature plots were used to

determine the activation energy of each peak, which is a measure of the energy required to delocalize a carrier particle from a trap.

4.2.2 Hall Effect in Semiconductors

The Hall coefficient for a semiconductor was measured by fastening the sample into a van der Pauw device. Three van der Pauw devices were manufactured using two [211] oriented samples and one [111] oriented sample. The van der Pauw devices were made by mounting each sample on a glass slide using double sided tape. An electric contact port, used to deliver current to the sample, was then bonded onto the slide using 50/50 mix of JB Weld (steel) and JB Weld (hardener) bonding cement. Silver-filled electrical epoxy resin (EPO-TEK-EE129-4) was used to make electrical contacts on the samples, which were also connected to the electrical plug-in. Fig. 4.5 shows the experimental set-up and a sample van der Pauw device.

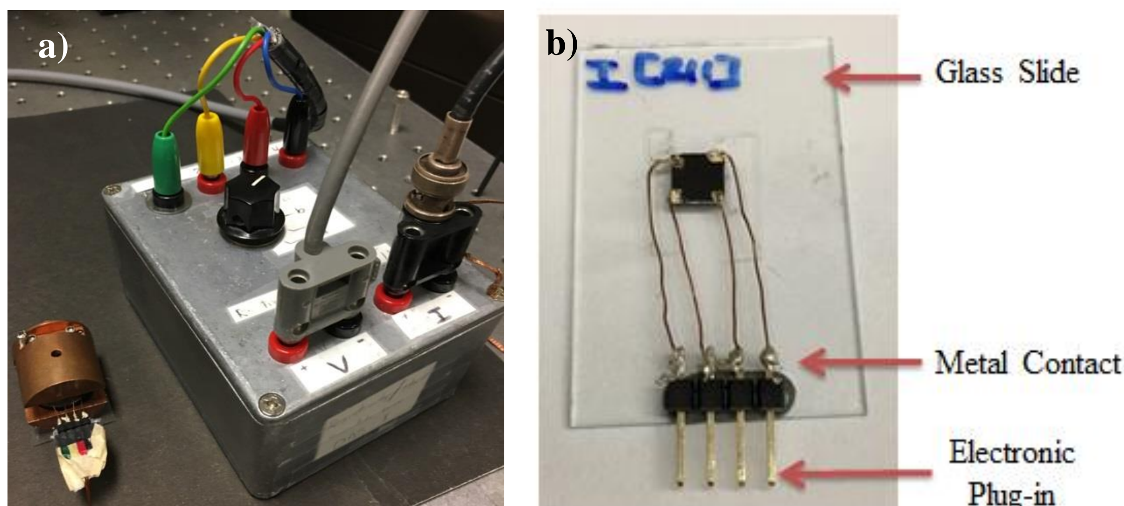

Figure 4.5: (a) van der Pauw I-V control unit and magnet and (b) van der Pauw device showing sample mounted on glass slide with four contacts

The copper wires had to be stripped of any insulation to ensure that there was a good electrical contact between the silver epoxy and the sample. This was done by using a gas torch to burn off the insulation. Any remaining parts of the insulation were stripped away by using a Brillo steel wool pad. The Hall I-V control unit (Fig. 4.5a) was connected to a programmable current source (Keithley 220) and a volt meter (Keithley 197 Microvolt DMM). The samples were placed in a dark box and the lights in the lab were turned off to avoid any photoconductive and photovoltaic

effects. Two additional samples, both in the [111] orientation, were made into van der Pauw devices using thinner copper wire, also stripped of insulation, and an Indium contact paste. These were found to be unsuccessful in producing functional contacts and were not used in the experiment.

4.3 Results

4.3.1 Photoluminescence

Photoluminescence was used to study the optical properties of the CZT samples. Room temperature experiments were used to get information about the band gap of the material, which can be used to calculate the Zn concentration. Low temperature experiments were performed in order to study the band structure of the material and to characterize and identify the type of defects and impurities present in the material.

4.3.1.1 Room Temperature Study

Room temperature PL emissions were collected. Each reading was fitted using an intrinsic direct band gap luminescence model in order to calculate the band gap of the material, E_g [47]. The band gap was used to determine the local Zn concentration and its variation in the samples. CZT is a direct band gap semiconductor, which has a PL spectrum made up of band-to-band transitions, I_{PL}^{b}, and below band gap luminescence intensity, I_{PL}^{e}, which is proportional to the localized density of states. Equation 4.3 models the PL intensity under ideal conditions for direct energy band gap semiconductors with a parabolic band edge [47].

$$I_{PL}^{b}(h\omega) = \begin{cases} A(h\omega)^2(h\omega - E_g)^2 e^{-(h\omega - E_{g)/(k_B T_e)}} \\ h\omega > E_g \\ 0, h\omega < E_g \end{cases} \quad \textbf{4.3}$$

In this expression, I_{PL}^{b}, is the PL intensity from the band-to-band transition, $h\omega$ is the photon energy, E_g is the band gap, T_e is the effective temperature (298 K), k_B is the Boltzmann constant (1.3806 x 10^{-23} $\frac{m^2 kg}{s^2 K}$) and A is a proportionality parameter. This model assumes that no emission is present below the energy gap. However, there is always some residual light emission, which can come from the band tail states induced by disorder, localized defects and bound

excitons [47]. This part of the emission correlates with the localized states within the energy gap. In the case where the below the gap luminescence, I_{PL}^{e}, is proportional to the localized density of states, this can be expressed in Equation 4.4 [47].

$$I_{PL}^{e}(h\omega) = \begin{cases} 0, h\omega > E_g \\ \frac{N_e}{E_0} e^{[\frac{(h\omega - E_g}{E_0}]}, h\omega < E_g \end{cases} \quad \textbf{4.4}$$

In this expression, I_{PL}^{e} is the below-gap luminescence intensity, N_e is the localized density of states and E_0 is the exponential decay fitting parameter. The combination of the two contributing factors to intensity models the full PL spectrum as expressed in Equation 4.5 [47].

$$I_{PL}(h\omega) = I_{PL}^{b}(h\omega) + I_{PL}^{e}(h\omega) \quad \textbf{4.5}$$

There are four fitting parameters in this equation. The collected data from all samples was analyzed according to Equation 4.5 to determine the values of A, E_g, N_e, and E_0. This fit was first tried but was found to contain a discontinuity at the band gap value, E_g. A modification was added to the model to then convolute the two signals (Equation 4.6), instead of adding them as per Equation 4.5.

$$I_{PL}(h\omega) = I_{PL}^{b}(h\omega) * I_{PL}^{e}(h\omega) \quad \textbf{4.6}$$

The convoluted fit was found to better describe the experimentally obtained data and removed the discontinuity at E_g. For CZT, the values of the band gap are directly related to the Zn concentration according to Equation 4.7 [47].

$$E_g\,(eV) = (1.494 \pm 0.005) + (0.606 \pm 0.010)x + (0.139 \pm 0.010)x^2 \quad \textbf{4.7}$$

This equation is valid for band gaps at a temperature of 280 K.

4.3.1.1.1 Zinc Concentration

The Zn concentration for all 29 samples was calculated. A representative PL spectrum of sample B is presented, in Fig. 4.6, where the curve fit by Equation 4.5 is shown and compared with the improved curve fit from Equation 4.6.

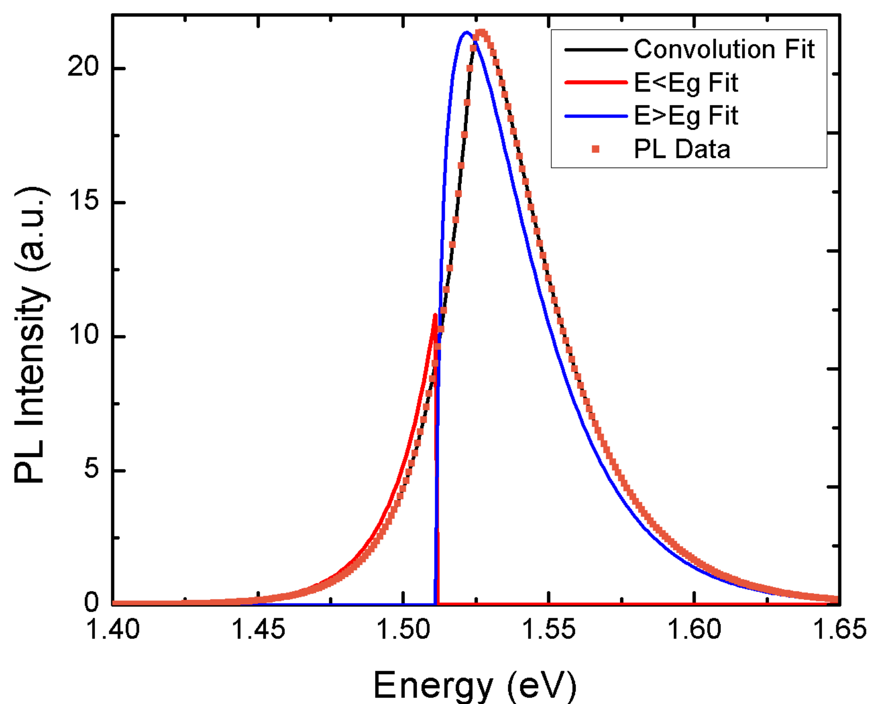

Figure 4.6: Example room temperature fitting analysis for calculating Eg in Sample B (black, Equation 4.6 fit), and comparison to the improvement from Equation 4.5 (red and blue) showing the previous fit compared with the raw data (orange)

The convolution fit (Equation 4.6) was found to be an improvement from the original fitting method (Equation 4.5) due to the removal of the discontinuity at the band gap, E_g. Sample convolution fits are shown for Sample L [211] (Fig. 4.7) and Sample S [111] (Fig. 4.8).

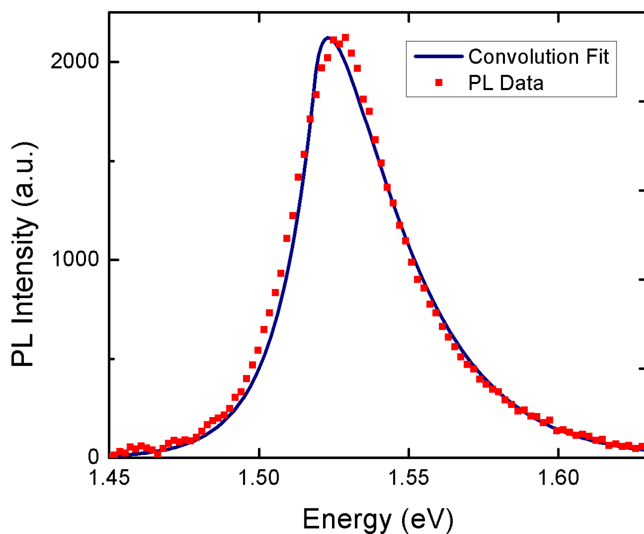

Figure 4.7: Sample L [211] convolution fit

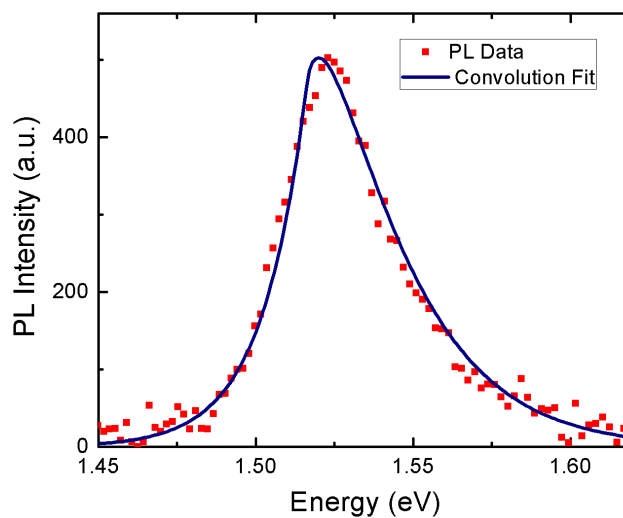

Figure 4.8: Sample S [111] convolution fit

The corresponding values of A, E_g, N_e, and E_0 for all 29 samples are given in Table 4.2.

Table 4.2: Room temperature PL fitting parameters used in band gap calculation

Sample	*A*	E_g	N_e	E_0
A	PL signal too weak for curve fitting			
AA	$2.6 \times 10^3 \pm 32$	1.508 ± 0.002	2.21 ± 0.2	0.016 ± 0.002
B	$1.8 \times 10^3 \pm 107$	1.510 ± 0.002	22.16 ± 0.8	0.016 ± 0.002
BB	$1.5 \times 10^4 \pm 94$	1.511 ± 0.002	16.77 ± 0.6	0.015 ± 0.002
C	$1.5 \times 10^2 \pm 25$	1.501 ± 0.002	0.15 ± 0.3	0.054 ± 0.002
CC	$1.3 \times 10^4 \pm 65$	1.509 ± 0.002	14.17 ± 0.4	0.015 ± 0.002
D	$1.3 \times 10^4 \pm 83$	1.509 ± 0.002	9.41 ± 0.6	0.015 ± 0.002
E	$1.0 \times 10^4 \pm 71$	1.509 ± 0.002	10.91 ± 0.5	0.018 ± 0.002
F	$1.6 \times 10^4 \pm 102$	1.509 ± 0.002	20.25 ± 0.7	0.017 ± 0.002
G	$1.3 \times 10^4 \pm 82$	1.506 ± 0.002	15.08 ± 0.6	0.013 ± 0.002
H	$1.9 \times 10^4 \pm 110$	1.510 ± 0.002	21.77 ± 0.8	0.015 ± 0.002
I	$1.9 \times 10^4 \pm 114$	1.510 ± 0.002	23.09 ± 0.8	0.014 ± 0.002
J	$1.6 \times 10^4 \pm 100$	1.509 ± 0.002	19.04 ± 0.7	0.016 ± 0.002
K	$2.2 \times 10^4 \pm 132$	1.509 ± 0.002	27.41 ± 0.9	0.015 ± 0.002
L	$1.5 \times 10^4 \pm 95$	1.510 ± 0.002	17.47 ± 0.7	0.013 ± 0.002
M	$2.6 \times 10^4 \pm 151$	1.511 ± 0.002	31.58 ± 1.0	0.015± 0.002
N	$1.9 \times 10^4 \pm 117$	1.511 ± 0.002	24.01 ± 0.8	0.015 ± 0.002
O	$4.1 \times 10^3 \pm 36$	1.510 ± 0.002	3.51 ± 0.2	0.016 ± 0.002
P	$4.0 \times 10^3 \pm 33$	1.510 ± 0.002	4.43 ± 0.2	0.015 ± 0.002
Q	$3.0 \times 10^3 \pm 35$	1.508 ± 0.002	2.24 ± 0.2	0.012 ± 0.002
R	$3.8 \times 10^3 \pm 32$	1.508 ± 0.002	3.92 ± 0.2	0.013 ± 0.002
S	$3.6 \times 10^3 \pm 36$	1.508 ± 0.002	3.16 ± 0.2	0.014 ± 0.002
T	$3.5 \times 10^3 \pm 31$	1.509 ± 0.002	4.03 ± 0.2	0.014 ± 0.002
U	$1.8 \times 10^4 \pm 107$	1.507 ± 0.002	20.61 ± 0.8	0.014 ± 0.002
V	$1.2 \times 10^4 \pm 76$	1.508 ± 0.002	12.13 ± 0.5	0.015 ± 0.002
W	$1.3 \times 10^4 \pm 81$	1.509 ± 0.002	13.72 ± 0.6	0.016 ± 0.002

Sample	*A*	E_g	N_e	E_0
X	1.1 x 10^4 ± 68	1.509 ± 0.002	12.36 ± 0.5	0.016 ± 0.002
Y	PL signal too weak for fitting			
Z	1.3 x 10^4 ± 83	1.509 ± 0.002	14.21 ± 0.6	0.015 ± 0.002

The curve fittings, improved through convoluting the signals, for the room temperature PL data. This improved fit produced good results shown by the small errors observed in the fitting parameters A, E_g, N_e, and E_0. The only outliers in the fitting were for Samples A and Y, which had a very weak PL signal which could not be fitted.

A low PL intensity is observed in cases where the sample has surface damage or the presence of defects. The data from Table 4.2 was used to calculate the Zn concentration (%) for all samples (Fig 4.9a) using Equation 4.7. The Zn (%) data is presented for all [111] and [211] samples in Fig. 4.9a, and then each growth orientation is shown separately in (Fig. 4.9b) and [211] (Fig. 4.9c).

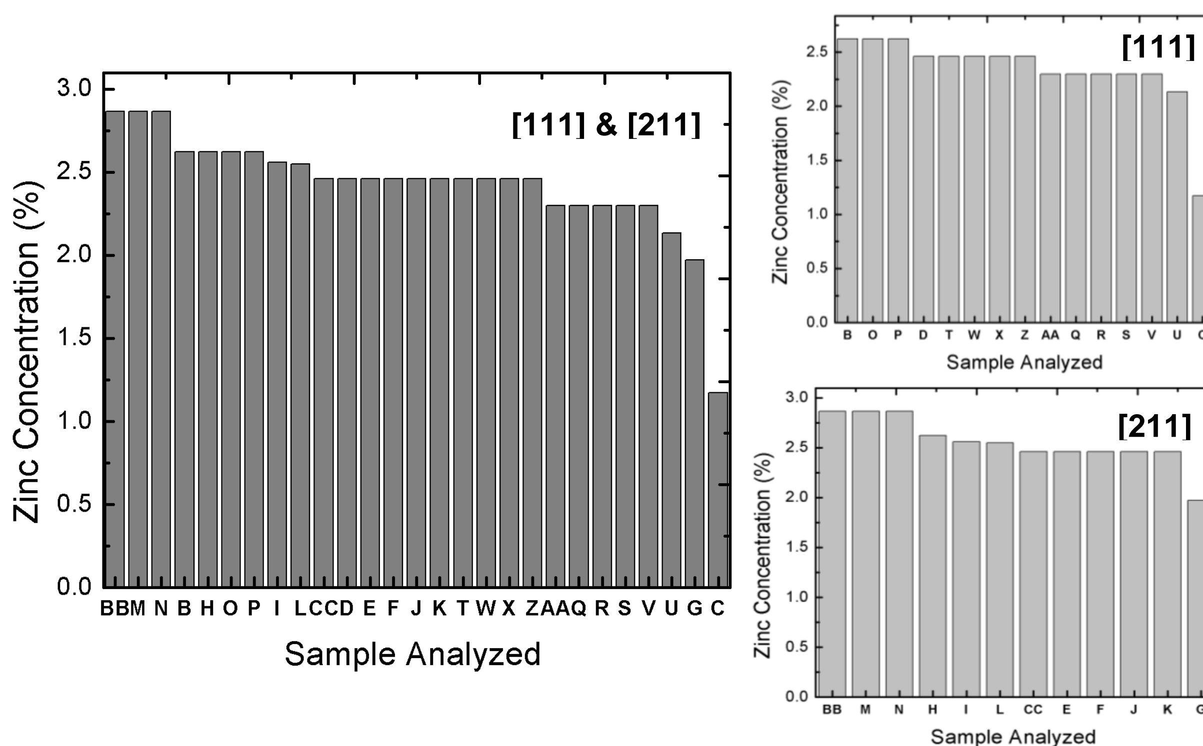

Figure 4.9: Zinc (%, molar) concentration spread for all 29 samples (left) and this same data repeated separating the growth directions [111] (top right) and [211] (bottom right)

The Zn (%, molar) concentration was found to vary from 1.17% - 2.87% in the overall sample population. The Zn concentration range for the two growth directions were 1.17% - 2.62% and 1.97% - 2.87% for the [111] and [211] samples, respectively.

4.3.1.1.2 Photoluminescence Zinc Concentration Mapping

The uniformity of the local Zn concentration was mapped for eight samples. The height adjustable stage in the room temperature PL set up was equipped with a two-dimensional micrometer translation stage. Each sample was examined using nine spots all located 0.3 mm away from one another. The band gap energy of each emission was analyzed using Equation 4.4, Equation 4.5, and the Zn (%, molar) concentration was calculated using Equation 4.7. Contour maps of the Zn distribution for each sample are shown in Fig. 4.10 to Fig. 4.17.

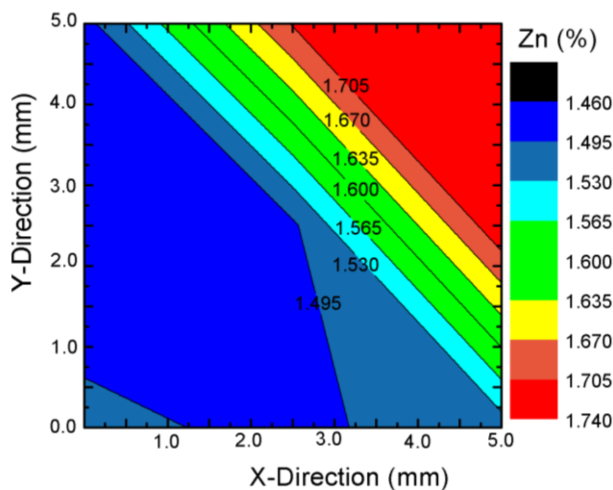

Figure 4.10: Zn (%) distribution contour map of Sample W, [111]

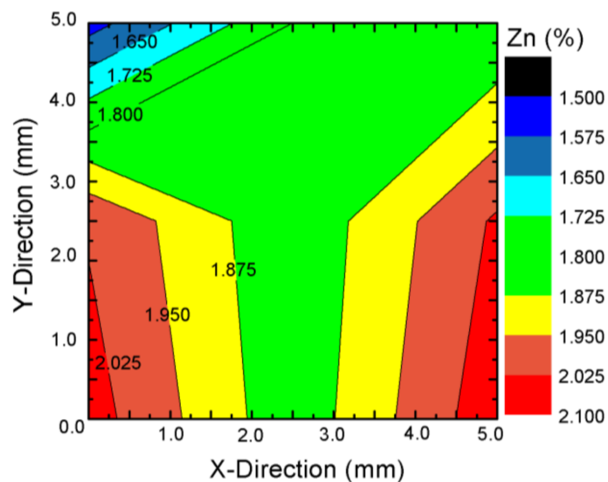

Figure 4.11: Zn (%) distribution contour map of Sample Y, [111]

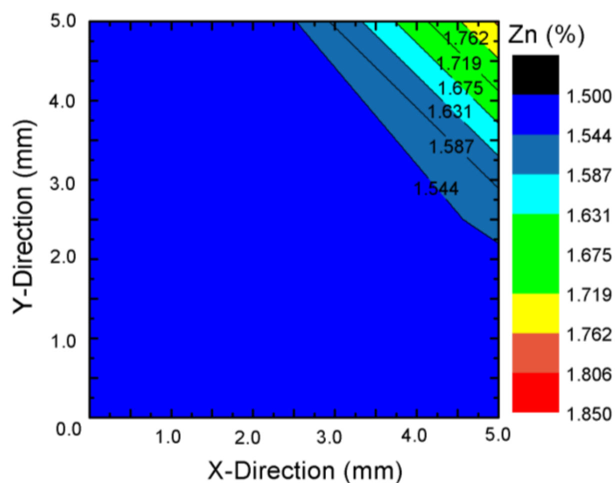

Figure 4.12: Zn (%) distribution contour map of Sample R, [111]

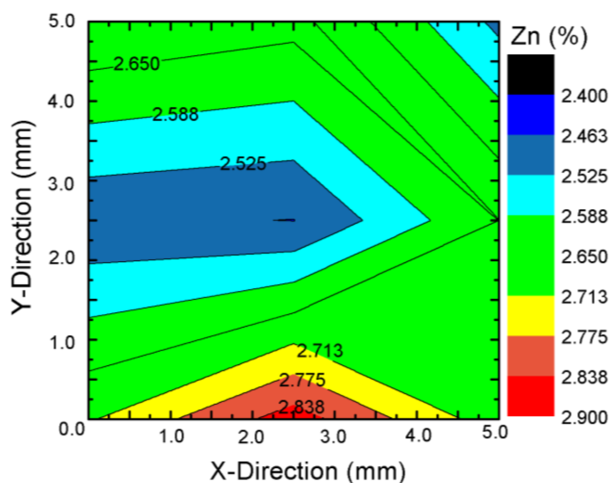

Figure 4.13: Zn (%) distribution contour map of Sample N, [211]

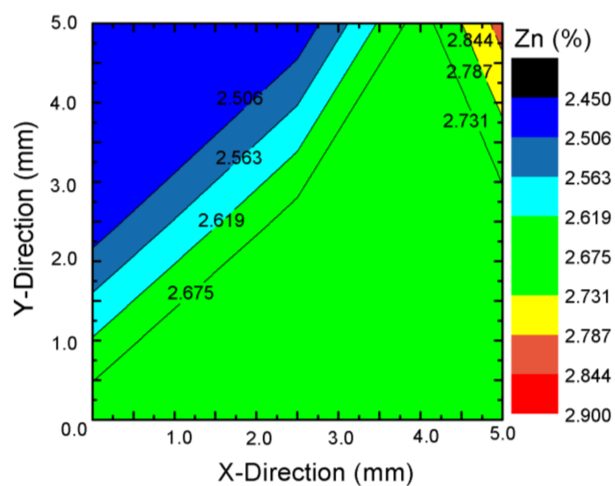

Figure 4.14: Zn (%) distribution contour map of Sample M, [211]

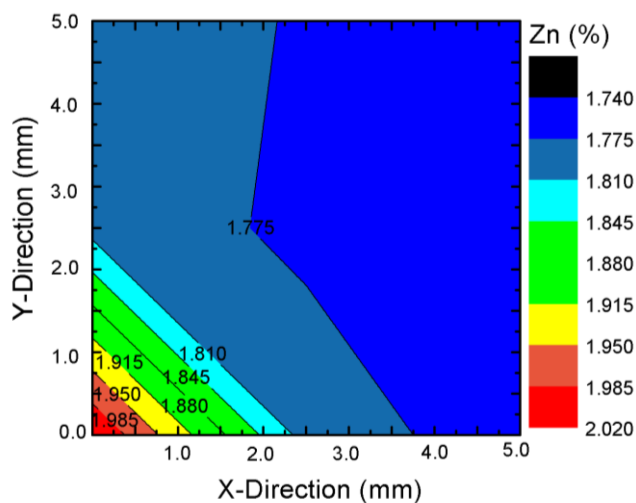

Figure 4.15: Zn (%) distribution contour map of Sample F, [211]

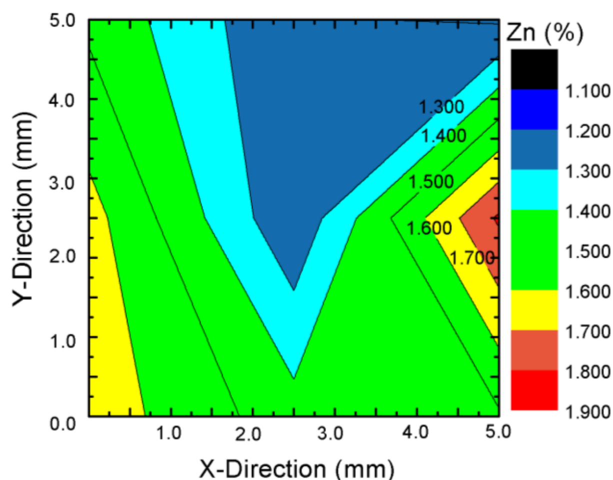

Figure 4.16: Zn (%) distribution contour map of Sample M, [211]

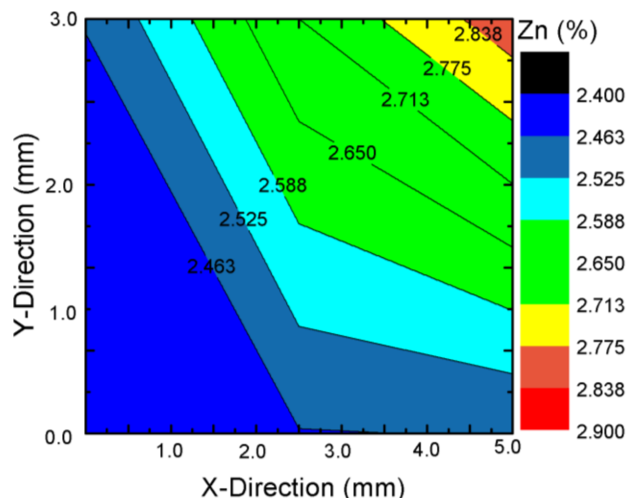

Figure 4.17: Zn (%) distribution contour map of Sample BB, [211]

The results indicate that some of the samples showed a large variation in the zinc concentration and some did not. Although these are bulk single crystals, sometimes micro-polycrystallinity exists in localized areas [4].

4.3.1.2 Low Temperature Study Results

The low temperature PL spectra had six to seven emission peaks at different energies. The peaks were resolved using a multi-peak fitting function in IGOR Pro which allowed for calculating the FWHM. Each spectrum was loaded into the program and then each peak was resolved using a Gaussian or Voigt distribution function. PL spectrum for sample R obtained at 9 K is shown in Fig 4.18 as an example.

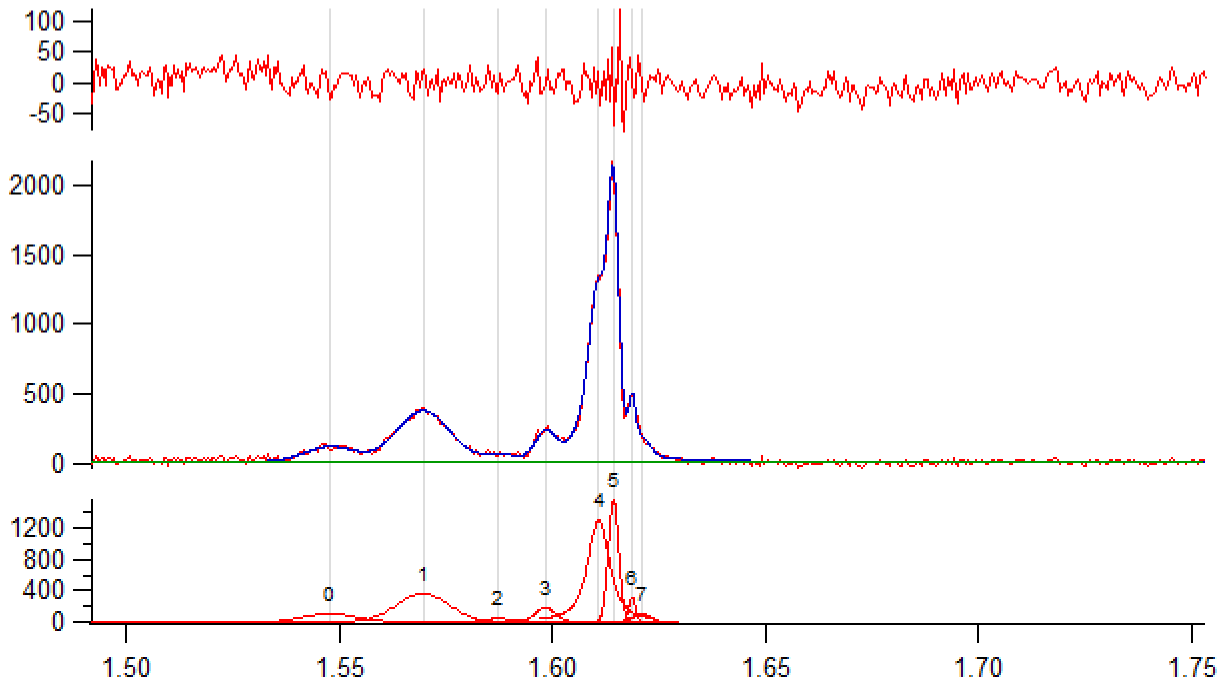

Figure 4.18: PL spectrum of sample R obtained at 9 K. (top) Residual plot showing peak fitting quality, (middle) PL spectra of the sample (red) overlaid on the sum of the Gaussian analysis results (blue); and (bottom) peaks used to produce curve fitting equation

Seven peaks, shown in the bottom graph of Figure 4.18, were used to resolve the data from a typical PL low temperature spectrum. The top graph shows the residual plot, where a better quality of the fit results in the least amount of fluctuation. This example spectrum had a very good quality fitting result.

In order to determine the type of emission from each PL peak (donor-acceptor pair (DAP), free exciton or excitonic), the PL intensity was analyzed by varying the laser intensity. This information was used to determine which fitting function, Equation 4.8 or 4.9, was to be used when the PL intensity was studied by observing any changes while increasing the temperature.

The value of studying how the PL intensity changes with temperature is calculating the binding energies of donors and acceptors. The temperature dependence of the integrated intensity, $I(T_o)$, is expressed by the excitonic Arrhenious fitting function in Equation 4.8 [48].

$$I(T_o) = \frac{I_0}{(1 + C_1 * \exp(-\frac{E_1}{k\,T})} \qquad \textbf{4.8}$$

In the excitonic Arrhenius function (Equation 4.8), I_0 is the highest point on the y-axis, C_1 is a fitting parameter representing the process rate, E_1 is the activation energy, and T_0 is the temperature the experiment was performed at. Although this function has been found to fit the data well in higher temperature ranges, it has been shown to be poor over a large temperature range. However, this function was suitable for fitting the data for the excitonic emissions because of their higher recombination energies, when compared to DAP emissions. These higher recombination energy excitonic peaks are less affected by thermal quenching and still remain detectable at higher temperatures [48].

For DAP emissions Equation 4.9 required two modifications to produce an accurate fit: (1) DAP emissions are detectable at lower temperatures so a second activation energy and process rate parameter was added ($\phi_1 T^{\frac{3}{2}}$) to increase the flexibility and sensitivity of the fit at lower temperatures and (2) the change in PL intensity as a function of electron/hole density (N_{eh}), and the radiative recombination probability of DAP (C_{DA}) was considered into the analysis. It has been shown that as the temperature is increased, the temperature dependence of both N_{eh} and C_{DA} is determined by the thermal velocity of free carriers and the temperature dependence of the capture cross sections of the defects. Previous experiments have also shown that N_{eh} and C_{DA} = ~$T^{-3/2}$ have given a reasonable approximation and this results in the DAP Arrhenius fitting function used for DAP emissions and shown in Equation 4.9 [48].

$$I(T) = \frac{I_0}{(1 + \phi_1 T^{\frac{3}{2}} + \phi_2 T^{\frac{3}{2}} * \exp(\frac{-E_d}{k\,T})} \qquad \textbf{4.9}$$

In the DAP emission fitting function shown in Equation 4.9, I_0 is the highest point on the y-axis, ϕ_1 and ϕ_2 are fitting parameters, T is the temperature the experiment was performed and E_d is the band gap. The equations for excitonic and DAP emissions used were manually added into the IGOR software package to build the fitting functions.

4.3.1.2.1 Low Temperature PL Emission Spectrum

The PL spectrum of Sample R was studied at 8K. The results from the power and temperature dependence studies and literature [21, 49] were used to identify the type of emission present and to assign each PL peak (Fig. 4.19).

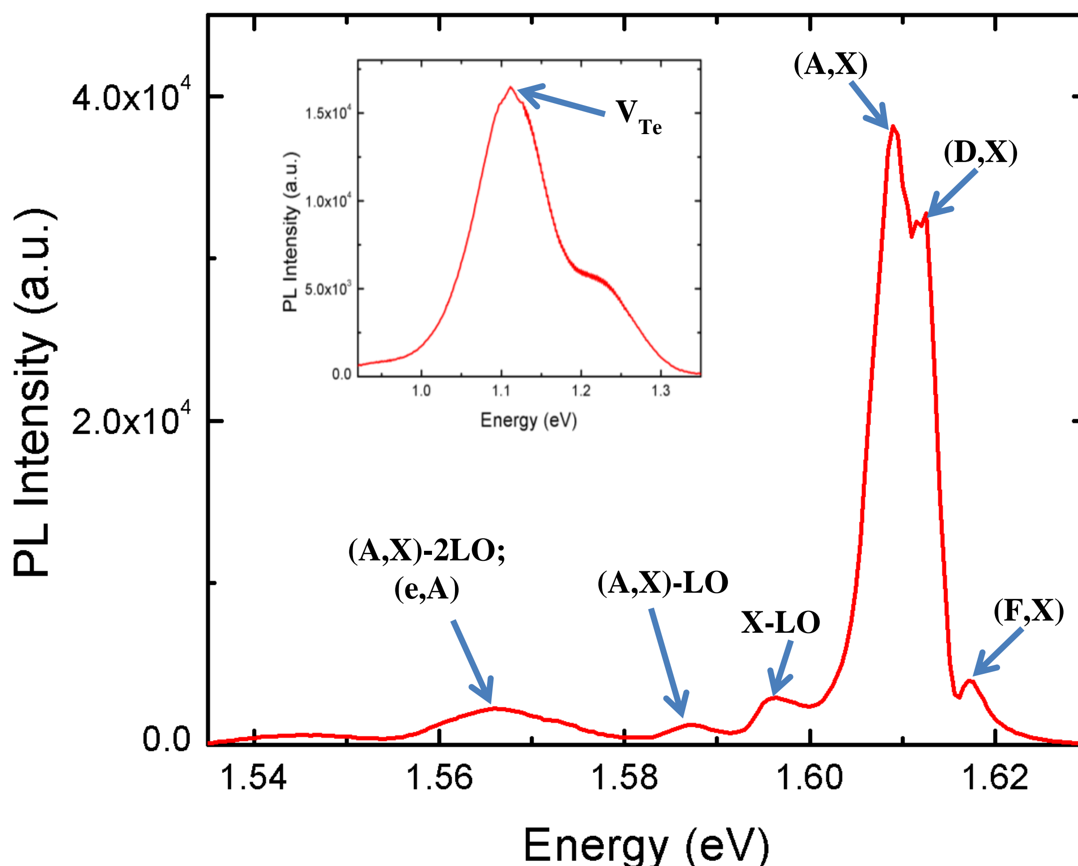

Figure 4.19: Identification of the PL emission peaks in sample Sample R at 8K

The low temperature emission spectra showed the presence of a free exciton (F,X) at the highest range of the energy scale (1.619 eV), followed by a donor bound exciton (D,X) and acceptor bound exciton (A,X) emissions around the 1.611-1.614 eV positions. The (A,X) emission is more dominant with p-type material. The X-LO and (A,X)-LO peaks are attributed to longitudinal optical phonon replicas and were determined by the incremental spacing from the (F,X) and (A,X). The donor-acceptor peak (e,A) and (A,X)-2LO peaks were noted in the 1.567 eV range. The (A,X)-2LO photon replica peak appeared in double the eV away from the (A,X)

peak. No signal was observed in the PL spectrum between 1.53 eV and 1.3 eV. Lastly, for the lowest range in the eV spectrum, the 1.1 eV peak was consistent with a Te vacancy, V_{Te}.

4.3.1.2.2 Laser Power Intensity Measurement

Sample R was used for the laser power intensity measurement. Equation 4.10 [41, 50] shows the change in the PL spectra as the laser energy is gradually decreased from 5 mW to 0.75 mW using neutral density filters. A neutral density filter (ND) is a glass filter placed in front of the excitation power source which allows only a set percentage of the excitation to pass. The amount of excitation power which passes is denoted by the ND number (i.e. ND 97 allows 97% of the excitation power to pass).

$$PL\ Intensity \propto P^{\gamma} \qquad \textbf{4.10}$$

In this expression, P is the laser intensity and γ is an exponent which describes the rate at which the PL intensity increases with increasing excitation power. The γ exponent depends on the nature of the radiative recombination process, and different processes can be categorized based on the value of γ. A plot of the PL spectrum as a function of laser power is shown in Fig.4.20.

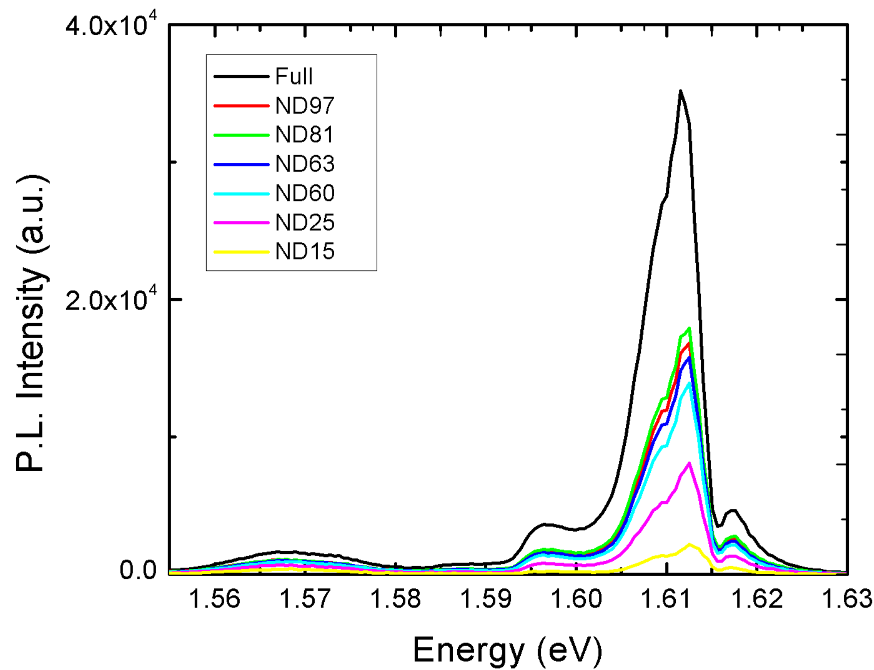

Figure 4.20: Power dependence study for Sample R showing changes in peaks with decrease in laser power. The decrease in power is achieved with a smaller number of the ND filter

As the excitation power was decreased, the intensity of the PL emission also decreased. Additionally, the peaks were noted to blue shift, moving right on the energy axis, as the power was decreased. The plots of log(PL Intensity) vs. log(Power) were linear for each peak in the spectrum indicating that the PL Intensity is a power law function of the excitation intensity. The exponent, γ, in the power law provides information on the nature of the centre or defect that is emitting [43, 50]. For example a donor-acceptor pair (DAP) recombination is characterized by an exponent between 0 and 1, a free exciton has a slope of 1 and an excitonic emission has a slope between 1 and 2 [50, 51]. The fits for all the peaks are shown next in Figure 4.21 to Figure 4.27.

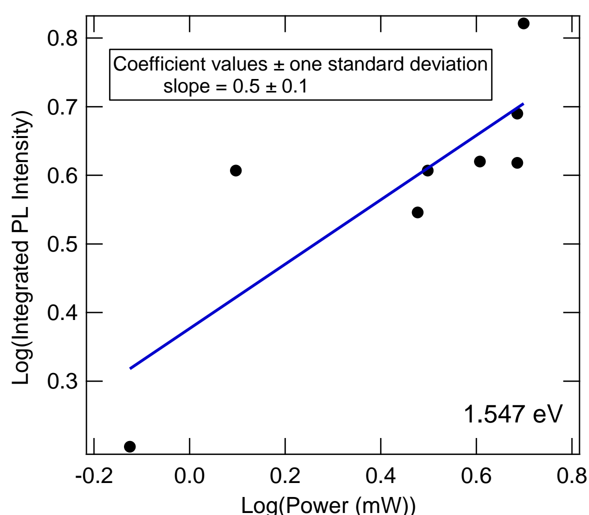

Figure 4.21: Power dependence fit for 1.547 eV peak

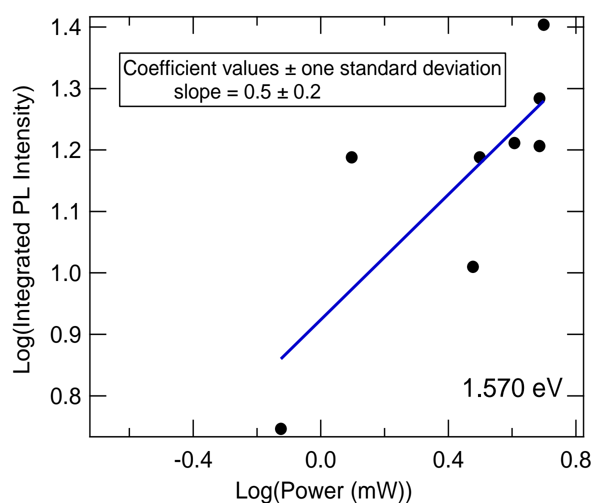

Figure 4.22: Power dependence fit for 1.570 eV donor acceptor pair (DAP) peak

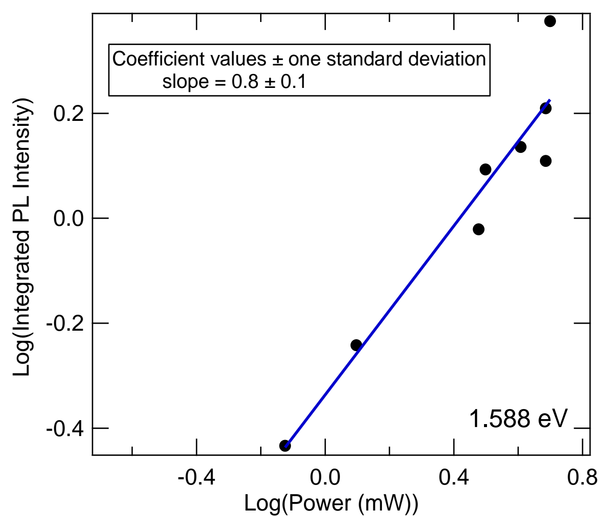

Figure 4.23: Power dependence fit for 1.588 eV (A,X)-LO longitudinal optical phonon replica peak

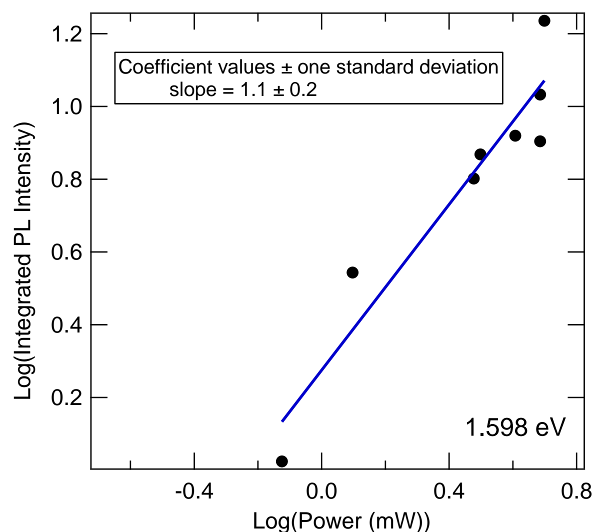

Figure 4.24: Power dependence fit for 1.598 eV X-LO longitudinal optical phonon replica peak

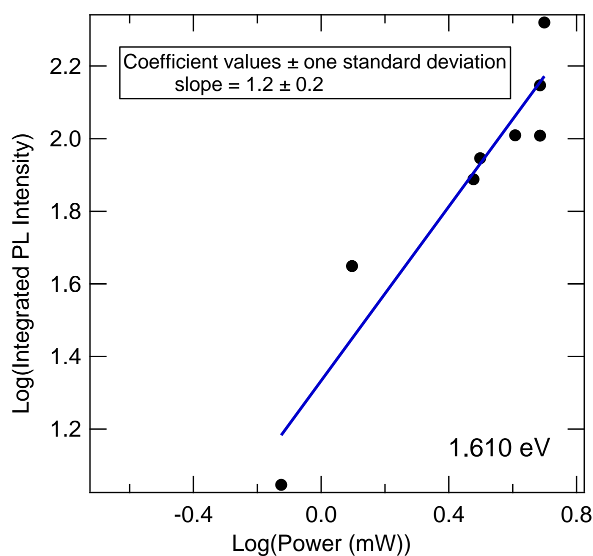

Figure 4.25: Power dependence fit for bound acceptor (A,X) 1.610 eV peak

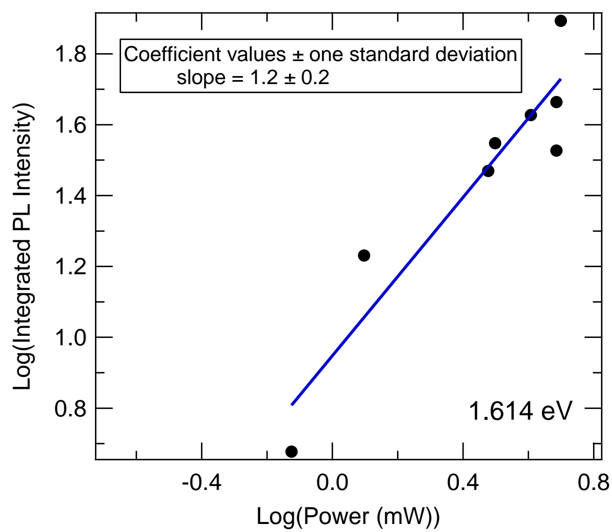

Figure 4.26: Power dependence fit for 1.614 eV bound donor (D,X) peak

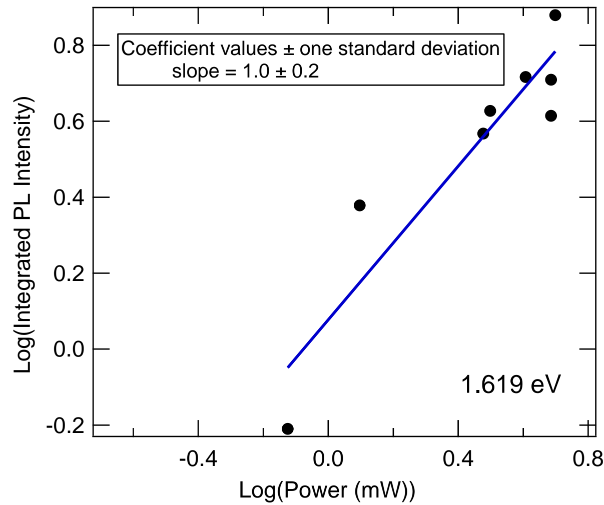

Figure 4.27: Power dependence fit for 1.619 eV free exciton (F,X) peak

Table 4.3 summarizes the type of emission which was observed for each energy level.

Table 4.3: Summary of emission types observed at different peak energies

Peak Energy [eV]	*Slope*	*Type of Emission*	*Peak Identification*
1.547	0.5 ± 0.1	Donor-Acceptor Pair	-
1.570	0.5 ± 0.2	Donor-Acceptor Pair	DAP
1.588	0.8 ± 0.1	Donor-Acceptor Pair	(A,X)-LO
1.598	1.1 ± 0.2	Excitonic	X-LO
1.610	1.2 ± 0.2	Excitonic	(A,X)
1.614	1.2 ± 0.2	Excitonic	(D,X)
1.619	1.0 ± 0.2	Excitonic	Free Exciton

The results show that the 1.547 eV, 1.570 eV and 1.588 eV peaks are due to DAP recombination, and the 1.598 eV, 1.610 eV, 1.614 eV and 1.619 eV peaks are excitonic in nature. In DAP recombination events, the change in PL intensity due to a variation in the laser intensity is dependent on impurity related recombination. In the excitonic emission, only a small number of free electron-hole pairs form excitons, while most photo-excited carriers recombine with donor or acceptor defect states [50].

4.3.1.2.3 Temperature Dependence Curve Fit Plot

Sample R was used to study the temperature dependence on the PL emission. A spectrum was recorded at eleven different temperatures ranging from 9K to 300K. Fig. 4.28 and Fig. 4.29 show the change in the PL spectrum as the temperature was increased.

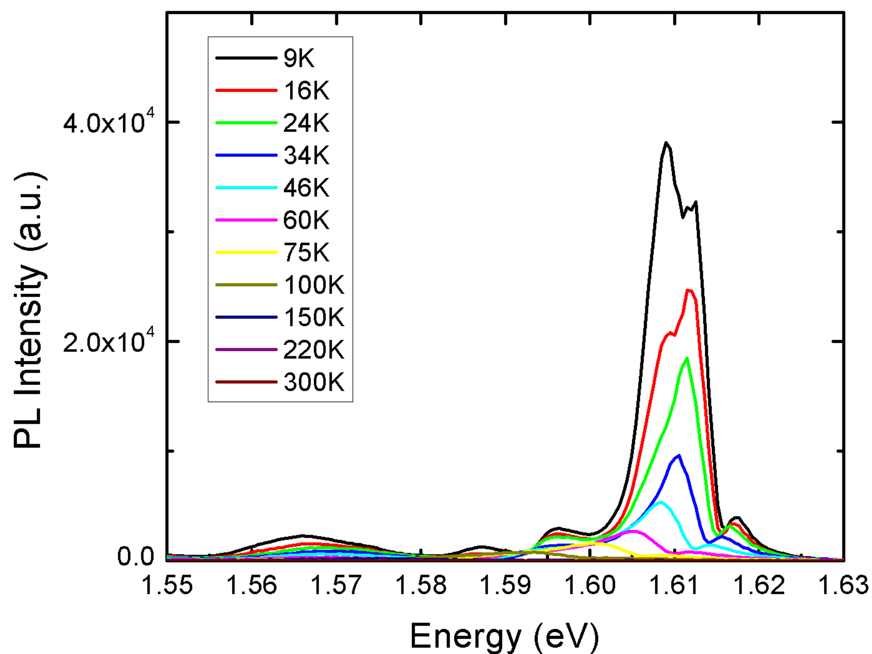

Figure 4.28: Temperature dependence plot of spectrum from 9K to 300K for Sample R

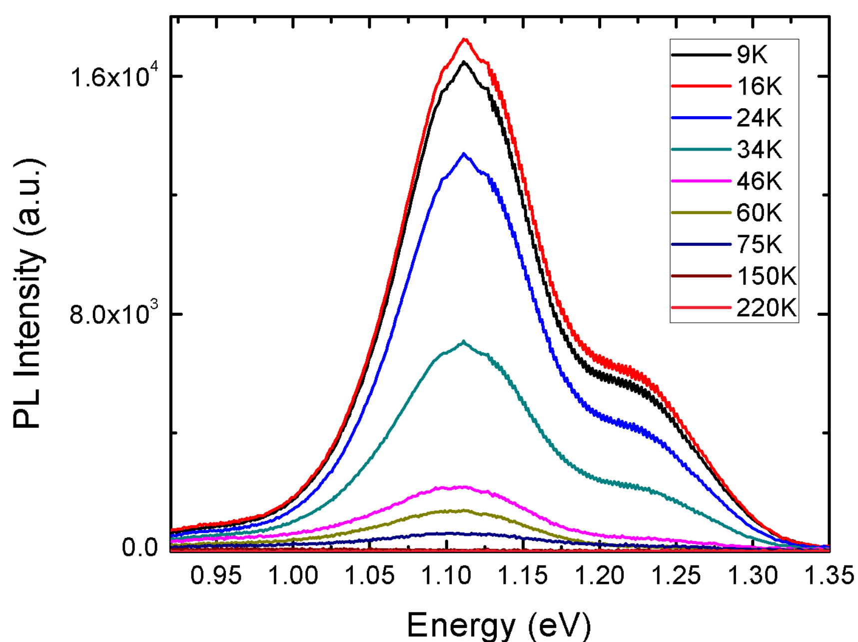

Figure 4.29: Tellurium vacancy temperature dependence spectrum plot from 9K to 220K

Each peak was analyzed depending on the type of emission as previously shown in Table 4.3 and the data was then curve fitted using Equation 4.9. The curve fittings for all DAP emissions are shown in Fig. 4.30 to Fig. 4.34.

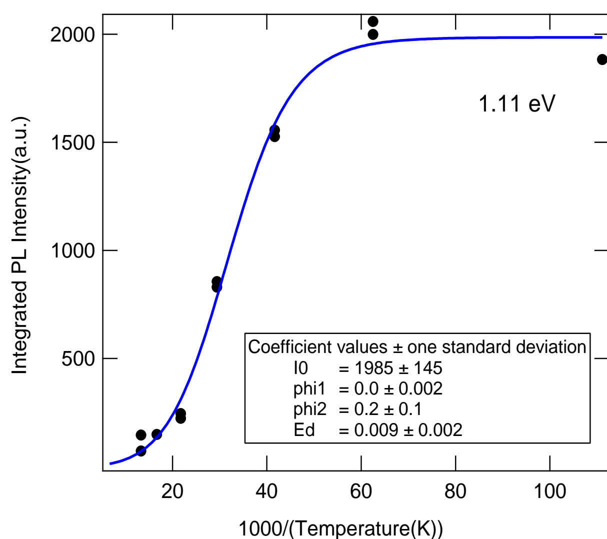

Figure 4.30: DAP Arrhenius fitting function results for Te vacancy peak at 1.11 eV

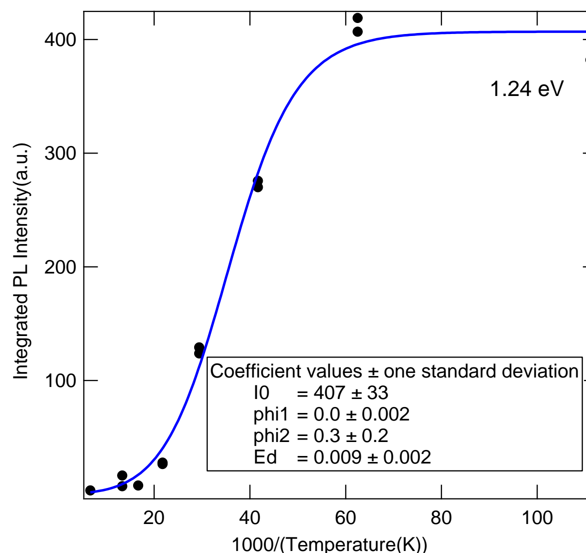

Figure 4.31: DAP Arrhenius fitting function results for the peak at 1.24 eV

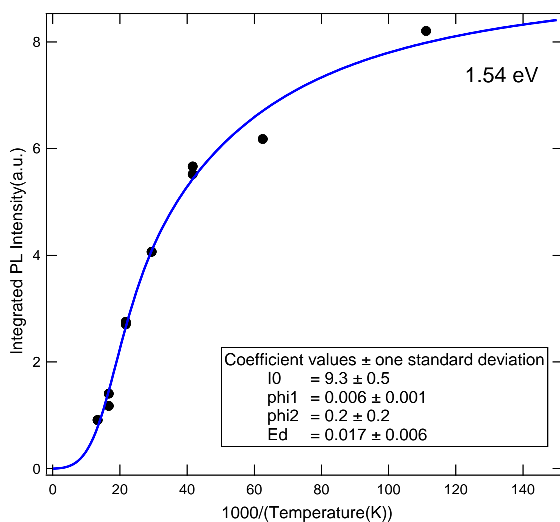

Figure 4.32: DAP Arrhenius fitting function results for the peak at 1.54 eV

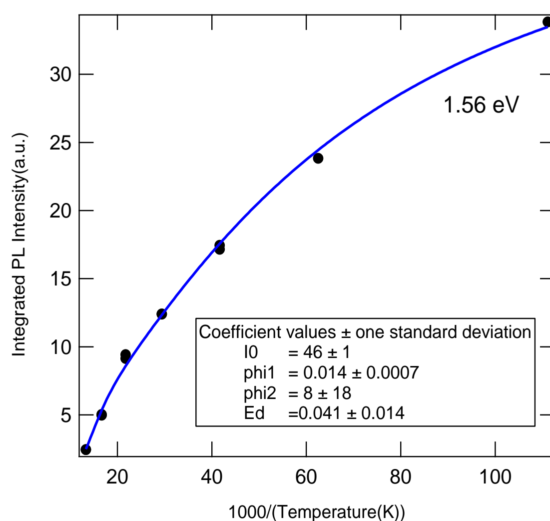

Figure 4.33: DAP Arrhenius fitting function results for the donor acceptor peak (DAP) at 1.56 eV

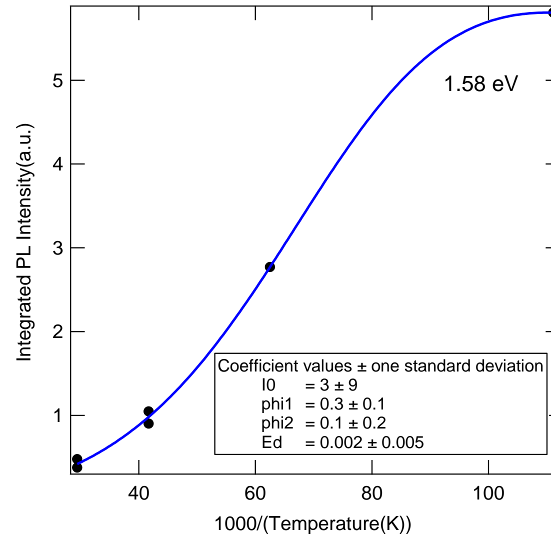

Figure 4.34: DAP Arrhenius fitting function results for the longitudinal optical replica (A,X)-LO peak

The fitting parameters which were used for the DAP emission fit are also summarized in Table 4.4.

Table 4.4: Fitting parameters for each energy of the DAP Arrhenius spectra (Fig. 4.30 to Fig. 4.34)

Energy [eV]	I_0	Φ_1	Φ_2	E_d *[meV]*
1.110	1985 ± 145	0.0 ± 0.002	0.2 ± 0.1	9 ± 0.002
1.240	407 ± 33	0.0 ± 0.002	0.3 ± 0.2	9 ± 0.002
1.540	9.3 ± 0.5	0.006 ± 0.001	0.2 ± 0.2	17 ± 6
1.560	46 ± 1	0.014 ± 0.0007	8 ± 18	41 ± 14
1.588	3 ± 9	0.3 ± 0.1	0.1 ± 0.2	2 ± 5

The curve fittings with the DAP Arrhenius function produced acceptable error margins for almost all fitting parameters. The fittings functions for the activation energies, E_d, showed larger error values which can be attributed to software limitations in the minimization process. Additionally, both of the fitting parameters Φ_1 and Φ_2 were found to be zero for the 1.110 eV and 1.240 eV peaks. This can be interpreted to mean that there is no temperature dependence on the band gap. The excitonic emissions were fitted with Excitonic Arrhenius (Equation 4.8) and the curve fitting for the Excitonic emissions are presented in Fig. 4.35 to Fig. 4.38.

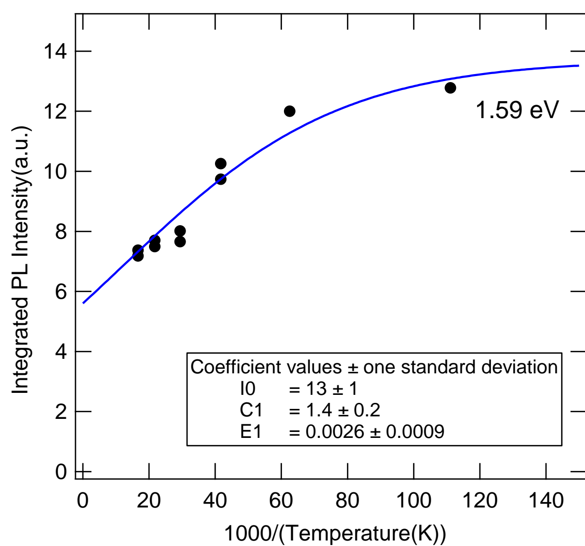

Figure 4.35: Excitonic Arrhenius fit for the 1.59 eV X-LO longitudinal optical phonon replica peak

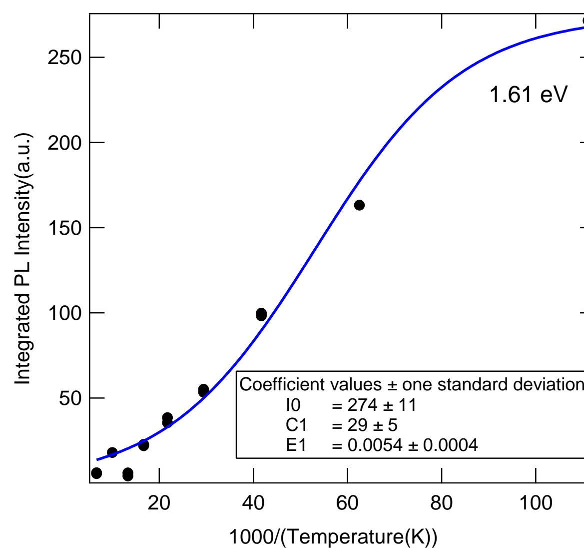

Figure 4.36: Excitonic Arrhenius fit for the 1.61 eV bound acceptor (A,X) peak

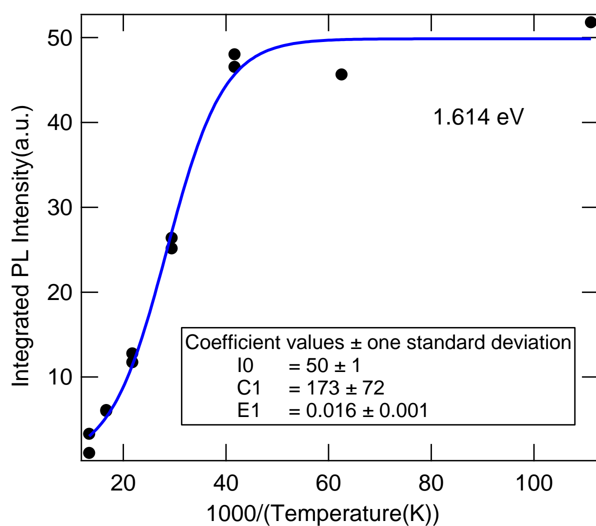

Figure 4.37: Excitonic Arrhenius fit for the 1.614 eV bound donor (D,X) peak

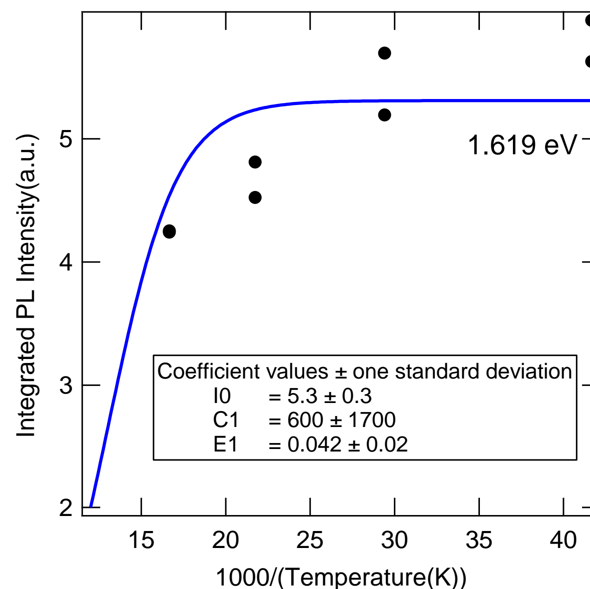

Figure 4.38: Excitonic Arrhenius fit for the 1.619 eV free exciton (F,X) peak

The fitted parameters for each of the excitonic peaks are also summarized in Table 4.5.

Table 4.5: Fitting parameters from the Excitonic temperature dependence fit using Equation 4.8 (Fig. 4.35 to Fig 4.38)

Energy [eV]	I_0	C_1	E_1 *[meV]*
1.590	13 ± 1	1.4 ± 0.2	26 ± 9
1.610	274 ± 11	29 ± 5	54 ± 4
1.614	50 ± 1	173 ± 72	156 ± 1
1.619	5.3 ± 0.3	600 ± 1700	420 ± 20

4.3.2 Hall Effect in Semiconductors

The Hall Effect in semiconductors was used to calculate the resistivity, density of carriers and the mobility of carriers in three samples (J, I and U). Each sample was examined by being mounted onto a van der Pauw device and connected to a current source via four electrical contacts placed at each corner. The contacts are labeled 1 through 4 in the counter-clockwise direction. A current is applied between contacts 1 and 2, I_{12}, and the voltage is measured between contacts 3 and 4, V_{34}. This experiment is repeated four times for each sample, and each time another two contacts are used for the current (I_{12}, I_{23}, I_{34}, and I_{14}) and for the voltage (V_{12}, V_{23}, V_{34}, and V_{14}). The results were recorded using LabView 6.0. Each current vs. voltage configuration was plotted and used to calculate the resistivity of each sample. The recorded I-V curves of Sample J (Fig. 4.39a), Sample I (Fig. 4.39b) and Sample U (Fig. 4.39c) are presented.

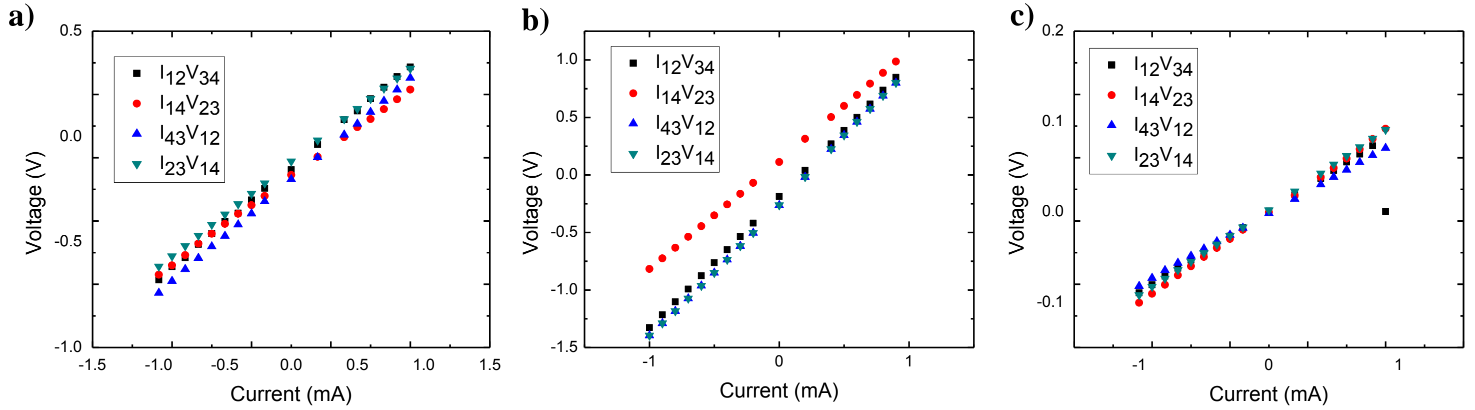

Figure 4.39: (a) I-V curves used to calculate the sheet resistance in Samples J, (b) Sample I and (c) Sample U

According to the van der Pauw method, two measurements of resistivity are obtained. These are shown in Equation 4.11 [46].

$$R_A = \frac{R_{41,32} + R_{14,23} + R_{23,14} + R_{32,41}}{4}$$

4.11

$$R_B = \frac{R_{32,24} + R_{43,12} + R_{12,43} + R_{21,34}}{4}$$

From the knowledge of the values for R_A and R_B and the material thickness, d, the sheet resistance, R_s, can be determined. The sheet resistance is a measure of the resistivity of thin films with uniform thickness, and is determined by the solution of Equation 4.12 [46].

$$q\left(\frac{-\pi R_A}{R_S}\right) + q\left(\frac{-\pi R_B}{R_S}\right) = 1 \qquad \textbf{4.12}$$

For square samples with approximate $R_A \approx R_B$ Equation. 4.12 can be manipulated to solve for the sheet resistance, R_s, and the resistivity, ρ, as presented in Equation 4.13 [46].

$$\rho = R_s d = \frac{\pi d}{\ln 2}\frac{(R_A + R_B)}{2} f \qquad \textbf{4.13}$$

where f is a correction factor for the sample's symmetry. The second part of the experiment involves calculating the Hall voltage. The Hall voltage is calculated using two sets of measurements: one with a magnetic field in the positive z-direction and one with a magnetic field in the negative z-direction. The direction of the magnetic field was reversed by flipping the sample inside the magnet. Unlike the sheet resistance measurement in which the voltage is

measured at terminals opposite the current ones, here the current is passed diagonally across the sample (I_{13}, I_{31}, I_{42}, I_{24}) and the voltage is measured at the opposing diagonal terminals (V_{24}, V_{13}, V_{42}, V_{31}). Eight IV curves are collected: four with the positive z-direction magnetic field and four with the negative z-direction magnetic field, and an average of all the readings is taken to find the Hall voltage. The positive and negative magnetic field I-V curves for Sample J, Sample I and Sample U are presented in Fig. 4.34 to Fig 4.42.

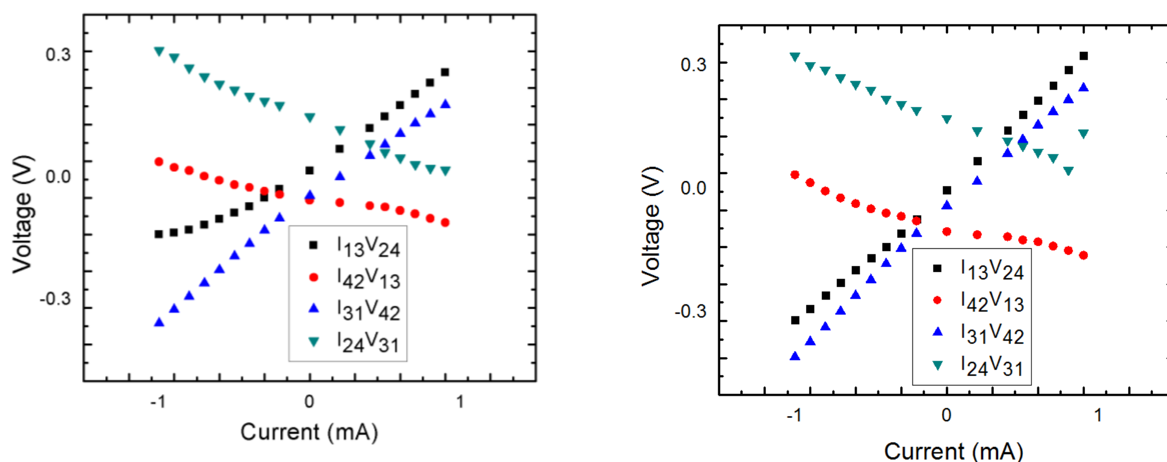

Figure 4.40: Negative magnetic field (left) and positive magnetic field (right) I-V curves used to calculate the Hall coefficient for Sample I

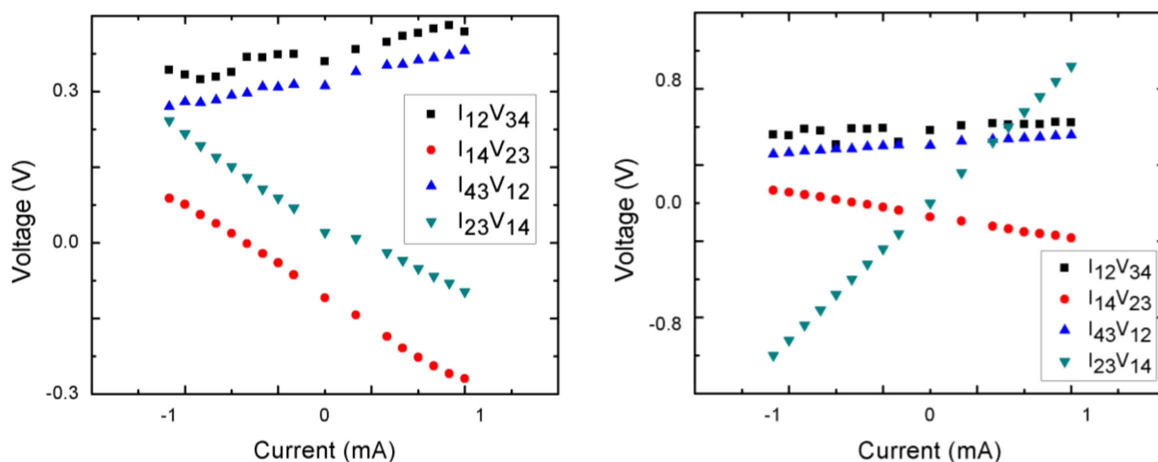

Figure 4.41: Negative magnetic field (left) and positive magnetic field (right) I-V curves used to calculate the Hall coefficient for Sample J

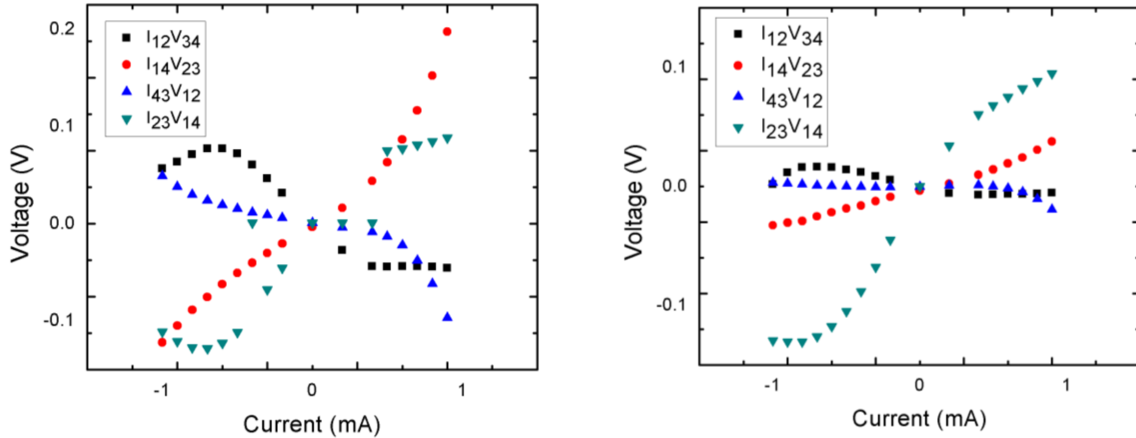

Figure 4.42: Negative magnetic field (left) and positive magnetic field (right) I-V curves used to calculate the Hall coefficient for Sample U

As can be seen by the shape of the I-V curves, not all plots (Fig. 4.40 and Fig. 4.42) showed the expected Ohmic linear relationship. This is attributed to non-Ohmic contacts, created by the resistance between the deposited contacts and the sample surface. This part of the experiment was used to measure the Hall voltage,V_H, from which the Hall coefficient, R_H, can be found using Equation 4.14 [46].

$$R_H = \frac{V_H d}{IB} \quad \textbf{4.14}$$

where d is the thickness of the sample, I is the current and B is the magnetic field strength. This result is used to calculate the density of carriers, n, using Equation 4.15.

$$n = \frac{1}{R_H q} \quad \textbf{4.15}$$

where q is the elementary charge. Lastly, the Hall coefficient and resistivity are used to determine the mobility of carriers, μ, using Equation 4.16.

$$\mu = \frac{R_H}{\rho} \quad \textbf{4.16}$$

The data was analyzed using a MATLAB code which calculated the carrier density, carrier mobility and type. The results from the experiment are summarized in Table 4.6.

Table 4.6: Hall Measurement results for Samples I, J, and U

Sample	*Orientation*	*Resistivity* [Ωm]	*Density of Carriers [cm^{-3}]*	*Mobility [cm^2/Vs]*	*Type*
J	211	1.69×10^3	2.63×10^{14}	82	p-type
I	211	4.79×10^3	4.16×10^{13}	184	p-type
U	111	4.00×10^3	1.48×10^{15}	62	p-type

The sign of the Hall voltage was used to determine the carrier type. The Hall voltage was positive, indicating all samples are p-type.

4.4 Discussion

4.4.1 Photoluminescence

4.4.1.1 Room Temperature Studies

The room temperature photoluminescence was used to calculate the molar Zn (%) concentration in the samples by curve fitting the data for the band gap value (Fig. 4.6 and Table 4.2). The bulk Zn concentration in the 29 samples was found to vary between 1.17% and 2.87%. The Zn concentration variation was also observed through micro-luminescence mapping and plotting the Zn distribution on contour maps (Fig. 4.10 to Fig. 4.17).

Deviation from the 4% Zn concentration was observed in both the [111] and [211] oriented samples. The Zn concentration depended on the location each sample was grown at in the boule. The principle reason for the variation of the Zn concentration is that CZT is subject to the effects of segregation. The ratio of concentration of a given atomic species in the solid phase to that in the liquid phase is known as the segregation coefficient, K. Segregation of different atomic species is an issue which arises during the growth process. The segregation coefficient for Zn in CdZnTe has a reported value of 1.35. As the value of K is greater than 1, the Zn concentration in the solid becomes higher than that in the melt leading to a depletion of Zn in the liquid. As the boule freezes, the Zn concentration along the boule is gradually reduced, resulting in a Zn distribution gradient. The segregation coefficient also results in an increased concentration gradient as the final parts of the boule solidify [52]. The last part of the boule is also most prone

to have impurities, as each impurity compound is governed by a different K and typically will segregate into the melt. Additionally to segregation, the Zn distribution is also affected by changes in the growth conditions such as temperature fluctuations at the growth interface due to convection [44]. The effects of segregation were also previously discussed in Section 2.2.2.

The samples used in this experiment all came from different larger tiles of CZT. The location in the boule that the tiles were removed from are unknown, therefore the variation between each sample suggests that they came from different places. Samples R and F showed the least variation of Zn on the surface, which suggest they came from the bottom of the boule. On the other hand, samples like Sample W, Y and BB showed a large Zn variation and likely came from the top of the boule. This level of micro-variation in the CZT atomic lattice has an impact on strain in the crystal because regions with a higher concentration of Zn will have locally different lattice constants. This results in a lattice mismatch between the two closely spaced regions, causing strain. The strain in the matrix is relieved by the formation of dislocations that lower the photoluminescence intensity by acting as non-radiative recombination sites for carriers [4]. Also strain shifts the photoluminescence emission energy and inhomogeneous strain will broaden photoluminescence emission lines.

4.4.1.2 Low Temperature Results

Low temperature (Temp < 20 K) PL spectroscopy carries a lot of information about the types of defects and the material's band structure. At the low temperatures PL is dominated by the lowest energy levels such as excitons which are electrons and holes bound together by Coulomb attraction, and shallow impurities such as donors and acceptors. These states are characterized by binding energies on the order of meV. The PL spectrum at 8 K, (Fig. 4.19) shows two energy regions from 1.50 eV to 1.60 eV and 1.60 eV to 1.70 eV. The 1.50 eV to 1.60 eV region is the donor-acceptor region consisting of the (D,A) transition and phonon replicas. The 1.60 eV to 1.70 eV region is the near band edge region which consists of free and bound exciton peaks. The second part of the high resolution spectrum from Sample R, near 1.1 eV, showed the presence of a Te vacancy, V_{Te}, defect [4].

The PL spectrum features can be divided into two categories: sharp lines and broad bands. The broad peaks are characteristic of radiative transitions at deep levels. Deep emissions are

attributed to states that are well separated from the band gap edges and have a low emission energy; thus having a broader emission peak. Sharper PL lines, which are strong and narrow, indicate a higher quality crystal, which is stress and defect free. Dislocations are known to reduce the PL signal and stress tends to shift and broaden PL peaks. Another feature observed in the spectrum includes peak splitting as seen at the (D,X) emission. Previous work by T.H. Gfroerer et al (2000) [41] indicates this is a result of thermal activation of carriers out of relatively sparse impurity-related traps, which make up the smaller quenched peak, whereas thermal population of the higher energy intrinsic state results in the upper peak. Impurity related traps catch carriers and act as bound donor traps [41].

Previous studies by K. Hjelt et al (1997) [51] show that the dominant peak in $Cd_{0.96}Zn_{0.04}Te$ is the acceptor bound exciton, (A^0,X) peak at 1.608 eV, especially in p-type material, which is consistent with what was observed in this experiment (Fig. 4.19). This acceptor bound peak is considered to originate from shallow neutral acceptors. The main prominence of the (A,X) peak is thought to originate from Cu impurities due to contamination during the growth [45] . The donor bound exciton (D,X) peak has been reported as less prominent in 4% Zn samples and is at 1.611 eV. The free exciton peak (F,X) is seen at 1.614 eV. This peak is often not resolvable from the (D,X) peak in lower quality material, however, it can be seen clearly in Fig. 4.19. Additionally, the binding energy difference between the (D,X) and (F,X) peaks has been reported to be 3 meV [43]. The results for Sample R are in agreement with this observation (F,X) 1.614 eV – (D,X) 1.611 eV = 3 meV.

The (e,A) peak at 1.567 eV is considered to be the luminescence from the electrons in the conduction band and the holes in the acceptors. The X-LO and (A,X)-LO peaks are due to the longitudinal optical (LO) phonon replicas. The reported energy difference between the (e,A), originating from the electron-phonon interaction, and its phonon replicas is 21 meV [44]. This is in an acceptable agreement with the data, which showed an energy difference of 28 meV. The shift toward this lower energy is thought to be a result of the donor binding energy [53]. The energy gap was determined from the free exciton luminescence E_g = (F,X) + 10.6 meV, which shows an energy gap of 1.625 eV which agrees with reported values for Zn = 0.04 material. The energy of the acceptor level was also found to be E_g – (e,A) = 0.065 eV. This value is 6 meV higher than previously reported work by H.Y. Lee at al (2001) [43]. The band around 1.1 eV has

been reported to result from Te vacancies. This agrees with the observed data which showed a peak at 1.11 eV. The DAP intensity located in the region of the (e,A) peak could not be resolved. This weak intensity emission form this region suggests that density of shallow donors is very low.

The origin of the peaks in the low temperature spectrum can be further understood by studying their behaviour as the intensity of the laser is varied. The rate of PL intensity variation with a change in excitation power, γ, was calculated by applying a linear fit to the data for each peak (Fig. 4.30 to Fig. 4.34). The value γ was used to categorize each peak emission as donor-accpetor pair, excitonic or a free excition. Previous studies by T.H. Gfroerer (2000) [41], showed that super linear dependence between the PL signal and the excitation power result under intermediate excitation, indicating a transition between nonradiative and radiative recombination regimes. The data in this case did not show this transition region, which means that it had radiative recombination dominated at all excitation-levels [41]. Additionally, the activation energy - used to gauge how much energy is needed for a carrier to escape a bound acceptor or donor trap - for the (A,X) peaks was found to be 4 meV which is in agreement with previously reported values [43].

It is observed that as the temperature increases, the intensity of the exciton luminescence peaks decrease quickly and also shift to a lower energy due to shrinkage in the energy gap [42]. As the temperature was raised from 9K to 16K, the (D,X) peak and the first (A,X)-LO were found to quench immediately. At the 16K temperature, a (A_2,X) peak appears in its place (Fig. 4.28), which is related to a shallow acceptor defect. Shallow levels lie near the edge of the conduction and valence edge and are more likely to participate in recombination [41]. As the temperature continues to rise, the two (A,X) peaks merge and loose definition due to band broadening. At this stage, no useful features can be further interpreted from those peaks. Lastly, as the temperature is increased the peaks all show a red-shift toward a lower energy (Fig 4.28). The red-shift in the peaks is attributed to the reduction in the band gap [42].

4.4.2 Hall Effect in Semiconductors

The resistivity and hole mobility results from the Hall Effect experiment were compared to other values calculated by researchers for $Cd_{0.96}Zn_{0.04}Te$ and $Cd_{0.96}Zn_{0.10}Te$ material. Previous work

showed that the resistivity for CZT with 4% Zinc was found to be 2.5 x 10^{10} Ω-cm [53] and the resistivity for CZT with 10% Zinc was found to be between the ranges of 4.33 x 10^{3} Ω-cm – 8.50 x 10^{6} Ω-cm [54] and 10^{9} - 10^{10} Ω-cm [55]. In this experiment, it was found that the resistivity of the samples varied between 1.69 x 10^{3} Ω-cm to 4.79 x 10^{3} Ω-cm, which is a factor seven lower when compared to other 4% zinc material but was in line with the bottom of the range previously reported for 10% Zn material. The samples showed a very low resistivity for both the [111] and [211] orientations. CZT has been shown to have low resistivity due to: (1) Te inclusions embedded in the CZT matrix which have a much higher conductivity than the parent material and (2) leakage current travelling through microcracks in the material [56]. Previous studies showed that the hole mobility for 4% zinc material was found to be 30 cm^2/Vs [4] and the hole mobility in material in 10% zinc material was found to be between 50 cm^2/Vs and 120 cm^2/Vs [4]. It can be seen that the calculated range from this experiment had values for hole mobility, 62 cm^2/Vs to 184 cm^2/Vs, which were found to agree with values reported in the literature.

Another possible contributing factor to the discrepancy with literature is the curved or asymmetric I-V plots observed with samples J and U. These have been previously observed and attributed to blocking, or also known as Schottky, contacts which form between the epoxy and the semiconductor [57].

Chapter 5
Connection Between Structure and Electronic Properties

This thesis set out to study the properties of $Cd_{0.96}Zn_{0.04}Te$ using five different characterization techniques. Up until now the results of each of the characterization methods were independently evaluated. This portion of the discussion brings all of the information from the study together and seeks to establish correlations between the characterization methods.

5.1 Effects of Strain on the Material Quality

Crystal lattice strain has a detrimental impact on the quality of the CZT material because it leads to dislocations. Strain is introduced into the lattice by: (1) lattice mismatch between atomic cells due to composition variations and/or (2) the presence of defects in the lattice, which result in distortion (3) or temperature gradients during growth. Lattice mismatch, created by a non-uniform Zn distribution throughout the matrix, was studied by mapping the change in Zn concentration in the samples using room temperature (RT) PL. The Zn (%) maps were then compared to the XRD peak shapes for each sample and it was observed that samples showing a large variation in Zn (%) concentration also had irregular XRD peaks. This was observed with both of the [111] and [211] oriented samples. Fig. 5.1 to 5.3 show several examples to support this.

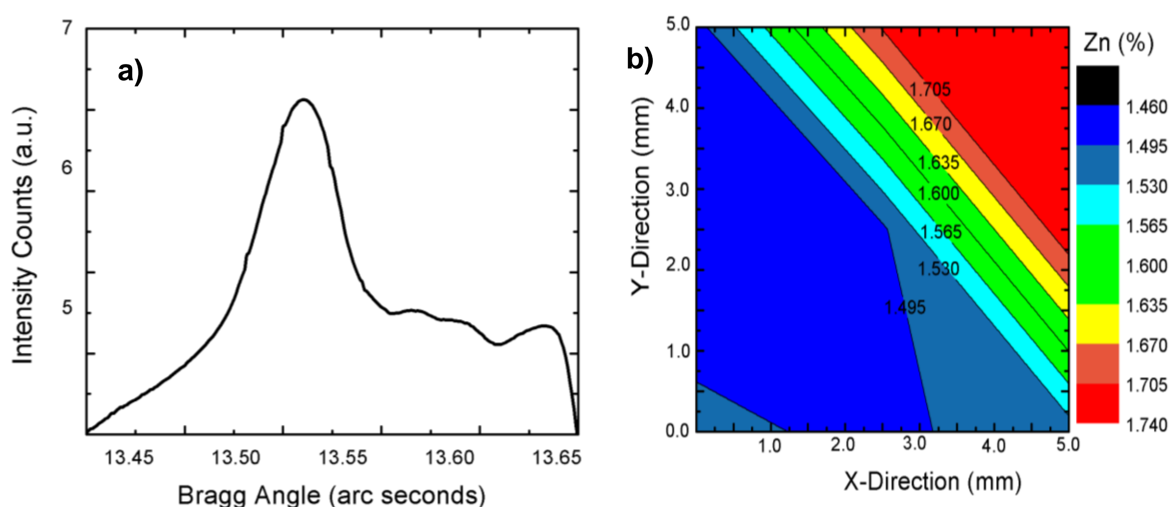

Figure 5.1: (a) XRD peak shape and (b) room temperature PL map for Sample W [111]

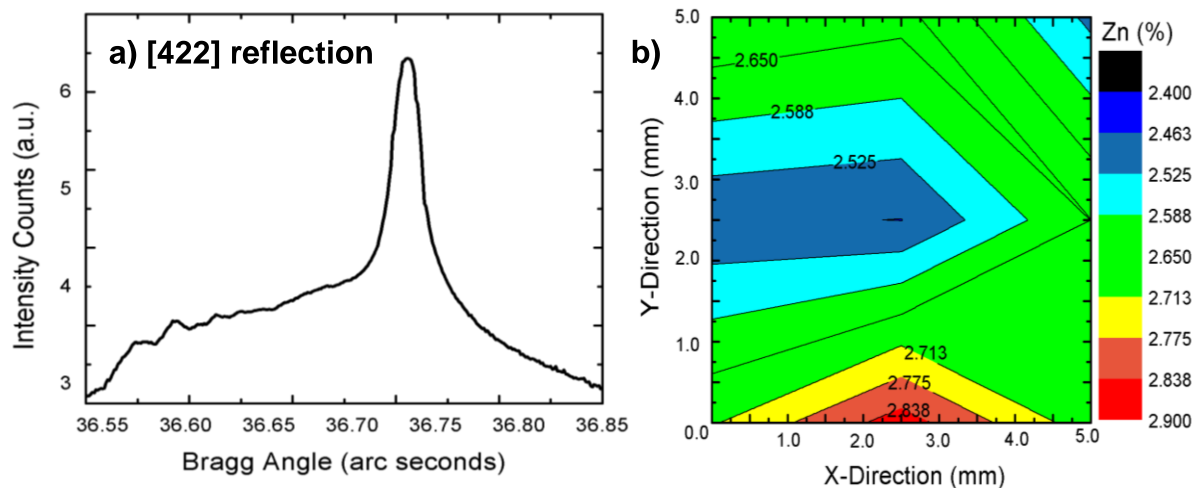

Figure 5.2: (a) XRD peak shape and (b) room temperature PL map for Sample N [211]

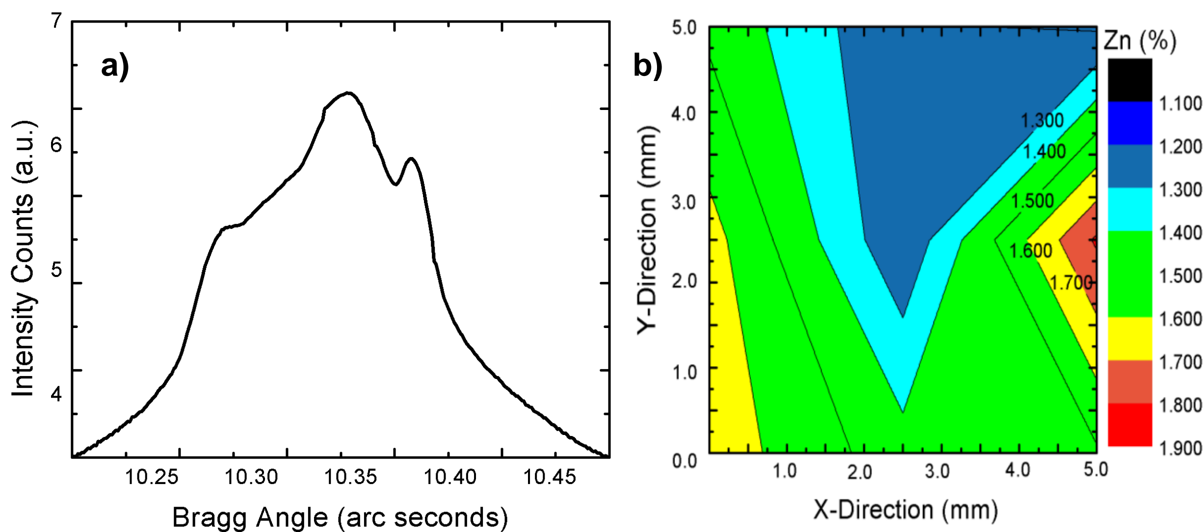

Figure 5.3: (a) XRD peak shape and (b) room temperature PL map for Sample U [111]

Splitting of the XRD peaks has been attributed to the presence of polycrystallinity in the matrix [30], such that areas with lattice mismatch form regions of similar local Zn concentration resulting in the formation of many small grains with different Zn concentrations. This leads to the development of thermal gradients and distortion in the lattice, which cause strain which becomes relieved by dislocations. Both polycrystallinity and defects formed as a mechanism of strain relief are contributors to lowering of photoluminescence intensity and broadening of the emission spectrum by acting as sites for non-radiative recombination. A concentration gradient in the Zn distribution has also been previously observed by other researchers [4, 30, 58], showing

that the Zn concentration changes along the boule due to the effects of segregation. However, the magnitude of the Zn concentration gradient with small areas, as studied here, had a more profound impact on the crystal quality when compared with the overall Zn gradient in the boule.

5.2 Zn Concentration Comparison Between XRD and PL Methods

The Zn concentration in all 29 samples was calculated by two methods: (1) XRD and (2) room temperature PL. The two methods produced different ranges for the Zn (%, molar) concentration. The PL values of Zn (%, molar) for each sample were lower than the values calculated from the XRD method. The Zn (%, molar) concentration from each method was plotted as a function of the other, Zn (%) from XRD vs. the Zn (%) from PL, in an effort to look for a correlation. A line of slope = 1 is also added to the graph showing that both [111] and [211] samples had a slope less than 1, which indicates a lack of correlation between Zn (%, molar) from XRD and the Zn (%, molar) from PL, (Figure 5.4).

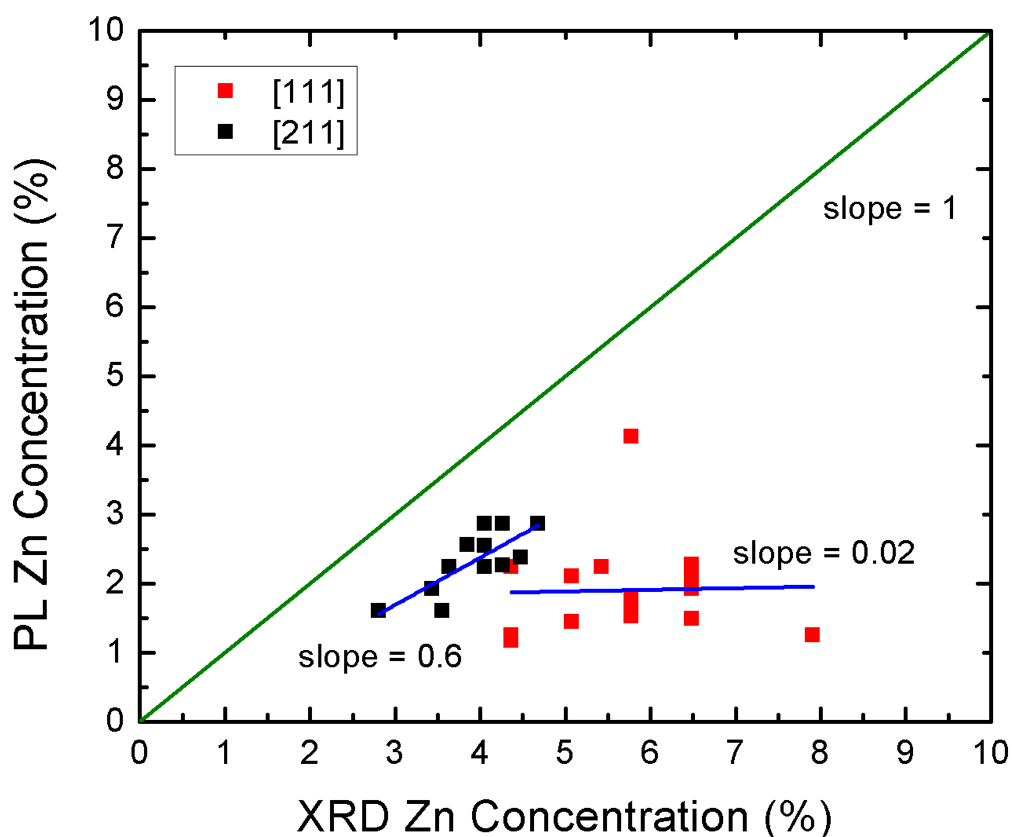

Figure 5.4: Plot of correlation between the Zn (%) molar concentrations found by XRD and by PL for each of the two crystal orientations

The results indicate that a weak correlation between the Zn concentrations from each method exist in the [111] growth orientation as the data is scattered. On the other hand, a linear trend was found for the Zn (%) molar concentration values in the [211] samples. Moreover, the values obtained by XRD were in close agreement with the intended 4% Zn growth concentration. Previous work by J. Lee et al (1994) [50] showed that room temperature PL studies were not a highly reliable method for predicting the band gap and thus the Zn molar concentration of the material. Room temperature measurements were generally found to produce lower band gap values due to difficulty in defining the precise band edge, and use of different curve fitting options used for the analysis.

5.3 Relationship between Lattice Disruptions and Electronic Broadening

A study between the FWHM of the XRD peaks and the FWHM of low temperature PL peaks was done. This aimed to see if a relationship between distortion in the lattice and the effects of electronic band broadening was present. FWHM broadening in XRD is caused by physical discontinuities or defects in the lattice structure. These defects result in disorder in the atomic arrangement which impacts the value of the Bragg angle. On the other hand, FWHM broadening in PL and the PL peak shape, are the result of fluctuations in the bandgap caused by lattice strain or composition variations. The impurity emission lines and shape can then be used to identify the types of states and transitions involved in the material [59]. The XRD FWHM was plotted against the FWHM of the (A,X), (e,A) and (F,X) low temperature PL emission peaks from Samples E, M, Q and BB (Fig 5.5).

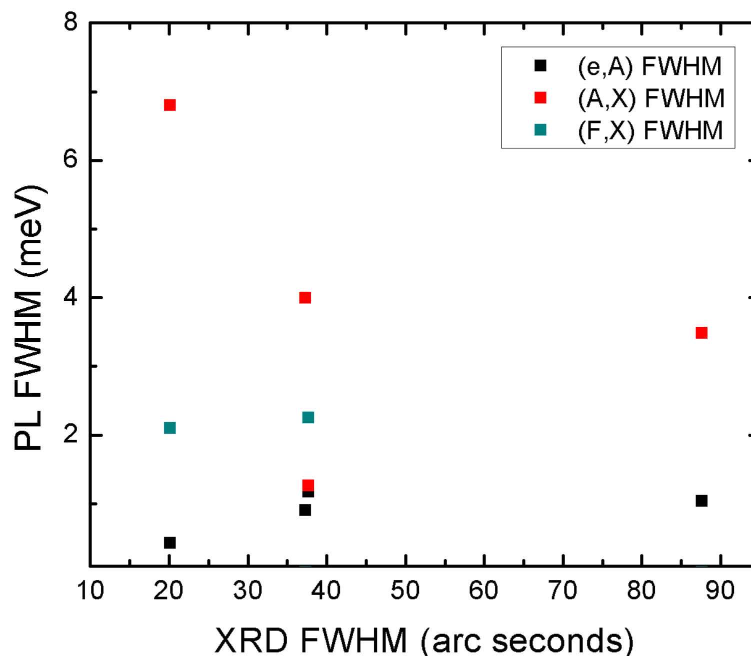

Figure 5.5: Plot of XRD peak FWHM and PL FWHM low temperature emission peaks from Samples E, M, Q and BB

This result shows that disturbances in the crystal lattice are related to defect band broadening for certain emission peaks. The (e,A) electrons in conduction band emissions shows that as the XRD FWHM increases, the width of the PL FWHM also increases. This means that more disorder in the atomic lattice results in a broadening of the conduction band. However, the effect of XRD FWHM broadening is not a strong influencing factor on the PL FWHM increase for (e,A) emission types because the value of the (e,A) emission FWHM stabilizes quickly (~1 meV) as the XRD FWHM increases.

On the other hand, the (A,X) bound acceptor emission trend line indicates that broadening in the XRD FWHM has a narrowing effect on the (A,X) band because the (A,X) FWHM decreased with the increase in XRD FWHM. This suggests that (A,X) complexes are more commonly observed in higher grade crystals, which have a narrower XRD FWHM. Lastly, the free exciton emission (F,X) was only observed in two of the four samples (Samples M and BB). Both samples appeared to have a similar PL FWHM with increasing XRD FWHM, suggesting that the distortions in the lattice do not have an effect on the free exciton peak (F,X). However, only two data points are available for (F,X), therefore this trend carries some uncertainty.

5.4 Relationship between Etch Pit Density and XRD FWHM

Etch pit density (EPD) is considered to be an important indicator of the crystal quality as it is thought to represent a count of the dislocation density in the material [35]. The effect of etch pit density (EPD) on XRD FWHM was studied. The results from each of the Nakagawa (Fig. 5.6a) and Everson (Fig. 5.6b) etches are shown.

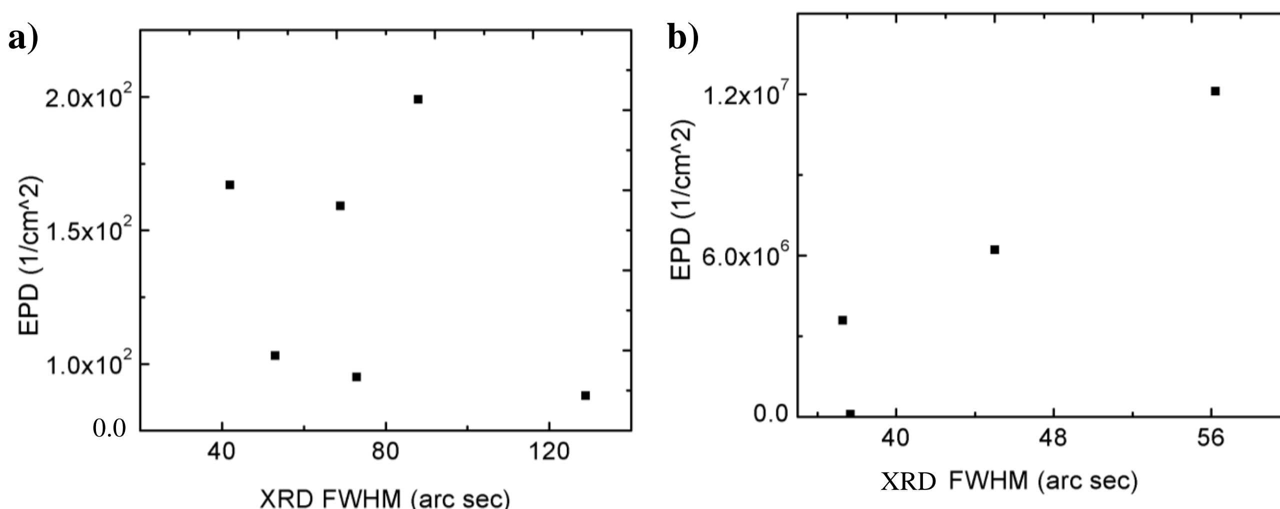

Figure 5.6: (a) Nakagawa etch EPD vs. XRD FWHM broadening and (b) Everson etch EPD vs. XRD FWHM broadening

The results of both etches showed that the density of defects generally increases with an increase in XRD FWHM. Outlier points were observed in each of the two EPD vs. XRD FWHM plots. The Nakagawa plot showed that Sample C (XRD FWHM ~130 arc seconds) had a very low EPD for the highest XRD FWHM and the Everson plot showed that no etch pits were observed on Sample M. Both the Nakagawa and Everson etching methods generally showed an increasing EPD with an increase in the XRD FWHM.

The most probable cause for the outliers is a failed etch which can occur when the surface of the sample remains pressed against the etching basket, thus limiting the sample's exposure to the etching solution. Additionally, the etch pit density was averaged by choosing two arbitrary locations on the sample and counting the number of etch pits there. The XRD and EPD experiments were done at different spots on the crystal which contributes to the error due to local variations in quality. The Everson EPD vs. XRD FWHM results were compared to similar work

by L. Burgess et al (2015) [36] and the results were found to be consistent in both cases. In both experiments, the etch pit density increased with an increase in the XRD FWHM value. Since both of these characterization methods are used to gauge the crystal quality of the material, an increase in one – thus meaning a lower quality material – is consistent with an expected increase in the other.

5.5 $Cd_{0.96}Zn_{0.04}Te$ Material Properties

Knowledge and understanding of a material's properties are paramount to choosing the correct material for a specific application and then exploring ways to optimize its functionality. Each of the five characterization methods used in this study provided important information about some of the key material properties of CZT. The properties calculated from XRD, TEM and etching provided information about the order of the atomic lattice. On the other hand, the results from the PL and the Hall Effect grade the electronic properties. The experimental material properties reported in this thesis are summarized in Table 5.1.

Table 5.1: Results of characterizing CZT samples

Material Property	Orientation	Units	Experimental Value
XRD FWHM Range	[111]	Arc seconds	45.00 – 161.28
	[422]	Arc seconds	20.17 – 138.08
XRD Zinc % Concentration Range	[111]	Percent	3.65 – 7.90
	[422]	Percent	2.81 – 4.68
PL Zn % Range	[111]	Percent	1.17 – 2.62
	[211]	Percent	1.97 -2.87
Band Gap	[111]	eV	1.508 – 1.511 (RT PL) 1.625 (LT PL)
	[211]	eV	1.506 – 1.511
Excitonic Emission Peak Energies	[111]	meV	1.598, 1.610, 1.614, 1.619
Donor-Acceptor Pair Peak Emission Energies	[111]	meV	1.547, 1.570, 1.588

Material Property	Orientation	Units	Experimental Value
Resistivity	[111]	Ohm-cm	4.00×10^3
	[211]	Ohm-cm	1.69×10^3 - 4.79×10^3
Mobility	[111]	cm/Vs	62
	[211]	cm/Vs	82-184
Etch Pit Density (EPD) - Nakagawa	[111]	cm^{-2}	8.75×10^1 - 1.67×10^2
Etch Pit Density (EPD) - Everson	[111] & [211]	cm^{-2}	7.96×10^4 - 1.21×10^7

All the experimentally obtained properties in Table 5.1 provided information about the 4% Zn material used in this thesis study. The results of this thesis showed that the values of the measured properties between [111] and [211] samples were very similar. This means that the [111] orientation is not preferential over the [211] orientation for use in commercial applications such as focal plane arrays.

Chapter 6
Conclusion

This thesis project set out to study the types of defects in $Cd_{0.96}Zn_{0.04}Te$ using a variety of experimental methodologies. A batch of 29 samples, comprised of [111] and [211] oriented crystals, were examined using five different characterization techniques. The goal was to look for correlations between the different techniques.

Three of the methods employed in this research – XRD, TEM and wet chemical etching – looked at the crystallinity of the samples. XRD and TEM used Bragg's law to gauge the deviation of the atomic arrangement due to the presence of precipitates and defects. TEM also allowed for visualizing the strain in the material by examining the CBED and HOLZ line patterns. Strain is a key contributor to the challenges with crystal growth of CZT because strain in the matrix is relieved by formation of dislocations. The method of wet chemical etching revealed etch pits on the material's surface at locations where the threading dislocations met the surface. These three methods allowed for characterizing atomic disturbances in the lattice, and their effects on the optical and electronic properties.

On the other hand, the methods of PL and the Hall Effect, looked at the electronic properties of the material. PL allowed for examining the effect of defects and alloying on the electronic structure. Unlike XRD or TEM, which use changes in the diffraction pattern to identify defects, PL uses the spectroscopic signature of the defects in the lattice to identify and to characterize them. A new way to fit the shape of the room temperature photoluminescence was developed that should be applicable to other semiconductor materials. The peak position of the PL spectrum did not follow the expected dependence of the band gap as a function of the Zn content. The dependence on Zn content was significantly weaker than expected. The reason for this discrepancy is not known. The Hall Effect showed further information about the electronic properties of the material by calculating the resistivity and the mobility of the carriers, which are two properties also influenced by the atomic lattice disorder.

These five distinct characterization methods were then evaluated by seeking to establish correlations between the results which were obtained. The three main findings of the thesis

included: (1) showing that a link between the XRD FWHM broadening existed with an increase in EPD, (2) that the shape and position of the XRD peak was affected by the variation in Zn concentration due to lattice mismatch and (3) the type of impact (or lack of) on the PL FWHM with an increase in XRD FWHM.

The other insight offered by researching the theory in this thesis study was the complexity of the crystal growth process and the paramount importance of controlling and optimizing the growth parameters. The origination of strain and defects in the lattice are the direct result of the growth conditions such as thermal gradients, retrograde solubility and the rates of solidification. All three of these factors result in strain in the CZT atomic lattice. Thermal gradients result in lattice strain due to differential thermal expansion. Other issues in CZT include the formation of Te precipitates during the growth due to a low Cd overpressure and an insufficient Cd reservoir and the effects of segregation cause variation in Zn concentration along the length of the crystal and introduce strain due to lattice mismatch.

It is recommended that future work on CZT focus on the growth stage of the material as well as exploring mitigation strategies in managing the defects in the material, some of which were discussed in this thesis. The many applications of CZT, such as early cancer detection and homeland security, show that there is great human benefit to further developing this technology - the future is bright!

References

[1] H. Chen, S. Awadalla, J. Mackenzie, R. Redden, G. Bindley, A. E. Bolotnikov, G. S. Camarda, G. Carini, R. B. James. “Characterization of Travelling Heater Method (THM) Grown CdZnTe Crystals”. *IEEE Transactions on Nuclear Science*, vol. 54, pp. 811-816, Aug. 2007.

[2] J. Mckenzie, *PCAMM 2014 Conference at University of Victoria*, 2014.

[3] M. Chu, S. Terteriam and D. Ting. “Role of Zinc in CdZnTe Radiation Detectors”. *IEEE Transactions on Nuclear Science*, vol. 51, pp. 2405-2411, 2004.

[4] T.E. Schlesinger, J.E. Toney, H. Yoon, E.Y. Lee, B.A. Brunett, L. Franks and R.B. James. “Cadmium zinc telluride and its use as a nuclear radiation detector material”. *Material Science and Engineering*, vol. 32, pp. 103-189, 2001.

[5] P. Rudolph, T. Boeck, and P. Schmidt. “Thermodiffusion and morphological stability in convectionless crystal growth systems from melts and melt-solutions”. *Crystal Research and Technology*, vol. 31, pp. 221-229, 1996.

[6] J. Clark, “Characterization of Durham CZT Detector Crystals,” M.Phy thesis, University of Surrey, 2010.

[7] P. Rudolph. “Fundamental studies on Bridgman growth of CdTe”. *Progress in Crystal Growth and Characterization of Materials*, vol. 29, pp. 275 – 381, 1994.

[8] W.G. Pfann. *Zone Melting (2nd Edition).* New York, USA: Wiley, 1966.

[9] C.H. Hanager Jr., D.J. Edwards, A.L. Schemer-Kohrn, M. Bliss, J.E. Jaffe. “Preferential orientation of Te particles in melt-grown CZT”. *Journal of Crystal Growth*, vol. 311, pp. 2641-2647, 2009.

[10] C. Szeles and M. Driver. “Growth and properties of semi-insualting CdZnTe for radiator detector applications”. *eV Products a division of II-IV Inc*., Saxonburd, 1998.

[11] R.B. James, B. Brunett, J. Heffelfinger, J. Van Scyoc, J. Lund, F.P. Doty, C.L. Lingren, R. Olsen, E. Cross, H. Hermon, H. Yoon, N. Hilton, M. Schieber, E.Y. Lee, J. Toney, T.E. Schlesinger, M. Groosky, W. Yao, H. Chen and A. Burger. “Material properties of large-volume cadmium zinc telluride crystals and their relationship to nuclear detector performance”. *Journal of Electronic Materials*, vol. 27, pp. 788-799, 1998.

[12] Szeles and Driver. SPIE Conf on Hard X-ray and Gamma-Ray Detector Physics, 1998.

[13] Ashcroft and Mermin, “Solid State Physics,” United States: Cenge Learning, 1976.

[14] M. A. Moram and M. E. Vickers. “X-ray diffraction of III-nitrides”. *Reports on Progress in Physics*, vol. 72, pp 1-33, 2009.

[15] D.B. Williams and C.B. Carter. *Transmission Electron Microscopy (Second Edition).* United States: Springer, 2009.

[16] B. Fultz and J. Howe. *Transmission Electron Microscopy and Diffractometry of Materials (Fourth Edition)*. United States: Springer, 2013.

[17] G. Nolze and A. Winkelmann. "Crystallometric and projective properties of Kikuchi diffraction patterns". *Journal of Applied Crystallography*, vol. 50, pp. 102-119, 2017.

[18] M. Tanaka and K. Tsuda. "Convergent-beam electron diffraction". *Journal of Electron Microscopy*, vol. 60, pp. 245-267, 2011.

[19] Hitachi. *Let's Familizarize Ourselves with the TEM.* Japan: Hitachi High-Technologies Corporation, 2009.

[20] Notten PHL, Van den Meerakker JEAM, Kelly JJ. E*tching of III–V semiconductors: an electrochemical approach*. Oxford: Elsevier; 1991.

[21] Pearton SJ, Ren F. "Wet chemical etching of compound semiconductors." *Electrochemical Society*, vol. 4, pp. 147–159, 2005.

[22] J.J. Kelly and H.G.G. Philipsen. "Anisotropy in the wet-etching of semiconductors". *Current Opinion in Solid State & Material Science*, vol. 9, pp. 84-90, 2005.

[23] I.M. Kotina, L.M. Tukhkonen, G.V. Patsekina, A.V. Schukarev and G.M. Gusinski. "Study of CdTe etching process in alcoholic solutions of Bromine". *Semiconductor Sci. Technology*, Vol. 13, pp. 890-894, 1998.

[24] F. Semendy, N. Bambha, M.C. Tamargo, A. Cavus, L. Zeng and N. Dai. "Etch Pit Studies of II-IV-Wide Bandgap Semiconductor Materials ZnSe, ZnCdSe, and ZnCdMgSe Grown on InP." *Army Research Laboratory*, October 1999.

[25] P. Capper. *Narrow-gap II-IV Compounds of Optoelectronic and Electromagnetic Applications.* Great Britain: T.J. Press International, 1997.

[26] SEMI International Standards. "Test Method for Determination of Dislocations Etch Pit Density in Monocrystals of III-IV Compound Semiconductors". *Semiconductor Equipment and Materials International*, 2014.

[27] G. Sivaranan. "Characterization of cadmium Zinc telluride solar cells". M.A.Sc. thesis, University of South Florida, South Florida, 2003.

[28] P.B. Hirsch, A. Howie, R.B. Nickolson, D.W. Parshley and M.J. Whelan. *Electron Microscopy of Thin Crystals*. Great Britain: London, 1965.

[29] D. Askland, P. Fulay and W. Wright. *The Science and Engineering of Materials (Sixth Edition).* Boston, MA: Cengage Learning, 2006.

[30] A.K. Garg, M. Srivastava, R.C. Narula, R.K. Bagai and V. Kumar. "Improvement in crystalline quality of CdZnTe (x=4%) crystals grown in graphite crucible". *Journal of Crystal Growth*, vol. 260, pp. 148-158, 2004.

[31] L. Xiaohua, J. Wanqi and Z. Yaohe. "Numerical analysis of CdZnTe crystal growth by the vertical Bridgman method using the accelerated crucible rotation technique". Journal

of Crystal Growth, vol. 47, pp. 22-31, 2000.

[32] M. Norouzpour and R. Herring. "Aberration-corrected self-interference of split higher order Laue zone line for measuring the z-dependent strain profile". *Materials Research Society*, vol. 32, pp. 996-1008, 2017.

[33] N. Armour. "*Etch Pit Density Measurement*." UVIC Crystal Growth Laboratory: University of Victoria, Victoria, 2015.

[34] K. Nakagawa, N. Naeda, S. Takeuchi. "Observation of dislocations in cadmium telluride by cathodoluminescence microscopy". *Applied Physics Letters*, vol. 34, pp. 574, 1979.

[35] X.P. Cui, W.Z. Fang, S.W. Sun, C.J. Zhang, H.L. Xu and J.R. Yang. "Characteristics of the dislocations in CdZnTe crystals revealed by etch pits". *Journal of Crystal Growth*, vol. 321, pp. 40-44, 2011.

[36] L. Burgess, F.J. Kumar and J. Mackenzie. "Orientation Dependence of Etch Pit Density in (111) and (211) CdZnTe Everson Etch*"*. *Journal of Electronic Materials*, vol. 44, pp. 3277-3282, 2015.

[37] Y. Xu, Y. He, T. Wang, R. Guo, W. Jie, P.J. Sellin and M. Veale. "Investigation of Te inclusions induced glides and corresponding dislocations in CdZnTe crystal". *CrystEngComm*, vol. 14, pp. 417-420, 2012.

[38] J. Schreiber, L. Horing, H. Uniewski, S. Hilderbrand and H.S. Leipner. "Recognition and Distribution of A(g) and B(g) Dislocations in Indentation Deformation Zones on {111} and {110} Surfaces of CdTe," Physica Status Solidi, vol. 171, pp. 89-97, (1999).

[39] Saleh and Teich. *Fundamentals of Photonics*. United States: Wiley Publishing, 2007.

[40] E.R. Weber. *Semiconductors and Semimetals*. Vol. 38, 1993.

[41] T.H. Gfroerer. "Photoluminescence in Analysis of Surfaces and Interfaces". *Encyclopaedia of Analytical Chemistry*, vol. 2, pp. 9202-9231, 2000.

[42] K. Suzuki, S. Setto, T. Sawda, K. Imai, M. Adachi and K. Inabe. "Photoluminescence measurements on undoped CdZnTe grown by the high-pressure Bridgman method". *Journal of Electronic Materials*, vol. 30, pp. 603-607, 2001.

[43] H.Y. Lee and T.W. Kang. "Temperature dependence of the optical properties in p-$Cd_{0.96}Zn_{0.04}Te$ single crystals". *Material Research Society*, vol. 16, pp. 2196-2199, 2001.

[44] R. Grill, J. Franc, P. Hlidek, I. Turkevych, E. Belas and P. Hoschl. "Defect-induced optical transitions in CdTe and $Cd_{0.96}Zn_{0.04}Te$". *Semiconductor Science and Technology*, vol. 17, pp. 1282-1287, 2002.

[45] S. Jain. "Photoluminescence Study of Cadmium Zinc Telluride". M.Phy thesis, West Virginia University, 2001.

[46] J. Colinge and C. Colinge. *Physics of Semiconductor Devices*. Boston, MA: Springer, 2002.

[47] Z.F. Li, G.S. Huang, J.R. Yang, L. He, and S.C. Shen. “Microluminescence mapping on CdZnTe: Zn distribution”. Journal of Applied Physics, vol. 90, pp. 260, 2001.

[48] J. Krustok, H. Collan and K. Hjelt. “Does and low-temperature Arrehnius plot of the photoluminescence intensity in CdTe point towards an erroneous activation energy?”. *Journal of Applied Physics*, vol. 3, pp. 1442-1445, 1997.

[49] R. Grill, J. Franc, P. Hlidek, I. Turkevych, E. Belas and P. Hoschl. “Defect-induced optical transitions in CdTe and $Cd_{0.96}Zn_{0.04}Te$”. *Semiconductor Science and Technology*, vol. 17, pp. 1282-1287, 2002.

[50] J. Lee, N.C. Giles, D. Rajavel and C.J. Summers. “Room-temperature band-edge photoluminescence from cadmium telluride”. *The Americal Physical Society*, vol. 3, pp. 1668-1676, 1994.

[51] K. Hjelt, M. Juvonen, T. Tuomi, S. Nenonen, E.E. Eissler and M. Bavdaz. “Photoluminescence of $Cd_{1-x}Zn_xTe$ crystals grown by High-Pressure Bridgman Technique”. *Physica Status Solidia*, vol. 162, pp. 747-763, 1997.

[52] R. Triboulet and P. Sliffert. *CdTe and related compounds; physics, defect, hetero- and nano-structures, crystal growth, surfaces and applications*. Amsterdam: European Materials Research Society Series, 2010.

[53] K. Zanio, Willardson, Beer, Teatise (Eds.). “Cadmium Telluride, Semiconductors and Semimetals”. *Academic Press*, vol. 13, pp. 53, 1978.

[54] Q.R. Hou, Y.B. Chen, H. Chen, Y.J. He and K.Y. Liu. “Characterization of CdZnTe Crystals by Resistivity Measurements and Chemical Issues”. *Modern Physics Letters*, vol. 16, pp. 615-619, 2002.

[55] G. Muller and G. Neumann. “Tenfold growth rates in the travelling heater method of GaSb crystals by forced convection on a centrifuge”. *Journal of Crystal Growth*, vol. 63, pp. 1-232, 1983.

[56] E. Belcarz, J. Chwaszczewska, M. Slapa, M. Szymczak, J. Tys. “Surface barrier lithium silicon detector with evaporated guard ring”. *Nuclear Instrumentation Methods*, vol. 27, pp. 21-28, 1970.

[57] M. Silver, M.P. Shaw, J. Mort and D.M. Pai. *Photoconductivity and Related Phenomena*. Amsterdam: Elsevier, pp.1-25, 1976.

[58] G. Dhanaraj, K. Byrappa, V. Prasad and M. Dudley. *Handbook in Crystal Growth*. Berlin: Springer, 2010.

[59] T.N. Morgan, “Broadening of Impurity Bands in Heavily Doped Semiconductors,” Physical Review, Vol. 139, No. 1A, 1965.

Appendix A
Details of TEM Sample Preparation

1. Selecting an Area for TEM Study

Due to the limited field of view in using a Transmission Electron Microscope (TEM), a suitable area for examination had to be selected. Three [111] oriented samples, not included in the 29 samples referenced in the other thesis experiments, were etched using the Nakagawa method. The theory and details of performing a Nakagawa etch are discussed in Section 3.1.3. The reason for etching the three samples first was to reveal etch pits on the surface. Notten et al (1991) [20] showed that etch pits form at dislocations sites. By choosing a location with a high etch pit density, the probability of studying a more defect prone region was increased. The goal of the study was to image any visible defects in the material.

The three etched [111] oriented samples were examined using an optical microscope (Olympus U-CMAD3 model) with a camera mount to confirm the success of the etch results. The three etched samples were then imaged using a Hitachi S-4800 scanning electron microscope (SEM) for a higher resolution and to select a TEM study site. Each sample was individually imaged by being placed on a small stage and secured using copper tape. The reason for using copper tape was to increase the conductivity of the sample, which reduces the aberration introduced by the charge up effect. If the sample is not conductive, a negative charge builds up on the specimen's surface and this can result in poor image quality [15].

The SEM (Hitachi S-4800) was used to image an area with several etch pits at a 150x magnification (Fig A.1a) and a 300x magnification (Fig. A.1b).

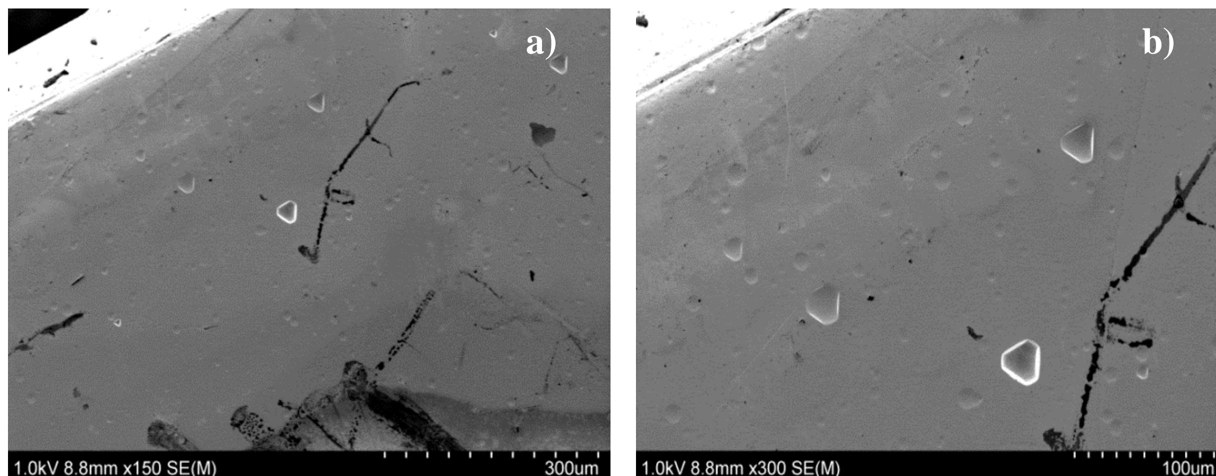

Figure A.1: SEM image showing etch pits at x150 magnification (left) and a zoomed in image at x300 magnification (right)

The large pit with white shadowing (Fig.A.1b) was selected due to its size and flat bottomed geometry. S.J. Pearton et al (2005) [21] showed that flat bottom pits correlate to tellurium inclusions or an intersection of dislocations. It was determined that this pit likely marked an area with more defects.

2 Sample Preparation Using the Lift-Out Process

Once the area of interest was identified, the next step was to use a sputtering chamber (Hummer Anatech Ltd.) to coat the sample with a mix of gold and palladium. The reason for this preparation step was twofold: (1) to protect the surface from damage during the lift-out and (2) to increase the conductivity of the sample lowering the charge up phenomenon. A mix of gold and palladium was used because the addition of palladium allows for reducing the deposition droplet size. The sputtering chamber is flushed with argon gas which is used as a medium to deposit the gold and palladium coating mixture. The machine was operated at 10 mA and the specimen was kept in the sputtering chamber for a total of two minutes.

Once the sample was adequately sputter coated, the focused ion beam (FIB) (Hitachi FB-2100) was used for the main part of sample preparation and the procedure is known as creating a “lift out”. The Hitachi FB-2100 system used for this experiment was the single beam unit. The first stage of the lift-out process was to align several of the available FIB beams. The FIB uses different strengths of focused Gallium beams for imaging, coating and fabrication. The viewing

beam allows the operator to see the sample and also has a wide range of magnification capabilities. It works by focusing gallium ions toward the surface of the specimen, these in turn knock out secondary electrons from the sample material, which are picked up by a detector and used to form a back scattered image.

The beam strengths are distinguished based on the operating voltage. In the case of CZT, the material was found to be very soft and easily damaged so low voltage beams were needed. The purpose of each beam is specified by the FB-2100 system manufacturers. The beams are indexed by their voltage, operation of the condenser aperture and the diameter of the aperture. The beams used for this experiment and their purpose are shown in Table A.1.

Table A.1: FIB beams used for the TEM sample preparation and their purpose

Beam	*Purpose*
30-0-30	Viewing beam and final finishing cuts
40-0-30	Deposition and final finishing cuts
40-0-80	Deposition
40-1-80	Rough cuts
40-1-150	Rough Cuts

The first number in the beam name is the voltage, the second number determines if the aperture is open or closed (0 = closed, 1 = open) and the last number is the diameter of the aperture. Once a beam was selected it had to be aligned. An iterative procedure was used to align the focus, stigmator (XX and XY) and the aligner. The focus controls the clarity of the image and can be tuned using a course, medium or fine setting. The stigmator corrects for the difference in focus of the beam in the XX and XY directions. Lastly, the alignment checks for the wobble in the beam, which is a measure of the stability.

A challenge with CZT is the softness of the material and the fact that is sustains damage during the beam alignment procedure, especially when using the higher voltage beams. Figs. A.2a and Fig. A.2b show the damage the sample sustained during the beam alignment.

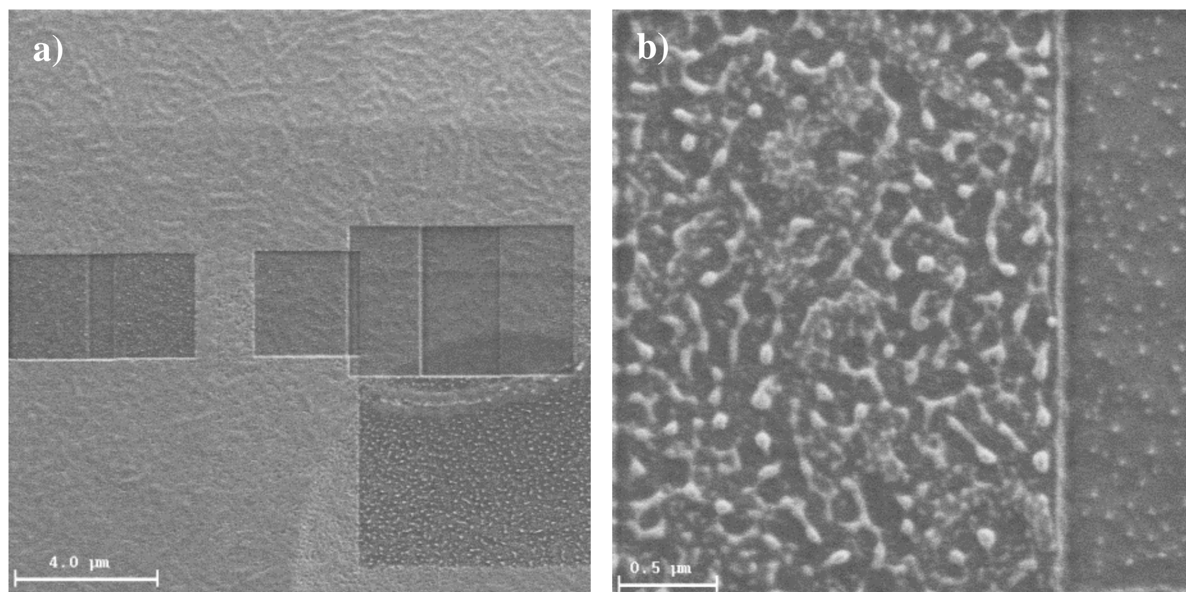

Figure A.2: Damage from FIB beam alignment (left) and a close up between a damaged and non-damaged area (right)

The darker contrast rectangles in Fig. A.2a are deeper trenches which were produced by the higher voltage beams. The towel-like structure in Fig. A.2b is due to the dissolution and recrystallization of the material which was melted by the gallium beam.

The next stage of the sample preparation was to use the 40-0-80 beam to deposit a Tungsten coating onto the sample to protect the surface. The deposition location was chosen to coincide with a large etch pit in Fig. A.3a and a close up in Fig. A.3b. Additionally, this is the same etch pit shown previously in Fig. A.2 using SEM.

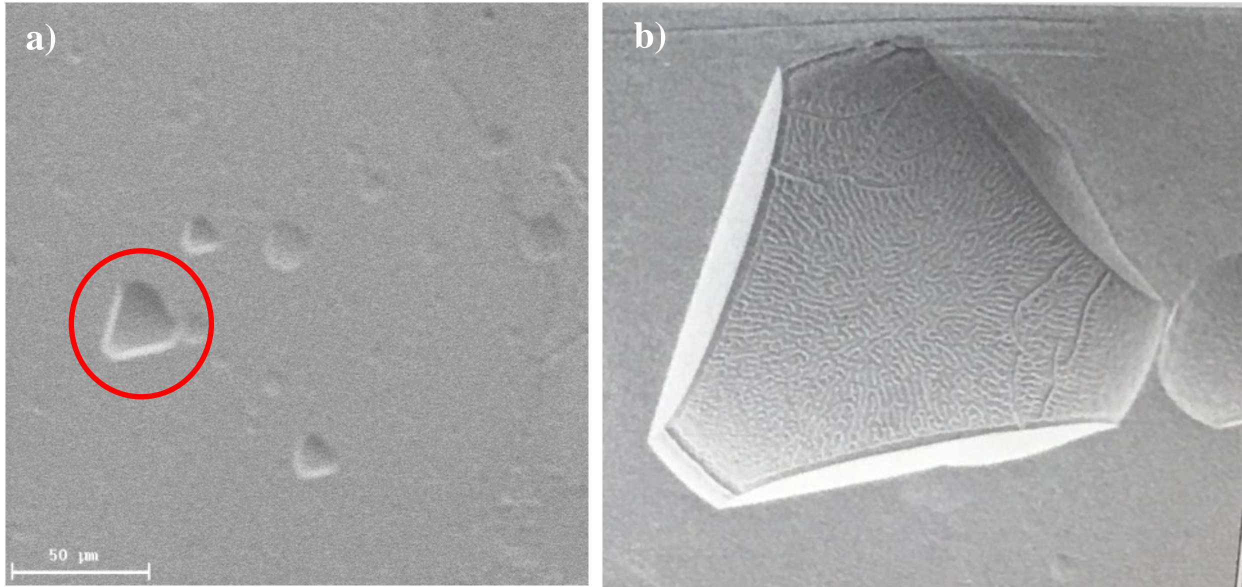

Figure A.3: FIB image showing an etch pit group found on Sample 3 (left) and a close up of the large etch pit circled in red (right)

The Tungsten deposition is controlled through a graphical user interface which allowed the operator to draw a box at the desired deposition location. The box was chosen to be 25 x 3 microns. The depth of the deposition was 5.48 microns at a stage rotation of 17 degrees and a beam dwell time of 60 microseconds. The main challenge faced during the deposition procedure was large instabilities in the beam. As each of the layers of Tungsten was deposited, the beam kept on moving slightly over the 10 minute process. Instead of depositing a large amount of Tungsten over the focused target area, the W spread thinly over a surrounding area. Fig. A.4a shows the beam drift and Fig. A.4b shows the final Tungsten covered area.

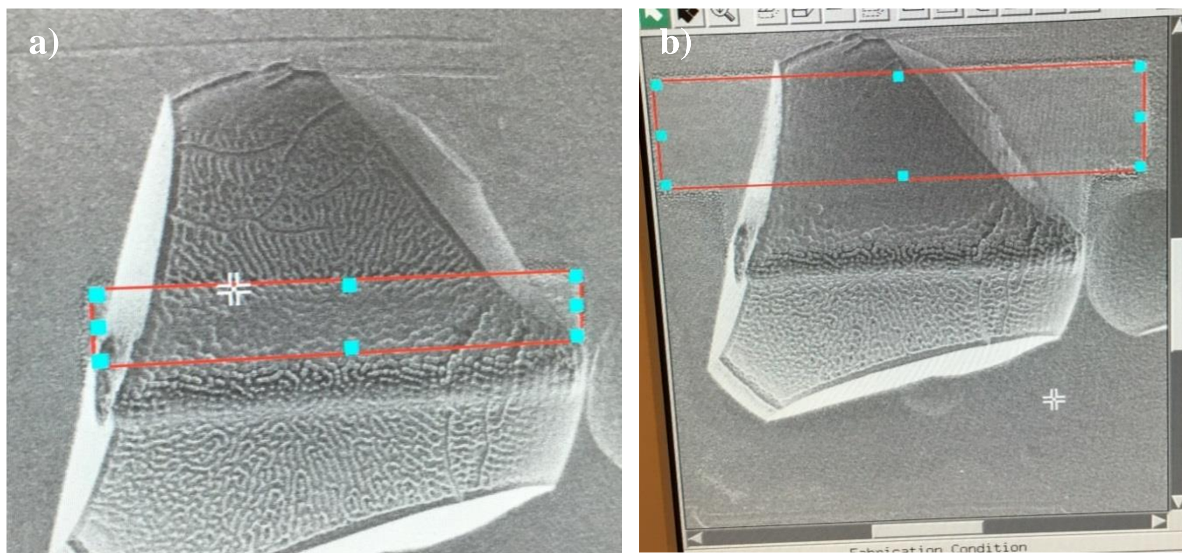

Figure A.4: Unwanted W deposition outside of red box (left) and final area covered with W in red box (right)

This issue required that multiple 10 minute passes were made to ensure that the area was adequately covered, ensuring adequate surface protection.

Once the deposition stage was finished, the sample had to be cut and lifted out from the parent specimen. In order to cut the sample more efficiently, beams with a higher voltage were used for the roughing cuts and beams with a lower voltage are used for the finer and finishing cuts. The cutting procedure implemented two deep trench cuts on each side of the sample, followed by two smaller cuts on the other two sides. A small portion remained attached to the parent sample to hold it in place. Fig. A.5a shows an isometric view of the sample during lift out and Fig. A.5b shows a top view of the sample and left over material holding it to the parent sample.

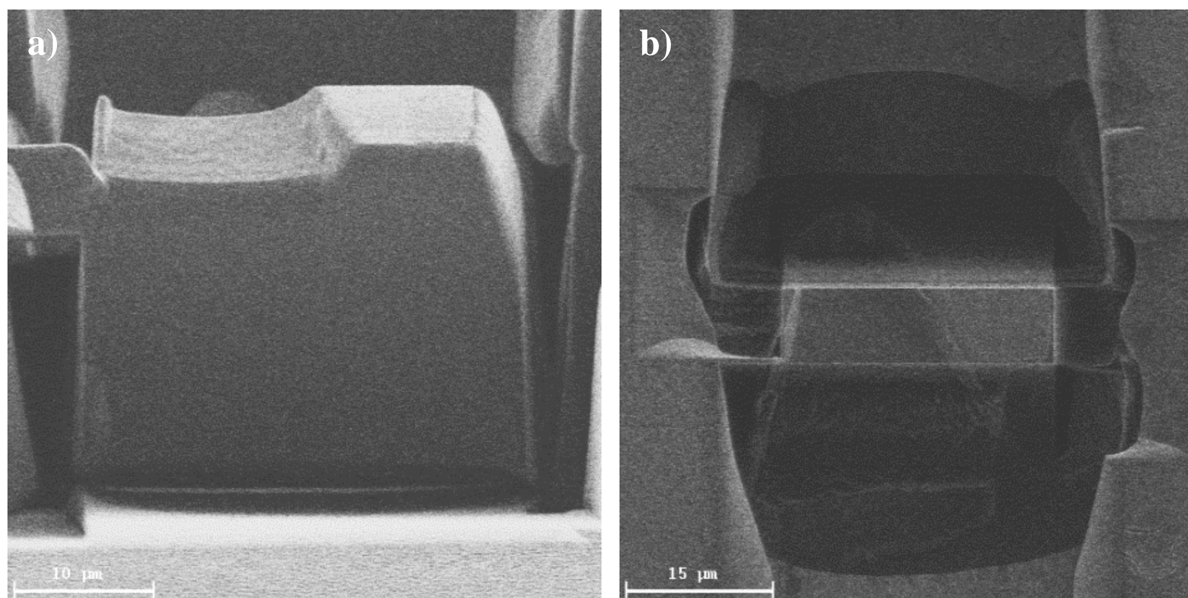

Figure A.5: Isometric view of lift out sample (left) and top view (right)

The sample cuts were made iteratively over two days (~20 hours) due to the softness of the material, which made it very challenging to work with. The heat and abrasion from the beam caused finer cuts to remove some material depositing it elsewhere. Another additional challenge with this process included the viewing angles which were available due to the limited 40 degree tilt of the FIB stage. This made it difficult to tell when a cut had been completed.

Next a holding probe was inserted into the FIB and the specimen was welded to it. Since the probe is re-usable, the tip had to be cut into the correct shape to fit the sample. The sputtering mode of the system was used to cut part of the probe and then bring it closer to the sample. The sample and probe were then welded to each other using Tungsten deposition. Lastly, the sample was cut out from the parent material and the lifted-out process was complete.

While the sample probe was still inserted in the FIB, a single tilt TEM holder (Fig. A.6) was inserted into the machine through a secondary port. The TEM holder is equipped with a copper grid, which was welded onto the sample for increasing the conductivity and reducing charge up phenomenon.

Figure A.6: TEM sample holder inserted into FIB in order to attach the specimen into the viewing area

Once the copper grid was attached, the sample was welded several more times using Tungsten to ensure that a secure connection had been made. Due to the sample's size, dropping inside the machine would make it impossible to be recovered and the fabrication would have to be repeated from the start. Finishing cuts were used to make the sample smoother and thinner. Fig. A.7a shows a side and Fig. A.7b shows a front view of the machined sample in the TEM holder.

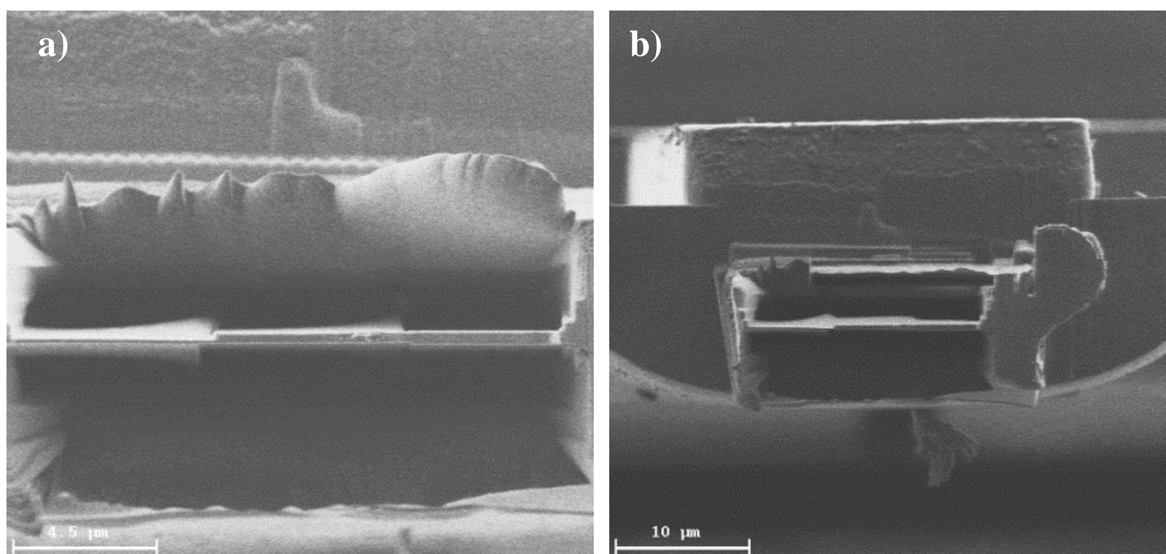

Figure A.7: Front view of the sample mounted in TEM holder (left) and a zoomed out view of the sample in the TEM holder (right)

A challenge with the finishing cuts was that due to the softness of the material, machining one area would result in material redisposition in neighbouring areas. Very small finishing cuts had to be made to minimize this and this resulted in extra added time in the process.

3 Finishing Clean – Ion Milling and Zone Cleaning

The sample was initially used in the TEM without first cleaning it from the Tungsten redeposition damage; however, it was found to be both too thick for lattice imaging and it also had too much redisposition damage from the FIB to get a clean image. Consecutively the sample had to be cleaned using a two stage process: (1) ion milling (Fischione Model 1010) and (2) ozone cleaning (TEM Ozone Cleaner). The sample was moved from the TEM holder onto a circular ion milling holder. The ion milling machine used Argon gas and was used in the metal cleaning mode due to the softness of the sample material. A 2kV voltage and 5mA current were used on each side of the samples for duration of three minutes each. The specimen was transferred back onto the TEM holder and the ozone cleaner was used for 10 minutes on each side of the sample.

This sample was used for all of the TEM experiments in included in this thesis.